CHARACTERIZATION OF INDIVIDUAL NANOPARTICLES AND APPLICATIONS OF NANOPARTICLES IN MASS SPECTROMETRY

A Dissertation

by

SIDHARTHA RAJA RAJAGOPAL ACHARY

Submitted to the Office of Graduate Studies of
Texas A&M University
in partial fulfillment of the requirements for the degree of

DOCTOR OF PHILOSOPHY

May 2010

Major Subject: Chemistry

CHARACTERIZATION OF INDIVIDUAL NANOPARTICLES AND APPLICATIONS OF NANOPARTICLES IN MASS SPECTROMETRY

A Dissertation

by

SIDHARTHA RAJA RAJAGOPAL ACHARY

Submitted to the Office of Graduate Studies of
Texas A&M University
in partial fulfillment of the requirements for the degree of

DOCTOR OF PHILOSOPHY

Approved by:

Chair of Committee,	Emile A. Schweikert
Committee Members,	David Church
	Paul S Cremer
	D.Wayne Goodman
Head of Department,	David H. Russell

May 2010

Major Subject: Chemistry

ABSTRACT

Characterization of Individual Nanoparticles and Applications of Nanoparticles in Mass Spectrometry. (May 2010)

Sidhartha Raja Rajagopal Achary, B.S., Wichita State University

Chair of Advisory Committee: Dr. Emile A. Schweikert

The chemical characterization of individual nanoparticles (NPs) ≤ 100 nm in diameter is one of the current frontiers in analytical chemistry. We present here, a methodology for the characterization of individual NPs by obtaining molecular information from single massive cluster impacts. The clusters used in this secondary ion mass spectrometry (SIMS) technique are Au_{400}^{4+} and C_{60}^{+}. The ionized ejecta from each impact are recorded individually which allows to identify ions emitted from a surface volume of ~10 nm in diameter and 5-10 nm in depth. The mode of analyzing ejecta individually from each single cluster impact gives insight into surface homogeneity, in our case NPs and their immediate surroundings.

We show that when the NPs (50 nm Al) are larger than the size of the volume perturbed by the projectile, the secondary ion emission (SI) resembles that of a bulk surface. However, when the NP (5 nm Ag) is of the size range of the volume perturbed by projectile the SI emission is different from that of a bulk surface. As part of this sub-assay volume study, the influence of neighboring NP on the SI emission was examined by using a mixture of different types of NPs (5 nm Au and 5 nm Ag). The methodology

of using cluster SIMS via a sequence of stochastic single impacts yield information on the surface coverage of the NPs, as well as the influence of the chemical environment on the type of SI emission. We also present a case of soft landing NPs for laser desorption ionization mass spectrometry. NPs enhance the SI emission in a manner that maintains the integrity of the spatial distribution of molecular species. The results indicate that the application can be extended to imaging mass spectrometry.

DEDICATION

To

My Father, Mother and Aunt,

My Brothers and Sisters

and

my Mentors

ACKNOWLEDGEMENTS

I would like to take this opportunity to thank all the people who helped and guided me over the past five years. First, I am ever so thankful to Dr. Schweikert for his guidance, mentorship, patience and support. Thank you believing in me and giving me the opportunity to be your student: one of the best decisions I have made in my life. I might have tested your patience at times. Thank you for giving me the freedom with my research to try anything I wanted by simply replying "you can try it out and see". It had blossomed into some fruitful projects and had made science more interesting for me. I have learned a lot from you, not only in science but outside in the real world too.

Next I would like to thank Dr Verkhoturov for his willingness to be always be available to discuss anything, form science to world geography. You have impressed me with your extent of knowledge in all areas and your appreciation for finer things in life. I have enjoyed working with you and learned a lot from you. I would like to thank my undergraduate advisor, Dr. Mike Van Stipdonk. Thank you for your support, advice and pushing me to further my education. I would like to express my thanks to members of the CCCA. Thanks to Dr. James for helping us maintain the facility and tempting me with your Harley. I will own a Harley one day. Mike Raulerson, Tammy and Tacy thank you for introducing me to Texas culture such as the rodeo. It was a fun experience indeed. I enjoyed getting to know Tacy and was inspired by her joyful spirit. I wish you guys the very best in life and hope to keep in touch. To Charlene Melton for deciphering Boss's handwriting and getting me acquainted to this lab. I would like to thank Sherry

Melton for taking care all the paperwork, from making travel arrangements, submitting papers, proof reading and even making sure I had a steady supply of the specific type of pens I liked. I would like to thank the previous Schweikert group members. Dr. Hager thank you for getting my feet wet in the lab when I joined the lab. I wish you and Sarah the very best. To Dr. Locklear for his long answers for everything and for keeping in touch even after graduation. To Dr. Li for teaching me insights of C_{60}.

I would like to thank the present Schweikert group members. Thank you Veronica for always being there for me, from proof reading to livening up moments with your fun personality. Every single day of grad school was exciting thanks to you. I will take and cherish all the memories we have had together to white water rafting in Denver to staying up late night designing experiments. I value our friendship and hope to keep our friendship for a long time. Thank you Li-Jung for teaching me Chinese and taking us to all the Chinese restaurants and I enjoyed working with you in projects. I wish you the best in grad school. You are almost there!!. And early congratulations for your wedding. To Mr. Mike Eller. Thank you introducing me to new things like Frisbee golf, baseball and loud music. You have been an interesting source of conversation and I have enjoyed your company over the last two years. I hope to you see you as a professor one day, maybe we can ride our Harleys together. To Mr. De Bord. You have impressed me with your learning ability. Thank for you introducing me to more Texas culture like steer wrestling, crawfish broil and tubing. It was a pleasure to work with you. I don't think you need any luck, I am sure you will excel in everything you do. To Atashi, all the best

with grad school. It will take some time but you will get a hold of everything pretty soon.

At this moment I would also like to take this opportunity to thank all the friends in College Station who have made my stay here a memorable experience. Friends like Srinivas, Suraen, Chatha and Tosin.

Finally, thanks to my family. My father who has been a source of inspiration to me. I don't think I will ever be smart as you are. To my mother and aunt for always being there for me. My brothers and sisters for their invaluable support and guidance throughout my life.

TABLE OF CONTENTS

CHAPTER Page

LIST OF FIGURES

FIGURE Page

FIGURE Page

LIST OF TABLES

CHAPTER I

INTRODUCTION

Many nano words have recently appeared in dictionaries, including nanoscale, nanocience, nanotechnology, nanostructures, nanotube, nanowire and nanorobot. The prefix "nano" is derived from the Greek word "nanos" meaning "dwarf". Nanotechnology, which is producing nanoscale objects and carrying out nanoscale manipulations, has been around for quite some time. While there are some exceptions, most of properties of the nanostructures begin to be apparent in systems smaller than 1 μm. Recent advances in synthesis and characterization tools, however, have fueled a boom in the study and industrial use of nanostructured materials. The number of publications on the topic of nanomaterials has increased at an exponential rate since the early 1990s, reaching about 40 000 in the year 2005, as indicated by a search on the ISI Web of Knowledge database.[1] The large number of publications on nanomaterials can be explained by the fact that nanoscience and nanotechnology encompass a wide range of fields, including chemistry, physics, materials engineering, biology, medicine, and electronics. Nanoparticles (NPs) are a major part of nanoscience and nanotechnology. They offer a useful platform demonstrating unique properties with potentially wide-range of applications because their properties can be controlled at the nanoscale.

This dissertation follows the style of *Nano Letters*.

Two primary factors cause nanomaterials to behave significantly differently than bulk materials: surface effects (large surface area to volume ratio) and quantum effects (showing discontinuous behavior due to quantum confinement effects in materials with delocalized electrons). These factors affect the chemical reactivity of materials, as well as their mechanical, optical, electric, and magnetic properties. In electronics they are used as components in devices to molecular machines, as nanomagnets that store information[2] for superfast computers and as nanowires will string together nanoelectronic circuits.[3,4] The purpose of this study is to provide a methodology for the characterization of NPs and their role in mass spectrometry. Prior to the presentation of the methodology and the role of NPs in mass spectrometry, it is useful to recall the scope of NPs in science and technology. Here we present a brief review.

Literature Review of the Use of NPs

NPs as Catalyst

In heterogeneous catalysis, metal NPs have been used for over 50 years.[5] The majority of the industrial catalysts are high-surface-area solids onto which an active component is dispersed in the form of very small particles. One of the first processes to use such catalysts is catalytic reforming for the production of reformulated gasolines.[6] Industrial catalysts containing NPs of 1 nm Pt on chlorinated alumina were introduced in the 1960s[7] and Pt–Re or Pt–Su bimetallic catalysts (1 nm particles) in the 1970s.[8] In hydrogenation, hydrocracking and aromatization processes, zeolites exchanged with

noble[9,10] and non-noble metals[11] are currently used. More recently metal catalysts were successfully employed in automotive catalytic converters.[12]

NPs as Vectors for Drug/Gene Delivery and Therapy

NPs can be used for drug and gene delivery either by modifying their surface chemistry or by using their unique physical properties. These properties of some common NPs and their corresponding ligands used for surface functionalization and their roles in different applications are given in Table 1.[14] A transmission electron microscopy (TEM) study of 16 nm Au NPs conjugated with human fibroblast cells shows control of the uptake mechanism either via delivery of Au NPs by liposomes or by surface modifications of the Au NPs with cell-penetrating peptides.[15] It has been shown that Au NPs increase the cellular mediated uptake of molecules such as transferrin. Au NPs conjugated with transferrin were shown to increase uptake by six times when compared to that in the absence of the interaction.[16] Similarly, Yamada and co-workers used NPs made of a yeast endoplasmic reticulum membrane to transfer genes as well as drug into human hepatocytes,[17] As seem the major advantage of using NPs as vectors to deliver genes or drugs over immunotargeted drugs, is the specific delivery of large amounts of therapeutic agents per targeting biorecognition event. Besides the surface chemistry of NPs, the unique physical properties of NPs can be utilized in the design of drug delivery systems. Bhatia et al. designed multifunctional supermagnetic NPs for remote release of bound drugs.[18] NPs have been widely used as delivery vehicles for other biomolecules too such as DNA, RNA and proteins, protecting these materials from

Table 1.1. Characteristics, ligands and representative applications of NPs made from various metal and semiconductor materials.[2]

Core Material	Characteristics	Ligand(s)	Applications
Au	Optical absorption, fluorescence and fluorescence quenching, stability	Thiol, disulfide, phosphine, amine	Biomolecular recognition, delivery, sensing
Ag	Surface-enhanced fluorescence	Thiol	Sensing
Pt	Catalytic property	Thiol, phosphine, amine, isocyanide	Bio-catalyst, sensing
CdSe	Luminescence, photo-stability	Thiol, phosphine, pyridine	Imaging, sensing
Fe_2O_3	Magnetic property	Diol, dopamine derivative, amine	MR imaging and biomolecule purification
SiO_2	Biocompatibility	Alkoxysilane	Biocompatible by surface coating

degradation and transporting them across the cell-membrane barrier.[19]

NPs for Biosensing/Imaging

It is an important goal for biomedical diagnosis, forensic analysis and environmental monitoring to sense and detect biological agents and diseases. Sensing can be done by fabricating the NPs or by functionalizing it. NPs can be used to detect biomolecules such as DNA. Mirkin and co-workers were the first to report colorimetric sensing of nucleic acids.[20] Since then studies of Au-NP interactions have subsequently been pursued by several groups.[21-24] Imaging using NPs is usually achieved by either quantum dots (QDs) or dye-doped NPs. The use of QDs for cell imaging was reported by the Alivisatos group. [25] Since then they have evolved into a routine technique for bioimaging systems.[26] Dye-doped silica NPs can be used to provide biocompatability, signal amplification and low toxicity.[27-28] Metallic NPs such Au NPs have excellent anitphotobleaching behavior under strong light illumination, resulting in strong native florescence under relatively high excitation power. He *et al.* have collected images of cell membrane when they were stained with Au NPs.[29] NPs have also been used as radioactive labels since 1950s and immuno-NPs conjugated to antibodies have been since the 1980s for biological staining in electron microscopy.[30] Their advantages over QDs and organic dyes include that they have much reduced or no toxicity and they offer better contrast for imaging.

NPs in Toxicology

Nanotoxicology is a branch of toxicology that address the adverse health effects caused by NPs. The reason for NP's toxicity comes from their ability to penetrate into cells and having adverse effects on the atmospheric environment. Peer-reviewed research articles on NPs and their toxicology has grown nearly 600 percent from 2000-2007, increasing almost exponentially across the 7-year period.[31] There are several reviews addressing nanotoxicology aspects; some are general[32-35], while other address selected aspects of NP toxicology. These selected areas include health effects of air pollution.[36-39] NPs in the atmosphere can also have important consequences for human health[37] and the environment.[38] They are usually released into the air directly by combustion or they may be formed in situ by gas-phase oxidation of precursors such as sulfur di oxide or volatile organic compounds. Inhalation of NPs has been shown to induce a variety of adverse responses associated with oxidative stress, pulmonary inflammation, or both.[39] Other reviews focus on epidemiological exposure to NPs.[40,41] NPs have also been found to diffuse, settle and agglomerate in cells. Makino and co-workers have found that permeation of AuNPs through intestine was found to be size dependant.[42] They showed that the distribution of various sizes from 15 to 200 nm of Au NPs were mainly accumulated in liver, lung and spleen, whereas accumulation in various tissues depended on the size of the Au NP.[42] There are reviews on effects of NPs in neurodegenerative diseases[43] and occupational settings[44] address the extensive effects of building demolitions and dust. Autoimmune diseases such as lupus eryhtematosus and

scleroderma can sometimes be associated with exposure to NPs, such as silica and asbestos.[45,46]

NPs in Mass Spectrometry

NPs are also used in mass spectrometry primarily to facilitate the ion emission from of compounds of interest.[47-53] Several different types of NPs have been used for this process from Co [47], TiN [50], Au [39], Ag [51] to SiO_2[53]. The mechanism of enhancement is not fully understood but mostly believed to be a thermal effect where the NPs absorb the laser energy and dissipate the heat to the analyte molecules .[50] Rotello and co-workers pioneered the use of different functionalized Au NPs as mass bar codes for a multiplexed screening assay to monitor cellular uptake of Au NPs by cells. This method can be used to simultaneously analyze many Au NPs and identify them by their unique mass barcode.[54]

Characterization of NPs

Despite the use NPs in these wide range of fields, there are only a limited amount of analytical tools available to characterize them. Established techniques such as TEM and scanning electron microscopy (SEM) are sensitive to morphology of the NPs. Other imaging techniques such as optical imaging (OI) can be used image NPs > 20 nm in diameter in phase contrast mode or differential interference contrast mode; fluorescence microscopy that has the benefit of detection at the single particle level;[29] photothermal coherence tomography (OCT) which has a penetration depth of 1-2 μm and a resolution

of 1-10 μm;[55] multiphoton surface plasmon resonance (SPR) microscopy [56]. X-ray scattering which has low signal-to-noise ratio with X-ray computer tomography, and gamma radiation using neutron activation.[57] These techniques offer isotopic information but no molecular information. Other techniques can also used be used to obtain chemical information such as derivatized AFM tips, infrared (IR) and Raman spectroscopy and are non destructive. The lateral resolution of Raman spectroscopy can be increased using modification such as tip enhanced Raman scattering (TERS), which has a lateral resolution of 20-50 nm.[56] As field of nanotechnology grows, it becomes increasingly important not only to explicitly identify the chemical composition of NPs themselves, but also of the functionalization or surface modification of the NPs.[58]

Mass spectrometry is well suited for the analysis of NPs to yield chemical information. The use of mass spectrometry in nanotechnology studies have focused on mass determinations of various sizes and types of NPs.[59-75] Royce Murray and co-workers have studied thiolated Au NPs extensively with minimal fragmentation, utilizing "soft" ionization sources such as electrospray ionization (ESI).[62-66] Other mass spectrometric techniques that cause extensive fragmentation such as plasma desorption (PD),[61] fast atom bombardment (FAB)[73] and laser desorption ionization (LDI)[59,60] have also been used to characterize NPs. However, spectra are complicated and the ions are obtained from several NPs. Nanoaerosol mass spectrometer (NAMS) is a technique that is increasing used to for the real-time characterization of individual NPs.[76-78] In this technique particles are accumulated through an aerodynamic inlet and size selected using

a quadrupole and analyzed by time-of-flight mass spectrometer. Due to the ablation of the laser, NAMS is able to provide only elemental information.

Secondary Ion Mass Spectrometry (SIMS) is mass spectral technique that is capable of obtaining molecular chemical information from NPs. SIMS is a surface analysis technique where primary ions which can be atomic or polyatomic are used to sputter positively and negatively charged secondary ions. The secondary ions (SIs) originate from the outermost nanometer of the sample.[79] The general schematic for the SIMS experiment is presented in Figure 1.1.

Traditionally, atomic projectiles such Ar^+, Ga^+, or alkali metals are used as primary projectiles. The SIs are either positive or negative, depending on the primary ions' identity; neutral species can be detected using post ionizations methods.[80] The mass spectrum is related to the chemistry of the material being analyzed. A major breakthrough in SIMS came with the advent of using polyatomic species or "clusters" as projectiles. The section below offers a brief synopsis on cluster SIMS.

Background

Cluster SIMS

Over a decade ago, it was shown that cluster ions are more effective at desorbing molecules. Blain and co-workers showed that the molecular ion yields (number of secondary ions ejected per incident primary ion) of phenylalanine, gold and CsI increased when clusters of CsI and organic molecular ions were used as the primary, as

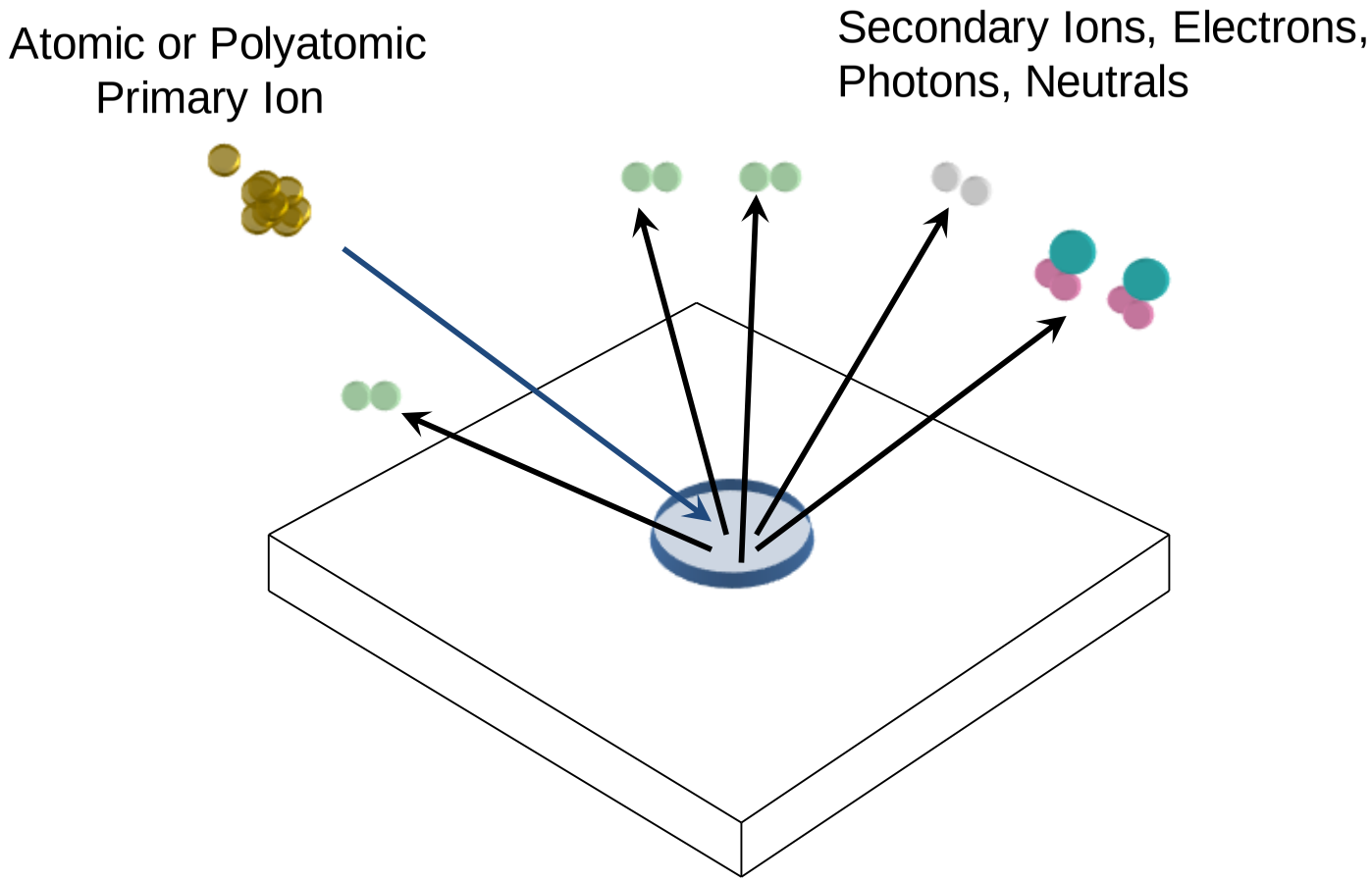

Figure 1.1. Representation of the SIMS process.

compared to atomic projectiles.[81] A nonlinear effect in the SI emission of molecular ions from organic targets was seen with small gold clusters, when compared to atomic gold projectiles under equal velocity.[82] A similar effect was observed by Delmore and co-workers when they used a SF_6 source.[83] Since the advent of commercial sources, Au_3^+, Bi_3^+ and C_{60}^+ ion sources have become popular. The Au_3^+ source utilizes a liquid-metal ion gun, while the C_{60}^+ is an effusion source. Recently massive gold clusters such as Au_{400}^{4+} (>80 000 Da) have been shown to be a even more effective projectile. Molecular ion yield enhancement of 1000 is obtained when compared to Au^+ during bombardment of the neuropeptide dynorphin and gramicidin S. Au_{400}^{4+} also yields minimal surface damage and a significantly lower fragmentation.[84] More energy is deposited in the sample near the surface as the momentum increases for a given energy (a large, heavy particle deposits its energy nearer the surface than a smaller, lighter particle of the same kinetic energy).[85]

C_{60}^+ is also used as a cluster projectile to increase the SI sputtering yield, as compared to atomic projectile. Previous studies from our lab using the C_{60}^+ projectile has shown an increase in the yield of phenylalanine by a factor of 17 when compared to Cs^+ primary ions.[86] Similar results have been obtained when a beam of C_{60}^+ projectiles was used on a gramicidin target. The secondary ion yields of gramicidin with the C_{60}^+ projectile were increased by an order of magnitude, when compared with the Ga^+ projectile.[87]

Another important aspect of using polyatomic projectiles is multi-ion emission. The effectiveness of the Au_{400}^{4+} projectile to emit multiple SIs from a single projectile is

referred to as ion multiplicity, which is the number secondary ions emitted per incident projectile. With Au_{400}^{4+}, the most probable event shows the desorption of eight secondary ions as compared to zero secondary ions with the Au_3^+ projectile when a vapor deposited sample of phenylalanine was analysed.[88] It has also been shown that cases of multiple secondary ion emission are increased with the energy of the Au_{400}^{4+} projectile.[88] For small projectiles such as Au_3^+ the mode of interaction can be described by the thermal spike model where there are overlapping collision cascades leading to additional sputtering.[89] However with heavier large clusters the enhancement in yields cannot be explained by the overlapping collision cascades. Bitensky and Parilis proposed the shockwave mechanism to explain the increase in yield under cluster bombardment. Where there is a decrease in stopping power due to a "clearing the way effect" produced by the first atoms in the cluster which hit the surface.[90] Recently, experiments from our lab has shown that the Au_{400}^{4+} projectile interacts with the substrate via hydrodynamic penetration. This effect is different from the overlapping collision cascade effect, in that it involves an extreme pressure transient at the interface of the colliding solids that lasts for a few picoseconds. The process involves several physical phenomena such as impact light flash, ejection of matter and crater formation.[91]

Analysis of NPs Using SIMS

The preceding comments suggest that cluster SIMS by virtue of enhanced secondary ion yields and ion multiplicity holds promise for the analysis of NPs. Yet the literature reveals that with a few notable exceptions, the studies are limited to atomic

projectiles in the dynamic[92] and static regime[93]. Sun and co-workers studied thiolated gold NPs of size 2.5 nm and 2.0 nm with a ToF-SIMS instrument equipped with a Ga gun. Impurities were found in one preparation technique as compared to the other.[94] Other studies include the investigation of the nanoclusters of Au desorbed from a surface upon impact by ^{252}Cf fission fragment.[95] NPs of gold with grain sizes of 2-100nm were sputtered by 1 MeV Au_5^+ and showed that the highest yield was obtained with 19 nm islets.[96] Shi et al reported the characterization of Al_2O_3 NPs in the 10-150 nm. They confirmed the existence of a nano-surface deposition of a pyrole film around the particles using ToF-SIMS.[97] NPs have been used to grow layer by layer on a polyester surface and then were characterized by ToF-SIMS using Ga^+ as a projectile. These were alternating layers of SiO_2 (7nm) and TiO_2 (40-50 nm).The results revealed that the layers intermix.[92] Surface ligands conjugated to quantum dots were characterized and imaged using a Bi^+ ion gun. As the beam was rastered across a 200 x 200 μm^2, the mass spectra were obtained from several NPs.[93] Recent studies performed in our lab using cluster SIMS via single impacts has shown molecular chemical information can be obtained from a mixture of nano-objects. The mixture contained Al nano-whiskers (2 nm wide) decorated with polystyrene NPs (30 nm). Results indicated that the technique can be used to separate mass spectra from these two different nano-objects.[98]

Prospects for Characterizing Individual NPs with SIMS

When the dose of bombardment is $\sim 10^6$ projectiles/cm^2, the term "super" static regime is used to describe them. The experiments described in this dissertation are

performed in the "super" static regime. Where primary projectiles isolated in space and time are used to impact an analyte stochastically. The secondary ions from each individual impact is collected and stored before another projectile perturbs the surface. The methodology is termed event-by-event bombardment/detection.[88] This allows one to later select specific mass spectra which contains a specific type of secondary ion. Under such conditions, the lateral resolution is set by the area perturbed by the projectile. The lateral resolution of this method for large cluster projectiles such as Au_{400}^{4+} and C_{60}^{+} have been found to be an area of 100 nm^2.[99,100] This resolution fall in the size range of certain NPs.

One advantage of performing the experiment in the event-by-event bombardment/detection is it allows one to explore ions that are co-emitted from each impact (1000 nm^3) volume. It can be achieved by coincidence counting. The section below gives a brief synopsis of this technique.

Coincidence Ion Mass Spectrometry

Coincidental counting methods have been practiced in the field of nuclear science for a long time.[101] The time of flight (ToF) technique itself could be considered as coincidence technique where it can be used to detect signals originating from a single desorption event. In essence, ToF along with event-by-event bombardment/detection mode can be used to determine the spatial relations of the various secondary ions observed. Two conditions are required for coincidence counting. The first, the primary projectile should address only a small region of the sample so individual components can

be spatially isolated. The second requirement is that each individual component of the sample studied must have a characteristic mass spectral peak.[102] The concept of coincidence counting technique to analyze sample chemical homogeneity was first suggested by Della-Negra and co-workers.[103] It was later demonstrated in our lab to analyze NaF crystals.[102] The application of coincidence measurements in mass spectrometry has been described by Van Stipdonk et al.[104] Coincidence counting has been used by our group extensively to determine surface microhomogeniety. [105-108]

In this dissertation we discuss for the first time a methodology for the characterization of individual NPs using cluster SIMS in the event-by-event bombardment/detection mode and the role of NPs to increase ion emission in mass spectrometry. In the following paragraphs, the methodology will be discussed in detail in relation to the analysis of NPs.

Scope of the Present Study

In the first case, we present a study which deals with the determination of the relative abundance of the oxide layer in the near-surface volume of aluminum NPs of 50-100 nm in diameter. They are bombarded with a sequence of single projectiles of Au_{400}^{4+} accelerated to 136 keV and C_{60}^{+} accelerated to 26 keV. The ionized ejecta from each impact are recorded individually which allows to identify ions emitted from a surface volume of ~10 nm in diameter and 5-10 nm in depth. The mode of analyzing ejecta individually from each single cluster impact gives insights into the effectiveness of the coating of these NPs. In this study the NPs represent a bulk surface as the NPs (50 nm)

are larger than the size of the volume perturbed by the projectile (1000 nm^3). However, the question arises on the type and abundance of the ionized ejecta when the NPs are in the size range of the volume perturbed by the projectile.

5 nm Ag NPs capped with decanethiol supported on organic substrate were used as a model for this sub-assay volume study. The methodology of using cluster SIMS via sequence of stochastic single impacts yield information on the surface coverage of the NPs, as well as the influence of the chemical environment on the type of SI emission.

As an extension of the study, another question that was addressed was how the type of SI emission from these sub-assay volume NPs, compare to that of a chemically identical bulk surface. Further a mixture such NPs (Ag and Au) supported on an organic substrate was studied to see the influence of the neighboring NP on the SI emission. A key question that was addressed is the ability to separate different type of NPs via this mass spectrometric technique.

As an application of these NPs, the final study presents the influence on ion emission when these NPs are deposited as single layer on top of an analyte, followed by laser ablation. As a test case, we present how these NPs can be used to increase the signal of the deprotonated species of the molecular ion from samples of dynorpin 1-8 fragment and substance P. The NPs were deposited evenly on the surface using a solution free commercially available technique that employs pneumatics. The results indicate the application can be extended to imaging samples as well.

CHAPTER II

EXAMINATION OF NANOPARTICLES VIA SINGLE LARGE CLUSTER IMPACTS*

Introduction

The goal of this study was to determine the relative abundance of oxide layer in the near-surface volume of aluminum NPs nominally coated with a self-assembled monolayer, SAM, of palmitic acid. Specifically, the particles (high combustion rate propellants) are prepared with a controlled oxide layer and then coated with the SAM to prevent further oxidation (Figure 2.1). In practice, the coverage with the SAM may not be complete, thus prompting degradation of the particles when exposed to air. We address here this issue with a variant of SIMS, which differs from customary SIMS in the type of projectile and mode of operation.

One area where nanotechnology has made an impact is in the field of energetic materials.[109] Metal powders are extensively used as fuels in most solid rocket propellants because of the effective combustion rate. Hence, the best propellants are those that produce the highest combustion temperature for the smallest possible molecular weight of the combustion products—aluminum is an ideal choice.

---

*Parts of this chapter are reprinted with permission from *Nano Letters*, Volume 8, S. Rajagopalachary, S.V. Verkhoturov, and E. A. Schweikert, Examinations of Nanoparticles via single Large Cluster Impacts, pages 1076-1080, 2008. Copyright [2008] American Chemical Society.

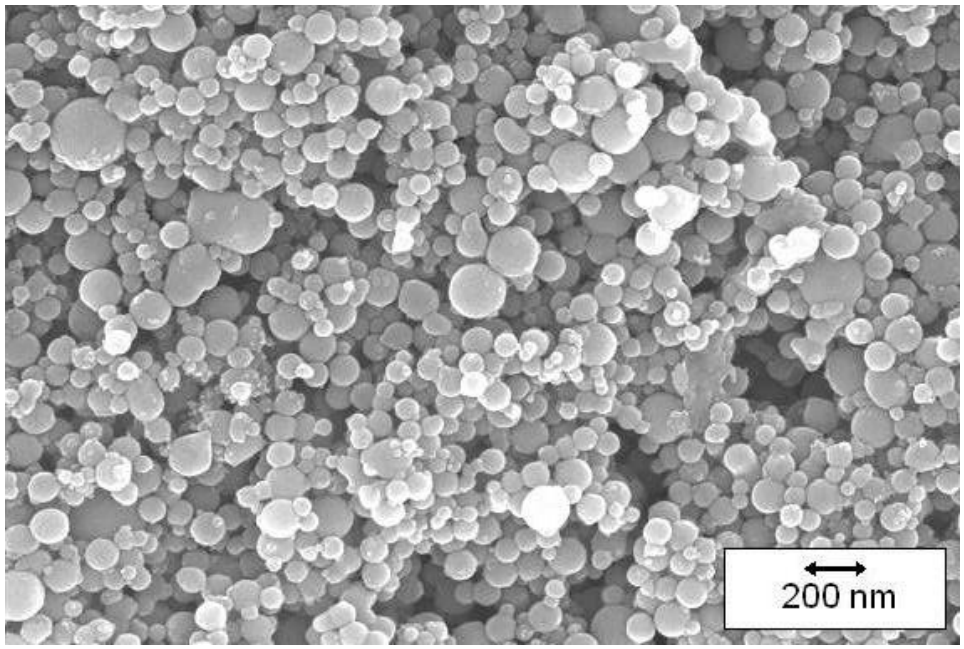

Figure 2.1. Micrograph of analyte obtained by SEM. The Al NPs (average size ~50 nm) are nominally coated by a self assembled monolayer of palmitic acid (layer thickness ~2-3 nm).

Micron-sized particles have been used to increase the combustion rate of solid rocket propellants. Since particle size and surface energy are critical, NPs are superior to micron-sized particles.[110] One such particle that is commercially available is Alex®. Alex is a nanosized aluminum powder made by electroexplosion of aluminum wire which consist of spherical particles in a distribution of diameters ranging from 50-200 nm. Figure 2.2a shows a SEM of the Alex particles advertised by the manufacturer as 50 nm in diameter. An analysis of the distribution of particle size is depicted in Figure 2.2b.[109] the centroid of the peak falls around 70 nm. Hence, there is a discrepancy between the advertised average size and the actual distribution of size. As our experiment is performed via single impacts, the size difference in size does not affect our experimental results. As with most reactive surfaces, Alex is prone to degradation when exposed to air through oxidation. Subsequent use of the degraded material in explosive and propellant compositions would result in significant loss of performance. Alex shows aluminum contents with 87% to 99% active aluminum, with the remaining material consisting of predominantly oxide (Al_2O_3). The aluminum oxide layer usually amounts to a 2-3 nm thick layer (Figure 2.2c).[111] To prevent the oxidation of the aluminum, these particles are coated with a SAM of palmitic acid. Fourier Transform- Infrared(FT-IR) analyses verified that the passivation coating on the coated Alex is chemically bound to the aluminum surface via a carboxylate linkage. The coating forms an effective barrier to hydrolysis and oxidation and the durability of the coated Alex over time has been tested and shown to last longer than the conventional Alex while still retaining the combustion properties of the aluminum.[110]

a).

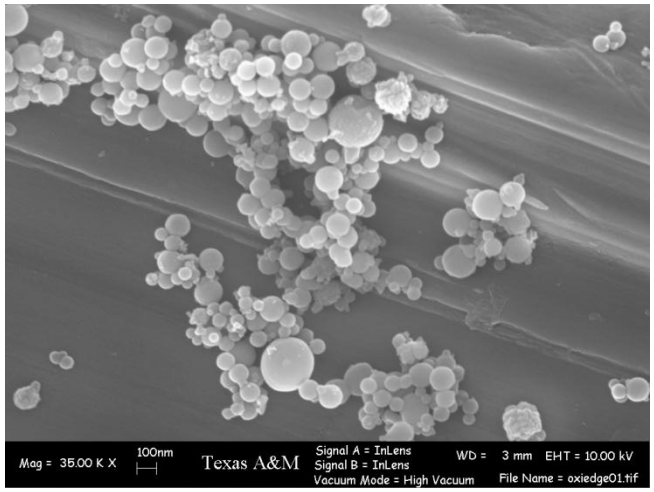

b).

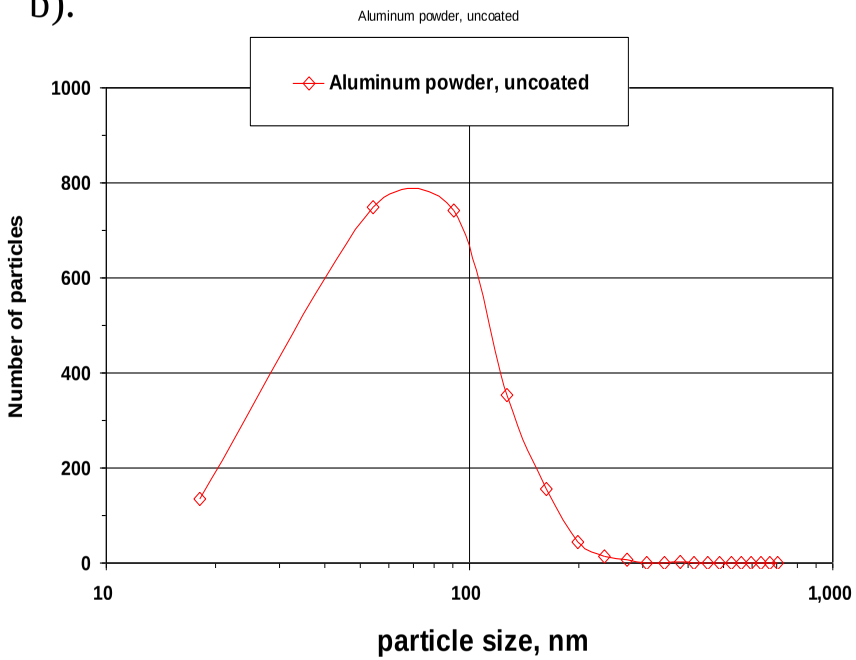

c).

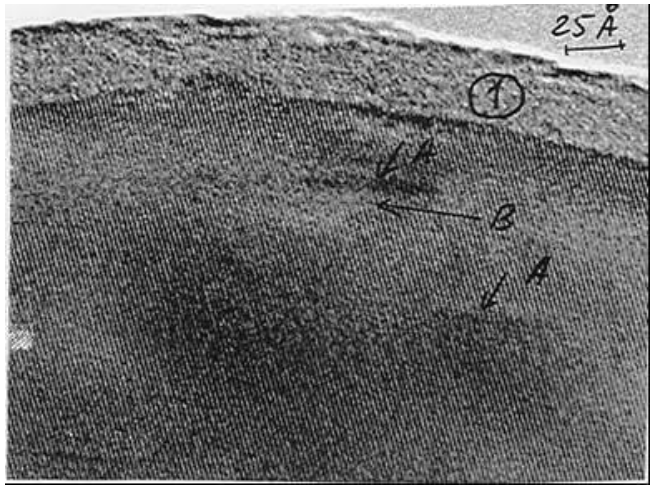

Figure 2.2. a) SEM image of 50 nm Alex® particles. b). The distribution in the size for 50nm Alex. c). High resolution TEM photo of Aluminum powders (APS-100 nm). Thickness of the oxide coating is ~ 25-30 Å.[111]

Another commercially available version of this particle has a paraffin overlayer on top of the layer of the palmitic acid to provide additional protection. The paraffin coating provides additional 3% by weight. The coating process is not perfect and the manufacturer has indicated that the organic coating might not be completely cover the NPs which gives way to the possibilities of an underlying oxide layer where there is an absence of the coating.[111]

These particles and other metallic particles have been characterized by imaging techniques such as SEM, which is unable to distinguish between the coated and the uncoated NPs. Toshima (et al.) has discussed the several different methods that are available for the analysis of these ultra fine NPs.[113] Several questions still remain unanswered regarding the quality and the extent of coverage of the palmitic acid and the efficiency of the palmitic acid in protecting the underlying aluminum from oxidation.

We show below that the sorting of SIs from a sequence of single impacts on the NPs allows to assess the relative SAM coverage and to compare the overall oxide layer with those in areas covered by the SAM (Figure 2.3). It must be noted that the data presented are from samples of NPs deposited on a metal substrate. The thickness of the NP layer was a few μm. The projectiles probe the sample stochastically in a non-imaging mode. NPs were bombarded with a sequence of single massive projectiles, specifically hypervelocity Au_{400}^{4+} and C_{60}^{+}. Massive cluster projectiles are utilized for these studies due to their high efficiency of multi-ion emission. It is well documented that surfaces bombarded with high energy clusters show enhanced emission of molecular

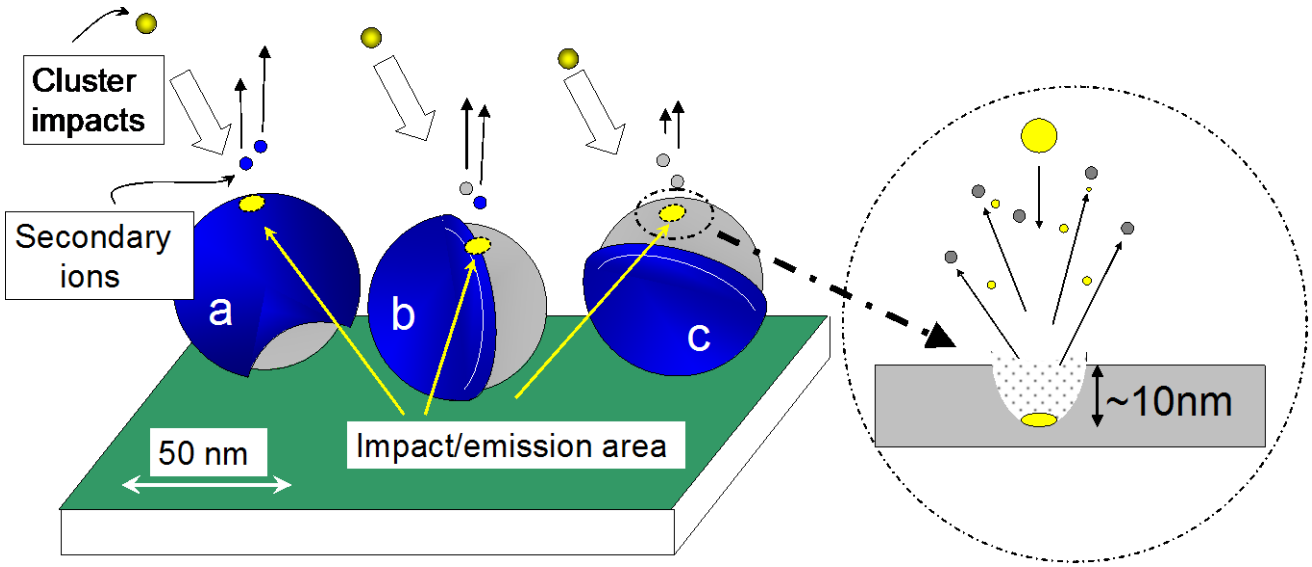

Figure 2.3. Schematic illustration of the analysis of NP surface areas. The aluminum NPs (size ~ 50nm) were slightly oxidized before they were coated by a self assembled monolayer (SAM) of palmitic acid. SAM coated areas are indicated in blue color. The uncoated areas (grey) are aluminum oxide layers. Single impacts of large gold cluster ions (136 keV Au_{400}^{+} or 26 keV C_{60}^{+}) stimulate the emission of the secondary atomic, molecular and cluster ions. The emission area is a nano-domain of ~10 nm in depth. The type of emitted ions depends on the area of a single impact. Micrograph of analyte obtained by SEM. The Al NPs (average size ~50 nm) are nominally coated by a self assembled monolayer of palmitic acid (layer thickness ~2-3 nm).

ions.[84,114] A unique feature of our experiment is that the ionized ejecta or secondary ions, SIs, from each impact were mass-analyzed and recorded from each single projectile impact. In this way, relationships were deduced between ions emitted from each nanovolume perturbed by the single projectile impact. The mode of analyzing ejecta individually from each single cluster impact is a means to apply mass spectrometry in nanovolumes.

Under these conditions, one observes the SIs emitted from the volume perturbed by one projectile impact, i.e. a hemispherical surfcace volume of 10 nm in diameter and a depth of 5-10 nm.[99,115] Such co-emitted SIs can reveal information about molecules co-located in a nanovolume.[102,117] The NPs were of two different average size distributions, 50 nm and 100 nm. The particles had distinct surface characteristics: the 50 nm particles had either an oxide layer of 2-3 nm thickness or were covered with a monolayer of palmitic acid ([M-H]- m/z 256); the 100 nm particles were covered with a monolayer of palmitic acid or a double layer of palmitic acid and paraffin. The particles were shipped and handled in argon atmosphere because of the reactive nature of aluminum. These NPs are prone to form micron sized clusters that appear more tightly agglomerated than the standard Alex powder[61] They were dissolved in acetone at 25 mg/mL and sonicated. A 25-μL aliquot of the solution was deposited on a metal substrate. The thickness of the NP layer on the substrate was larger than the depth of secondary ion emission (~ 10 nm). The NPs were briefly exposed to the air (~ 10 min) during deposition on the substrate and insertion into the mass spectrometer.

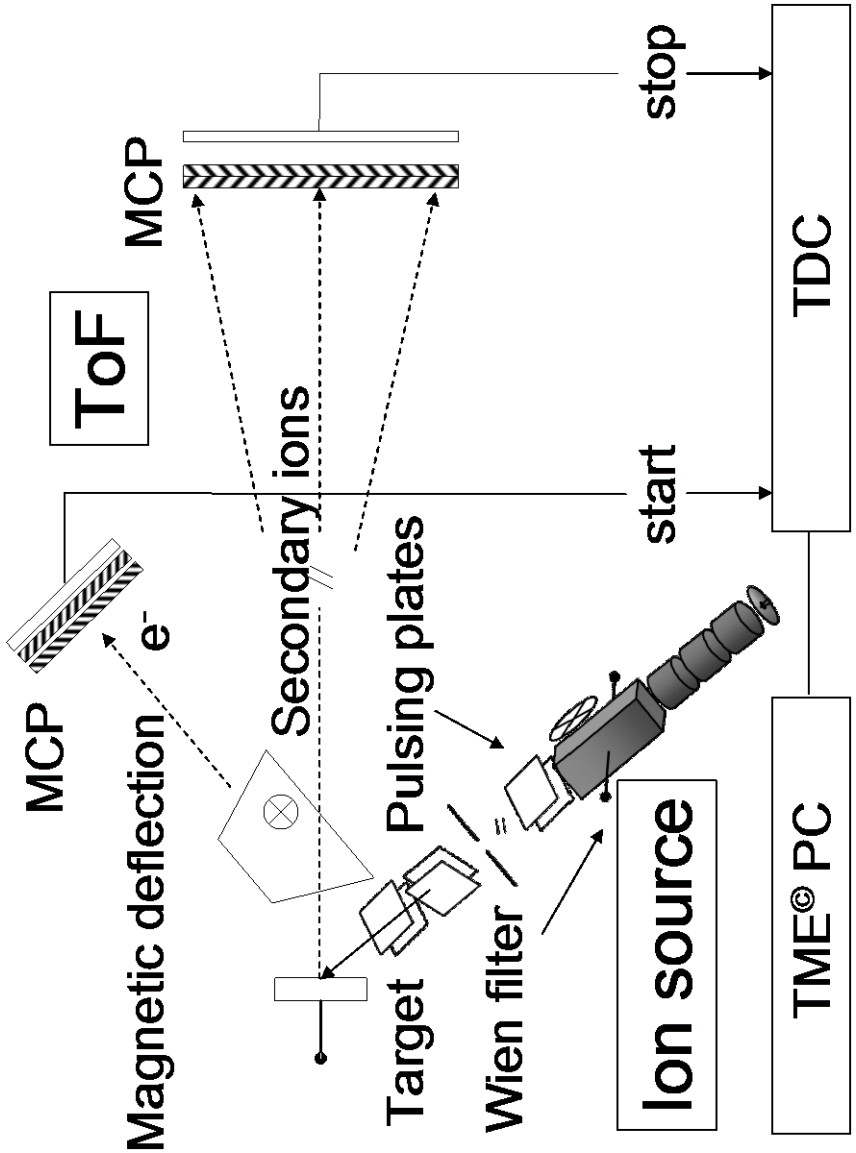

Figure 2.4. Schematic of the Cluster SIMS instrument with the Au LMIS. The 136 keV Au_{400}^{+} projectiles generated by the ion source strike the target (NPs deposited on the metal substrate) at a repetition rate of ~1000 impacts/s. The secondary electrons are emitted from single cluster impacts, deflected by the weak magnetic field, and detected by the dual microchannel plate (MCP) detector. The pulse from this detector serves as the start signal for the time-of-flight measurement of secondary ions. The secondary ions are detected by another set of dual MCP detector. The pulse from this detector constitutes the stop signal. The start and stop signals are fed into a time-to-digital converter (TDC), its output is stored in a PC as individual mass spectra by the Total Matrix of Events (TME©) software.[68]

Experimental Section

The experiments were run on a cluster SIMS instrument comprised of a liquid metal ion source, a Wien filter for primary ion mass selection, a beam pulser for single projectile bombardment and a linear ToF mass spectrometer (Figure 2.4).[117] Gold primary ions are produced by heating a tungsten reservoir and needle assembly filled with an Au/Si eutectic. The melting of the eutectic yields the formation of ions of Au_n^{q+} where n= number of atoms and q= charge of the ion. The primary ion beam is then focused onto a Wien filter using a series of electrostatic lenses. The Wien filter allows for the selection of a projectile with a certain number of atoms to charge (*n/q*) ratio while deflecting the rest. The mass/time selected cluster projectiles used in this study are on average Au_{400}^{4+} accelerated to 136 keV. In these conditions, it was found that the Au_{400}^{4+} cluster had an average of 400 atoms with an overall net charge of +4 on the cluster.[118] Since these experiments were done in event-by-event bombardment/detection mode, the filtered beam was pulsed between two plates biased with +1 and -1 kV at a frequency of 10 kHz.[119] The beam then passes through a 0.4 mm aperture before reaching a negatively biased target. The secondary electrons that are emitted from the target are deflected to a micro-channel plate detector assembly and used as the start signal for the ToF for the secondary ions. The secondary ions then travel through the field-free drift tube before hitting a micro channel plate assembly followed by an eight-anode detector array where they are registered as a stop for the secondary ions' time of flight. The signals from the detector are processed by a constant fraction discriminator and routed to a high resolution time-to-digital converter. A unique feature of event-by-event bombardment/detection

mode is that the mass spectrum of each individual event is stored in a reserved space in the computer memory before the impact of the next projectile. The total mass spectrum obtained, after processing through the custom software, is the sum of all the individual events. All impact/emission/detection events (typically ~ $2x10^6$ events) are collected and stored as a "Total Matrix of Events", TME, described elsewhere.[119]

The C_{60} ToF-SIMS instrument has a similar set-up with a few minor differences. Figure 2.5 gives a schematic of the instrument. Instead of a LMIS, it has an effusion source. The material to be used as the primary projectile, in this case C_{60}, is placed in the copper reservoir and heated in vacuum until it sublimes. The vapor then effuses into a cylindrical electrode area, where the heating of a 0.01" tungsten wire causes the emission and penetration of thermal electrons into the sublimed material causing ionization.[120] The ionization produces a range of ions from fragments of C_{60}^+ and to the unfragmented C_{60}^+. The ions are then focused using electrostatic lenses and by using a pair of steering plates guided towards a Wien filter. The Wien filter can be used to select the primary ion of interest. An off-centered slit allows for the ions deflected by an electric field to pass through while preventing the neutrals, that are unaffected by the deflection field from reaching the target. A second set of steering plates is used to guide the primary ion towards the target.

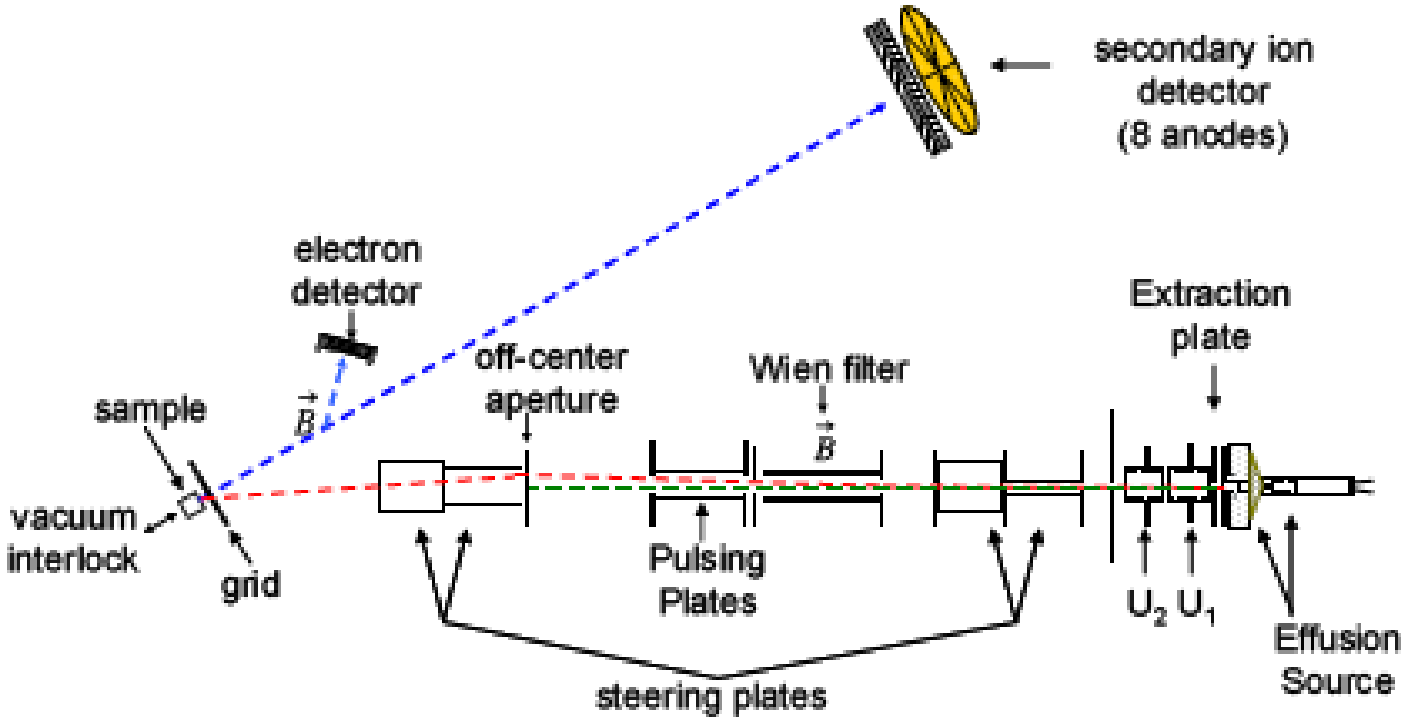

Figure 2.5. Schematic of the Cluster SIMS instrument equipped with the C_{60}^+ effusion source. The C_{60}^+ projectiles are directed towards a negatively biased target. The electrons from the impact are used as the start signal of ToF for the secondary ions. The SI ions travel through a field free region and arrive at a set of micro channel plates that constitute the stop detector. This is used as the stop signal for their ToF. The start and stop signals are fed into a time-to-digital converter (TDC), its output is stored in a PC as individual mass spectra by the Total Matrix of Events (TME©) software.[68]

Results and Discussion

The performance of SIMS with single large cluster impacts is demonstrated below on different samples of the specimens; 50 nm coated with palmitic acid, 100 nm coated with palmitic acid, 50 nm oxidized and a doubly coated with palmitic and then paraffin. The summary mass spectra of negatively charged SIs are presented in Figure 2.6.a, b and c. These mass spectra have common peaks in the lower mass range, which correspond to the aluminum oxide layer.[121] The prominent peaks are at m/e = 43, attributed to AlO^-, and at m/e = 59, attributed to AlO_2^-. In the higher mass range the mass spectrum shows repeating units of cluster ions.

Some of these SIs are oxide-specific ions while others are hydroxide specific ions with different base units. These clusters match with the cluster found in literature.[121] The clusters can be classified into three different groups, namely $[(Al_2O_3)_nAlO_2]^-$,$[(Al_2O_3)_nOH]^-$ and $[AlO_2\ (AlO)_n\ (OH)_n]^-$. The aluminum oxide clusters are present, despite the coverage of these particles by a monolayer of palmitic acid, because the palmitic acid layer is only 2-3 nm in thickness. However, the depth of secondary ion emission for the Au_{400}^{4+} projectile is ~10 nm in organic layers.[99] The most abundant cluster (both in terms of intensity and number) is $[(Al_2O_3)_nAlO_2]^-$. In our experiments, the least abundant cluster group is $[AlO_2\ (AlO)_n\ (OH)_n]^-$, where n does not exceed 4. Returning to the mass spectrum of the NPs from the 50 nm coated sample (Figure 2.6.a), a peak that can be attributed to the deprotonated molecule from the palmitic acid (m/e 255) is visible, in between the two clusters of $[AlO_2(AlO)_3(OH)_3]^-$ ($Al_4O_8H_3$ in Figure

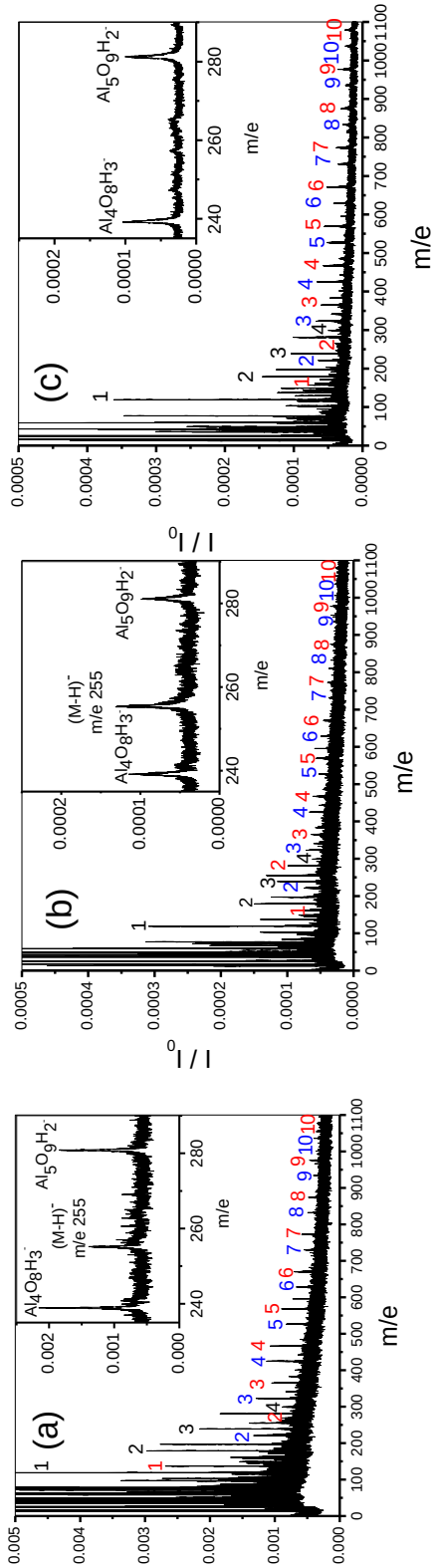

Figure 2.6. Negative ion mass spectra of (a) 50 nm coated, (b) 100 nm coated and (c) 50 nm oxidized obtained under Au_{400}^{4+} bombardment at 136 keV total impact energy. The secondary ions can be classified into different clusters that are color co-coordinated as follows. The red colored peaks are clusters with the generic formula $[(Al_2O_3)nAlO_2]^-$, the blue colored peaks are clusters identified as $[(Al_2O_3)_nOH]^-$ the black colored peaks are clusters with formula $[AlO_2(AlO)_n(OH)_n]^-$, where n in each case is an integer. The peak intensities (I) are normalized to the total number of projectiles I_0 on the y-axis. A magnified version of the mass range from 235-290 is given in the insets. The deprotonated molecule of the palmitic acid is present in 50 nm coated and 100 nm coated between the clusters represented by the formula $[AlO_2(AlO)_3(OH)_3]^-$ (in figure $Al_4O_8H_3$) and $[(Al_2O_3)_2(AlO)(OH)_2]^-$ (in figure $Al_5O_9H_2$), but absent in 50 nm oxidized NP .

2.6 inset) and $[(Al_2O_3)_2\ (AlO)(OH)_2]^-$ ($Al_5O_9H_2$ in Figure 2.6 inset). The assignment of this peak to palmitic acid is verified by the cluster SIMS analysis of palmitic acid (Sigma Aldrich) which shows the deprotonated molecule at m/e = 255. The mass spectrum of the 50 nm coated NPs (Figure 2.6 a) is similar to the spectrum of the 100 nm coated NPs in terms of the presence of clusters, but the intensities of the peaks are lower. Concurrently, the intensity of the palmitic acid ion is higher for the 100 nm coated NPs (Figure 2.6.b). Both of these observations suggest that SAM coated particles from the 100 nm coated have more complete coverage. As a reference, the oxidized uncoated particles were also analyzed (Figure 2.6.c). It shows an increase in intensity of the aluminum oxide clusters when compared to the coated particles. The increase can be attributed to the greater thickness of oxide layer on uncoated particles. A similar mass spectrum, with the decreased intensity for aluminum oxide clusters as well as for the palmitic acid, was observed for the double coated 100 nm particle (Figure not shown). The SI yield is defined as the number ions emitted per projectile impact. A comparison of the yields for the deprotonated molecule of palmitic acid m/e 255 for the different Al particles projectiles is shown in Figure 2.7. The oxidized 50 nm particle has zero yield because of the absence of the coating of palmitic acid. A comparison of the yields of palmitic acid for the coated 50 nm and coated 100 nm particles shows that the yield of the coated 100 nm particles is higher, which again supports the hypothesis that the coated 100 nm particles have a better coverage of the palmitic acid than the coated 50 nm particles. However, the doubly-coated 100 nm particle has a lower yield for the palmitic acid than

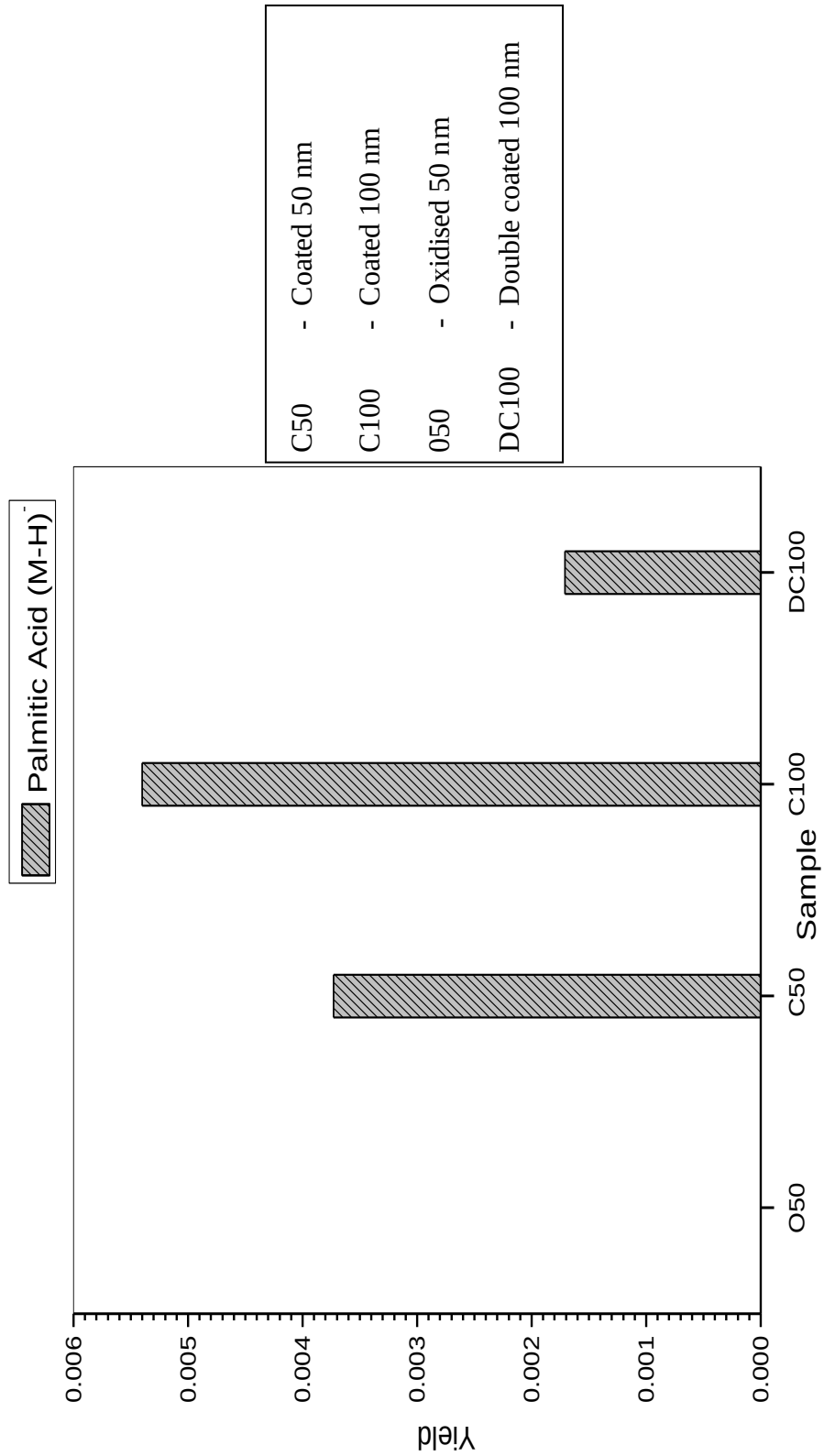

Figure 2.7. Comparative yield of deprotonated molecule of palmitic acid (m/e 255) for the different particles when bombarded with Au_{400}^{4+} projectile at 136 keV total impact energy.

either of the coated particles because the emission of the molecular ion of the palmitic acid is suppressed by the outer layer of paraffin. A similar phenomenon was observed when the signal from an indicator layer is suppressed by addition clay layers on top.[99] Yields of the most intense cluster in the mass spectrum (described by the formula $([Al_2O_3)_nAlO_2]^-$) for the different particles with two different projectiles further support the inequality in coverage (Figure 2.8). A trend similar to that with Au_{400}^{4+} is observed with the C_{60} projectile but the yields of the SI clusters are half as much of those from Au_{400}^{4+}. The C_{60}^+ projectile is less efficient than the Au_{400}^{4+} projectile in the desorption of the molecular ion, as demonstrated by a test case where a vapor deposited target of C_{60} was analyzed.

The yield for the intact molecular ion (C_{60}^-) with 136 keV Au_{400}^{4+} was 0.16 as compared to a value of 2×10^{-4} with a 18 keV C_{60}^+ projectile.[122] The comparison was extended to other Al oxide clusters $([Al_2O_3)_nOH]^-$ (Figure 2.9). Additionally, the difference in the extent of coating was supported by the yields of smaller aluminum oxide peaks (Figure 2.10). The SIs include AlO^- (m/e 43), AlO_2^- (m/e 59) and $Al_2O_4H^-$ (m/e 119). Yields of AlO^- and $Al_2O_4H^-$ are the highest in the oxidized 50 nm particles where there is no external organic covering. The next highest is the coated 50 nm particles and then followed by the coated 100 nm particles. The yields of these two ions are lower for the coated 100nm than the coated 50nm particles because the coated 100 nm particles had better coverage. The yields for the doubly coated particles are the lowest among the four Al particles because of the external covering of the paraffin.

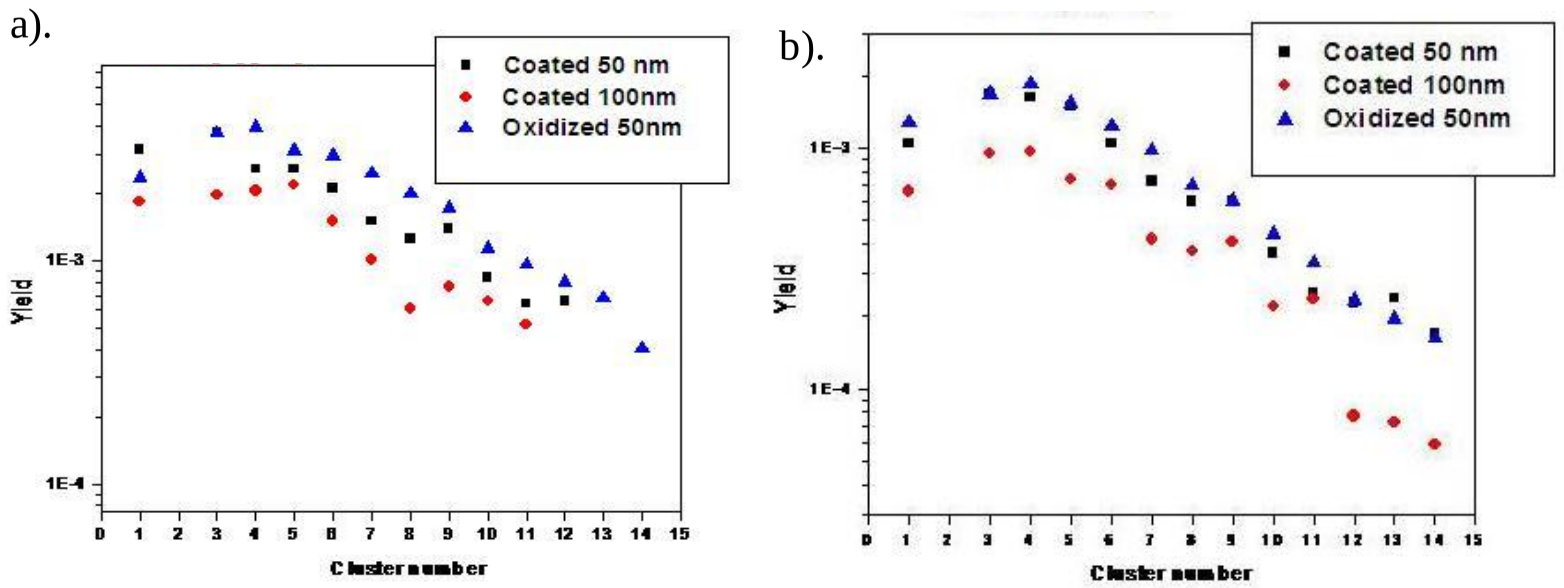

Figure 2.8. Yields of the Al oxide clusters ($[Al_2O_3)_nAlO_2]^-$) as a function of integer n in the molecular formula for the 3 samples with a). 136 keV Au_{400}^{4+} and b). 26 keV C_{60}^{+}.

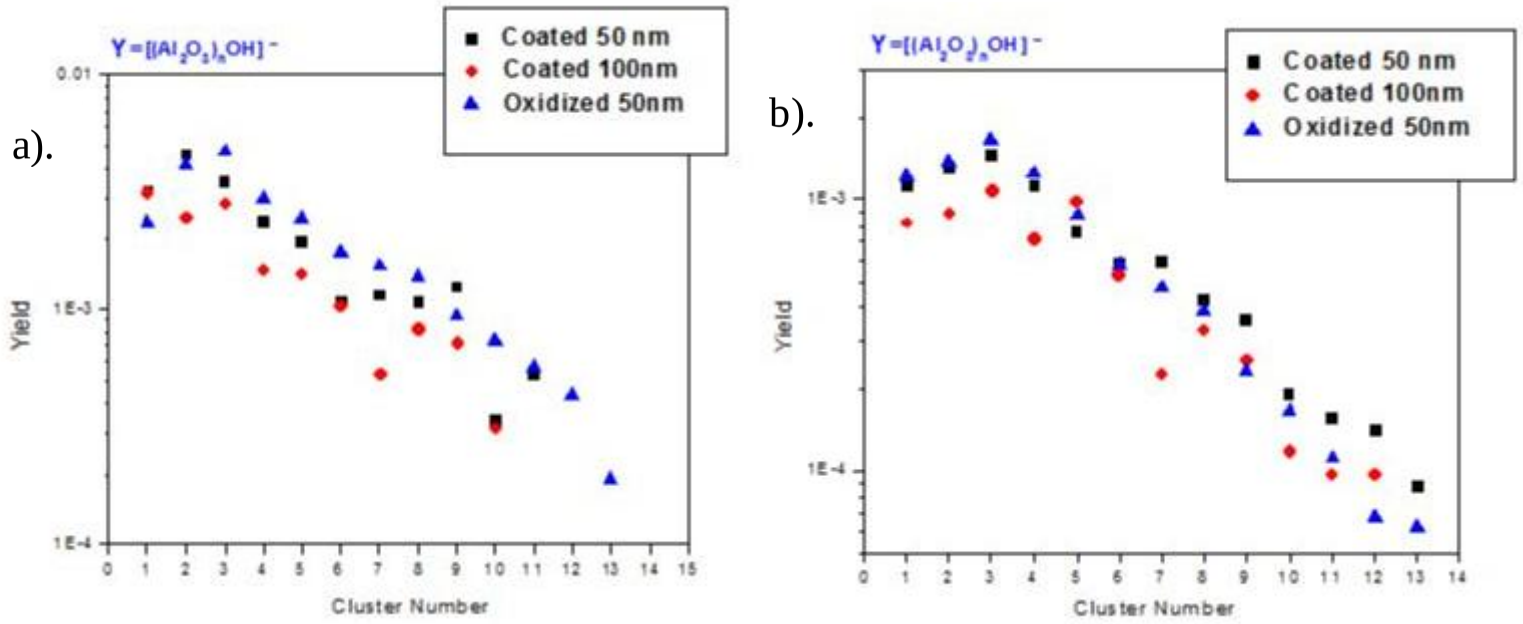

Figure 2.9. Yields of the Al oxide clusters ($[Al_2O_3)_nOH]^-$) as a function of integer n in the molecular formula for the 3 samples with a). 136 keV Au_{400}^{4+} and b). 26 keV C_{60}^{+}.

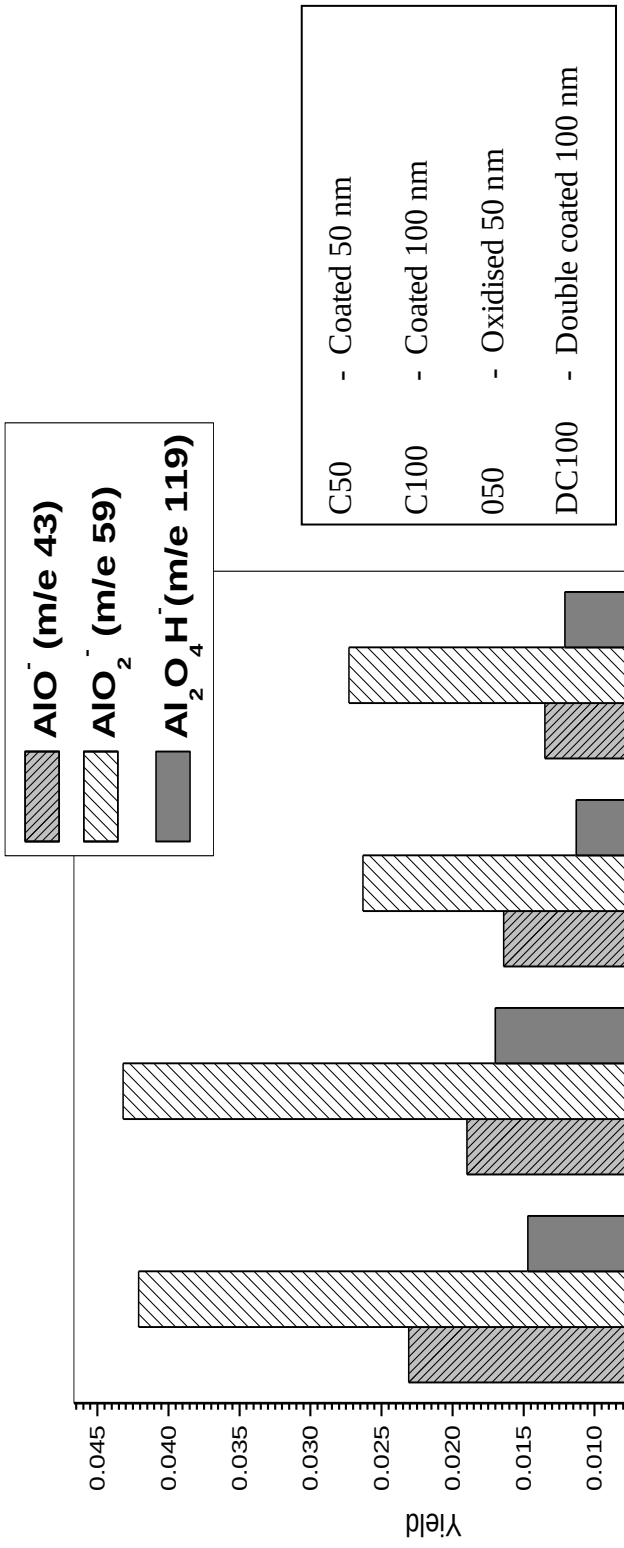

Figure 2.10. Comparative yield s of the lower mass Al oxide ions for the 4 samples when bombarded with Au_{400}^{4+} projectile at 136 keV total impact energy.

However, the yield of AlO_2^- (m/e 59) does not follow a similar trend as the AlO^- and $Al_2O_4H^-$ ions. This is true for both the coated particles. The degree of coating cannot be determined as an absolute value, since the signal of SIs is a function of ionization/detection efficiency.

This efficiency depends on a few variable experimental parameters.[123] However, the relative degree of coating, β, can be extracted from the experimental data for the two palmitic acid coated samples. In the equations and tables below, the 50 nm coated NPs will be represented by symbol A and 100 nm coated NPs will be represented by symbol B for simplicity.

$$\beta = \left(\frac{N_{\text{M-H}}}{n_0}\right)_{\text{A}} \Big/ \left(\frac{N_{\text{M-H}}}{n_0}\right)_{\text{B}} = \frac{p_{\text{A}}}{p_{\text{B}}} \qquad \text{Eq. 2.1}$$

where $N_{\text{M-H}}$ denotes the number of deprotonated palmitic acid ions $(M\text{-}H)^-$ detected, n_0 is the total number of projectile impacts. The degree of coating, p, is $p = S_{M-H}/S_0 = n_{M-H}/n_0$, where S_0 is the average surface area of a NP; S_{M-H} is the average coated area; and n_{M-H} is the number of projectile impacts on the coated areas. The comparison of the specimens A and B gives $\beta = 0.7 \pm 0.05$. Thus, the particles from the specimen B have a better SAM coverage. The average uncoated area of the particles from the specimen A is at least 30%.

As noted at the outset, the ability to detect individual mass spectra corresponding to the SAM area of the NPs prompts questions about the relative thickness of the

different oxide layers (layer beneath SAM, and layer from uncoated area), and about the effect of exposure to air on the thicknesses of these layers.

It must be noted that variations in oxide thickness may only be detected within the depth of SI emission. Thus, oxidation beyond ~10nm will not be recognized.

The value of the relative thickness of the oxide layer beneath the SAM can be extracted from the experimental data by the following calculations. The number of deprotonated palmitic acid ions $(M\text{-}H)^-$ detected, $N_{M\text{-}H}$, can be expressed as follows:

$$N_{M\text{-}H} = n_{M\text{-}H} Y_{M\text{-}H} \qquad \text{Eq. 2.2}$$

where $Y_{M\text{-}H}$ is the yield of $(M\text{-}H)^-$. Similarly, N'_{AlO_2} is the detected number of aluminum oxide ions $(AlO_2)^-$ which were emitted from coated areas

$$N'_{AlO_2} = n_{M\text{-}H} Y'_{AlO_2} \qquad \text{Eq. 2.3}$$

where Y'_{AlO_2} is the yield of $(AlO_2)^-$ emitted from coated areas. The co-emission of $(M\text{-}H)^-$ with aluminum oxide ion $(AlO_2)^-$ represented by $N_{AlO_2,\,M\text{-}H}$ can be expressed as

$$N_{AlO_2,\,M\text{-}H} = n_{M\text{-}H} Y_{AlO_2,\,M\text{-}H} \qquad \text{Eq. 2.4}$$

Considering that for cluster bombardment $Y_{AlO_2,\,M\text{-}H} = Y'_{AlO_2} Y_{M\text{-}H}$,[108] the combination of expressions 2.2, 2.3 and 2.4 gives

$$Y'_{AlO_2} = N_{AlO_2,\,M\text{-}H} / N_{M\text{-}H} \qquad \text{Eq. 2.5}$$

As indicated earlier, the emission depth of secondary ions is ≤10 nm. The thickness of the self-assembled monolayer is well defined (length of palmitic acid chain is of ~3 nm).

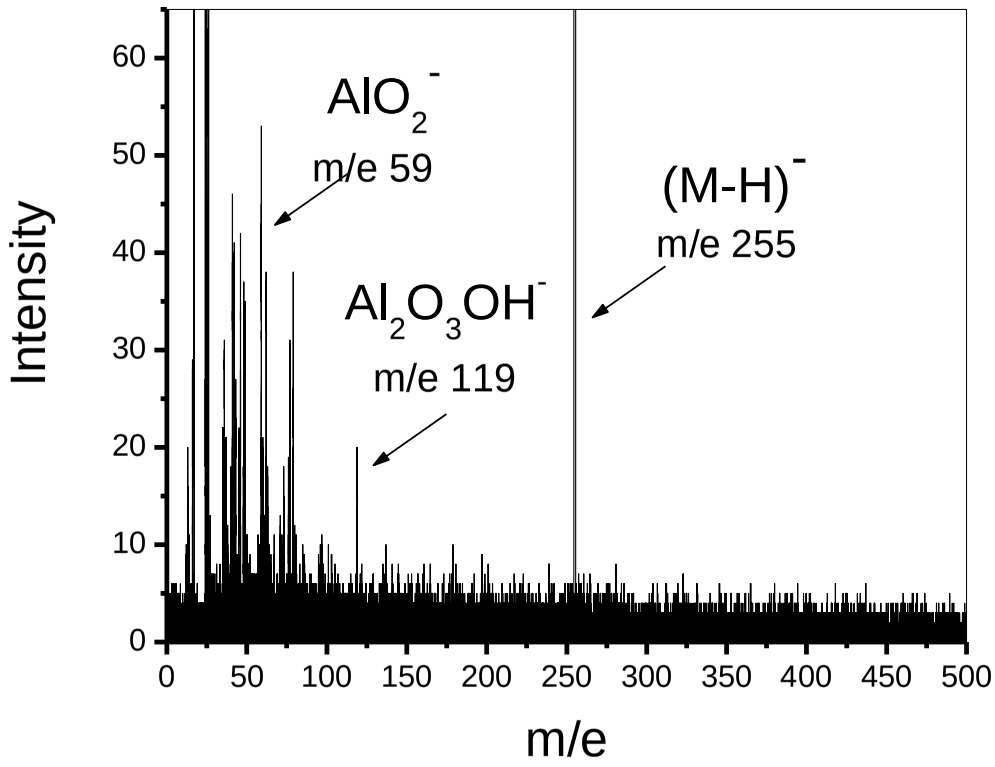

Figure 2.11. Negative ion mass spectrum of ions co-emitted with palmitic acid ion (50 nm coated NPs). The mass spectrum was acquired with ~2 million impacts of 136 keV Au_{400}^{4+}.

Thus, the yield Y'_{AlO_2} reflects the thickness of the aluminum oxide interface layer beneath the SAM. An interesting feature of the coincidental (effective yield?) values used here is that Y'_{AlO_2} is independent of the number of projectiles hitting the SAM area of NPs. Values of Y'_{AlO_2} from different samples can thus be directly compared. The expressions (2.3-2.5) are suitable for any sort of aluminum oxide cluster ions co-emitted with palmitic acid ions, e.g. $(Al_2O_3)OH^-$ (Figure 2.11).

The yield of aluminum oxide ions emitted from the total surface (area beneath the SAM and uncoated area) of the NPs can again be calculated from the number of the co-emitted aluminum oxide cluster ions of the different type, e.g. AlO_2^- and $(Al_2O_3)OH^-$:

$$Y_{AlO_2} = N_{AlO_2,\,Al_2O_3OH} / N_{Al_2O_3OH} \qquad \text{Eq. 2.6}$$

The yields Y'_{AlO_2} and Y_{AlO_2} calculated for the 50 nm coated particles (specimen A) and 100 nm coated particles (specimen B) are shown in Table 2.1. The ratio of the SI yields, $Y_{AlO_2}{}' / Y_{AlO_2}$, is ~1 for both specimens, indicating that the short exposure in the air (~10 min) does not increase the degree of oxidation of the uncoated areas. The ratios of yields $(Y_{AlO_2})_A / (Y_{AlO_2})_B$ and $(Y'_{AlO_2})_A / (Y'_{AlO_2})_B$, are ~2, which show that the better coated NPs from specimen B ($\beta = 0.7$) have half the thickness of the oxide layer.

One must assess the contribution of interfacial impacts, i.e. projectile impacts on the boundaries between surface areas of SAM and uncoated aluminum oxides. The magnitude of the interfacial contribution can be evaluated with an "interference coefficient" which can be defined as follows:

Table 2.1. Yields of aluminum oxide cluster ions emitted from specimens coated 50 nm and coated 100 nm NPs. The yield, Y_{AlO_2}, corresponds to the total surface of the nanoparticle (SAM coated and uncoated). Y'_{AlO_2}, is the yield of ions emitted from the SAM coated area. The accuracy of yield measurements is ±10%.

	Y'_{AlO_2}	Y_{AlO_2}	$(Y_{AlO_2})_A/(Y_{AlO_2})_B$	$(Y'_{AlO_2})_A/(Y'_{AlO_2})_B$
Coated 50 nm (A)	0.11 ± 0.01	0.13 ± 0.01	1.9 ± 0.2	2.0 ± 0.2
Coated 100 nm (B)	0.06 ± 0.005	0.07 ± 0.005		

$$K = \frac{(N_{AlO_2,\,M\text{-}H})_{int}}{N_{AlO_2,\,M\text{-}H}} \qquad \text{Eq. 2.7}$$

where $(N_{AlO_2,\,M\text{-}H})_{int}$ is the interfacial contribution, i.e. the number of aluminum oxide ions emitted from the uncoated areas and detected as co-emitted with palmitic acid ion; $N_{AlO_2,\,M\text{-}H}$ is the number of aluminum oxide ions emitted from SAM areas and detected as co-emitted with palmitic acid ion. To calculate K, we use a model of interference where the interference area at the surface of the NP, S_{int}, is larger than the interference area between neighboring NPs (apposition of spherical objects). Considering that $n_{int}/n_{M\text{-}H} = S_{int}/S_{SAM}$, where n_{int} is the number of impacts on the interference area, and S_{SAM} is the area of NP coated by SAM, we obtain

$$K = \frac{Y_{AlO_2}}{Y'_{AlO_2} n_{M\text{-}H}} \sum_{i=1}^{n_{int}} \frac{x_i d - x_i^2}{d^2} \qquad \text{Eq. 2.8}$$

where d is the diameter of the emission area (~ 10nm); and x_i is the random distance between the point of impact and the boundary of SAM ($d \geq x_i \geq 0$).

The values of K vs. the degree of coating, p, are given in Figure 2.12. Using Figure 2.10 one can estimate the accuracy of the single impact measurements. K should be smaller than the precision of our experiment (±10%). For the large variations of the ratio Y_{AlO_2}/Y'_{AlO_2}, K is below 0.2 when the degree of coating is not too low ($p \geq 0.4$).

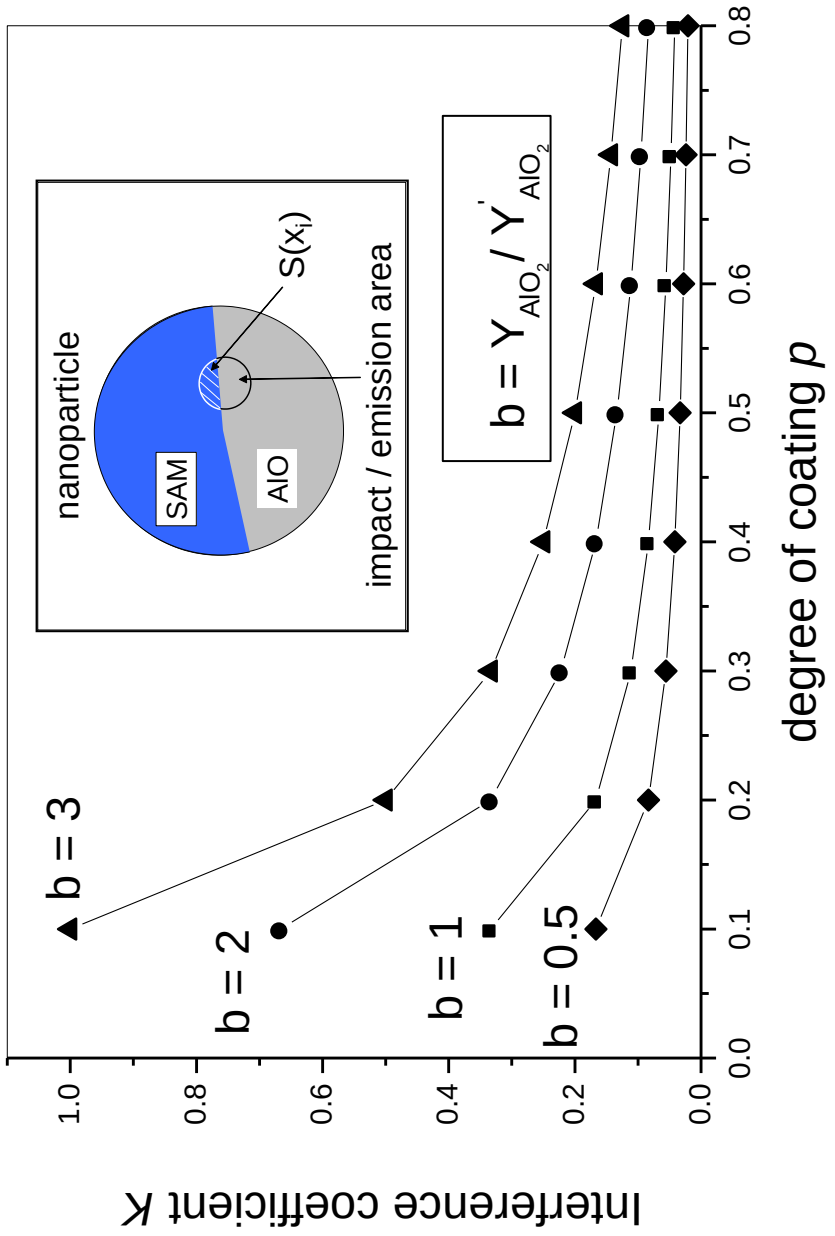

Figure 2.12. "Interference coefficient" K as a function of the degree of particle coating *p*.

Thus, the spatial resolution of the technique is approximately twice that of the diameter of the emission area (~10 nm). The accuracy of the single impact measurements becomes unacceptable for oxidized NPs having largely deficient SAM coverage ($K > 0.2$, $p < 0.4$).

Conclusion

SIMS in the single cluster impact mode, uniquely combines the analytical versatility of surface mass spectrometry with ~20 nm spatial resolution. The method requires a large number of impacts (~10^6) to obtain analytically significant information. Yet its "nanoprobe" feature is retained by analyzing the ionized ejecta from each impact independently. The detection limit, under the experimental conditions of this study, is ~ 10^2 attomole for small MW organics such as palmitic acid. The scope of applications remains to be explored. The method should be useful for determining if further oxidation occurs in SAM-protected areas under prolonged air exposure. For instance, do the uncoated areas stimulate oxidation beneath those covered by SAM? It can also examine the relationship between the initial oxide thickness and the quality of the SAM coverage. An important added capability, namely the combination of the single projectile impacts with the concurrent real-time localization of each impact, is in progress.

CHAPTER III

CHARACTERIZATION OF INDIVIDUAL Ag NANOPARTICLES AND THEIR CHEMICAL ENVIRONMENT*

Introduction

Thiol-capped metallic NPs are of increasing interest because of their optical, magnetic or reactive peoperties.[124-126] These properties significantly differ from the bare or bulk counterparts, with these changes being modulated by the size and the capping. A further notable feature of capped metal NPs in size of 1 to 10 nm is that they assemble a self-assembled organization.[127] Such metal nanostructures deposited in organic matrices have applications as optical or electronic devices. The morphology of these assemblies can be determined with TEM and AFM.[128,129] The resulting physical description assumes knowledge of the chemical identity and integrity of the nano-objects and their surroundings. However, isotopic and molecular characterization at the spatial scale of physical microscopy remains an elusive goal. We present here the application of SIMS yielding non-imaging, yet spatially resolved information approaching that of microscopy techniques. In the experiments described below, mass spectrometric data are extracted from nanovolumes (~10 nm^3) by running SIMS in the event-by-event bombardment/detection mode. In this approach ionized ejecta are identified from single

*Parts of this chapter are reprinted with permission from *Analytical Chemistry*, Volume 81, S. Rajagopalachary, S.V. Verkhoturov, and E. A. Schweikert, Characterization of Individual Ag Nanoparticles and their Chemical Environment, 1089-1094, 2009. Copyright [2009] American Chemical Society.

projectile impacts i.e. from an area ~10 nm in diameter and depth. Under these conditions the effectiveness of the bombarding ion is critical for generating secondary ions. Recent SIMS literature has focused on enhanced SI yields obtained with polyatomic and massive projectiles (e.g. Au_3^+, Bi_3^+,C_{60}^+, Au_{400}^{4+}) accelerated to keV energies.[99,100,130-132] Silver NPs of ~ 5 nm diameter deposited in a single layer on glycine were examined with cluster SIMS in the event-by-event bombardment/detection mode. The projectiles used were Au_3^+, C_{60}^+ Au_{400}^{4+} with impact energies of 34 keV, 26 keV and 136 keV respectively. The importance of the projectile characteristics for maximizing chemical and morphological information from single impacts is illustrated here with event-by-event bombardment/detection experiments with Au_3^+, C_{60}^+ and Au_{400}^{4+}. The model target used to test the ability of "shot-by-shot" SIMS to characterize metal nano-assemblies consisted of capped Ag NPs (~ 5nm) deposited on a glycine substrate.

Figure 3.1 presents a TEM image of the Ag NPs on glycine vapor deposited on the formvar coating of a TEM grid. The figure depicts three distinct areas on the grid. First, a regular arrangement of the particles forming a uniform single layer as previously noted.[127] The polar sulfur group ligates to the metal surface while the alkane chain creates a boundary that insulates the reactive metal particles from each other, preventing aggregation.[133] Second, there are darker regions where more than one layer of particles is seen as well as empty areas which are void of the Ag NPs, i.e. the underlying glycine is exposed.

(a)

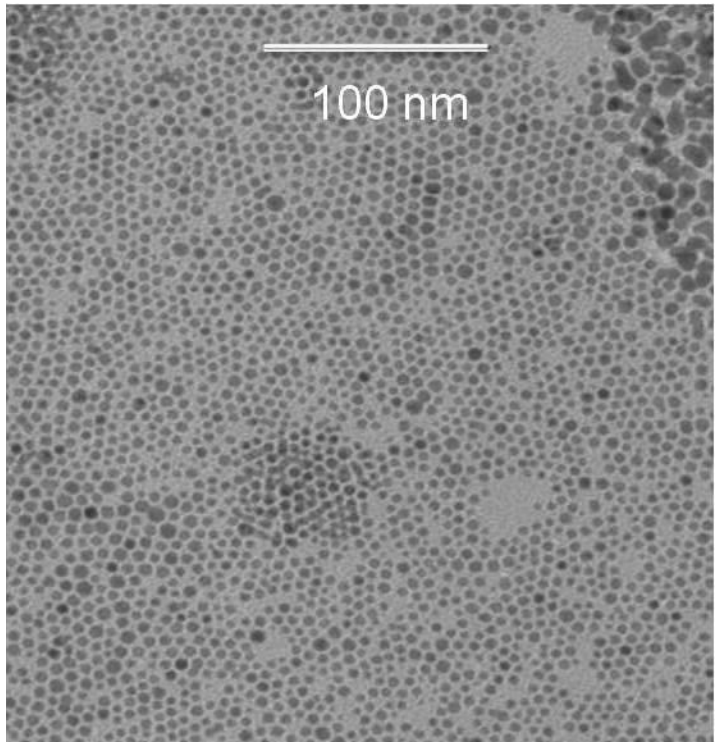

Figure 3.1. (a) TEM image of the decanethiol functionalized Ag NPs (~5nm) in hexane with 2 μL deposited on a glycine coating on a TEM grid.

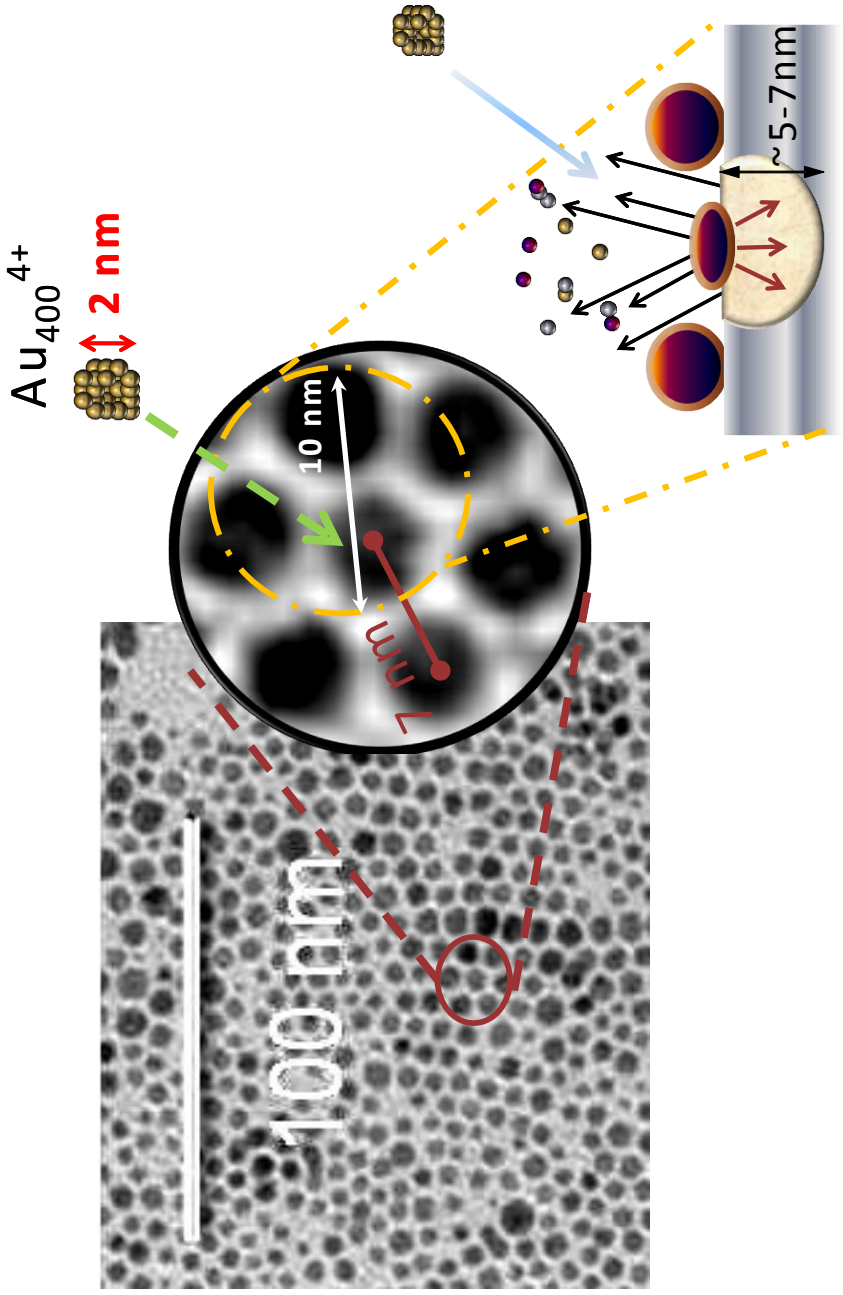

Figure 3.1. continued, (b) enlarged portion of the TEM grid showing a schematic illustration of the impact of the Au_{400}^{4+} projectile on the NPs probing a nanovolume that is 10 nm in diameter and 10 nm in depth.

Experimental Section

For the SIMS experiment, the samples were made by first vapor depositing glycine (Sigma-Aldrich) on a stainless steel surface which results in a thickness of ~ 5 μm. Then a 15 μL aliquot of 1mg/mL of 5 nm decanethiol functionalized Ag NPs (Sigma Aldrich) in hexane, was drop cast on top of the glycine surface. TEM images of the NPs taken before and after vapor deposition of glycine on the formvar of the TEM grid showed the distribution of the particles to be similar in both cases. As glycine is insoluble in hexane, the vapor deposition morphology of glycine was unaffected by the deposition of the Ag NPs. This was verified by comparing scanning electron microscopy (SEM) images of the sample before and after deposition of the Ag NPs.

The samples were analyzed with two different cluster-SIMS instruments, before and after the deposition of the Ag NPs. One instrument is equipped with a gold LMIS and the other with an effusion C_{60} source, as described in the previous chapter. The mass resolution ($m/\Delta m$) for the Au LMIS instrument was typically between 900 and 1000 for the glycine dimer peak Gly_2^- (m/z 149) in the negative ion mass spectra. The mass selected cluster projectiles used in this study are Au_{400}^{4+} accelerated to 136 keV and Au_3^+ accelerated to 34 keV. The C_{60}^+ was accelerated to 26 keV total impact energy. In all cases, approximately two million impact/emission events were stochastically sampled over a spot with a diameter of ~2mm.

Results and Discussion

An excerpt of a mass spectrum of Ag NPs deposited on glycine is presented in Figure 3.2 with the same mass range from a neat glycine shown for comparison. Both were obtained with 136 keV Au_{400}^{4+} and are normalized to the same number of impacts. The presence of the Ag NPs is demonstrated with the observation of the peaks Ag^-, $Ag(CN)_2^-$ and $AgSC_2^-$. Negative values do not have physical significance, rather they were a means to compare both the spectra on the same mass scale. It should be noted that the height of the peak (normalized intensities) do not reflect the relative abundance of the isotopes of Ag, but the peak area does. The overall spectra (Figure 3.3) for both the Ag NP/glycine, and the neat glycine samples also contain the distinct $AuGly^-$ and $Au(CN)_2^-$ peaks obtained by Au_{400}^{4+} bombardment.[134] The unexpected occurrence of $Ag(CN)_2^-$ was verified with isotopically labeled ^{15}N-glycine (Sigma Aldrich). Indeed, a shift in two mass units is seen for the adducts represented by Ag $(C^{15}N)_2^-$ (Figure 3.2 b). Surprisingly, there are split peaks for $^{109}Ag(C^{15}N)_2^-$ and $^{107}AgSC_2^-$, both nominally at m/z 163. A more detailed examination (Figure 3.2 c) shows a difference in the respective peak locations. The flight time delay exceeds the deficit (0.02779 a.m.u) in the exact mass of $^{109}Ag(C^{15}N)_2^-$ vs. that of $^{107}AgSC_2^-$. The difference is attributed to delayed emission of $AgSC_2^-$, perhaps reflecting metastability of the silver decanethiol moiety. The broader peaks of $AgSC_2^-$, in comparison to other peaks in the spectrum, are a further indication of delayed emission. The adduct $Ag(C^{15}N)_2^-$ is the result of a multi-step process during single projectile impacts ("super-static" regime), whereas the $AgSC_2^-$ ions

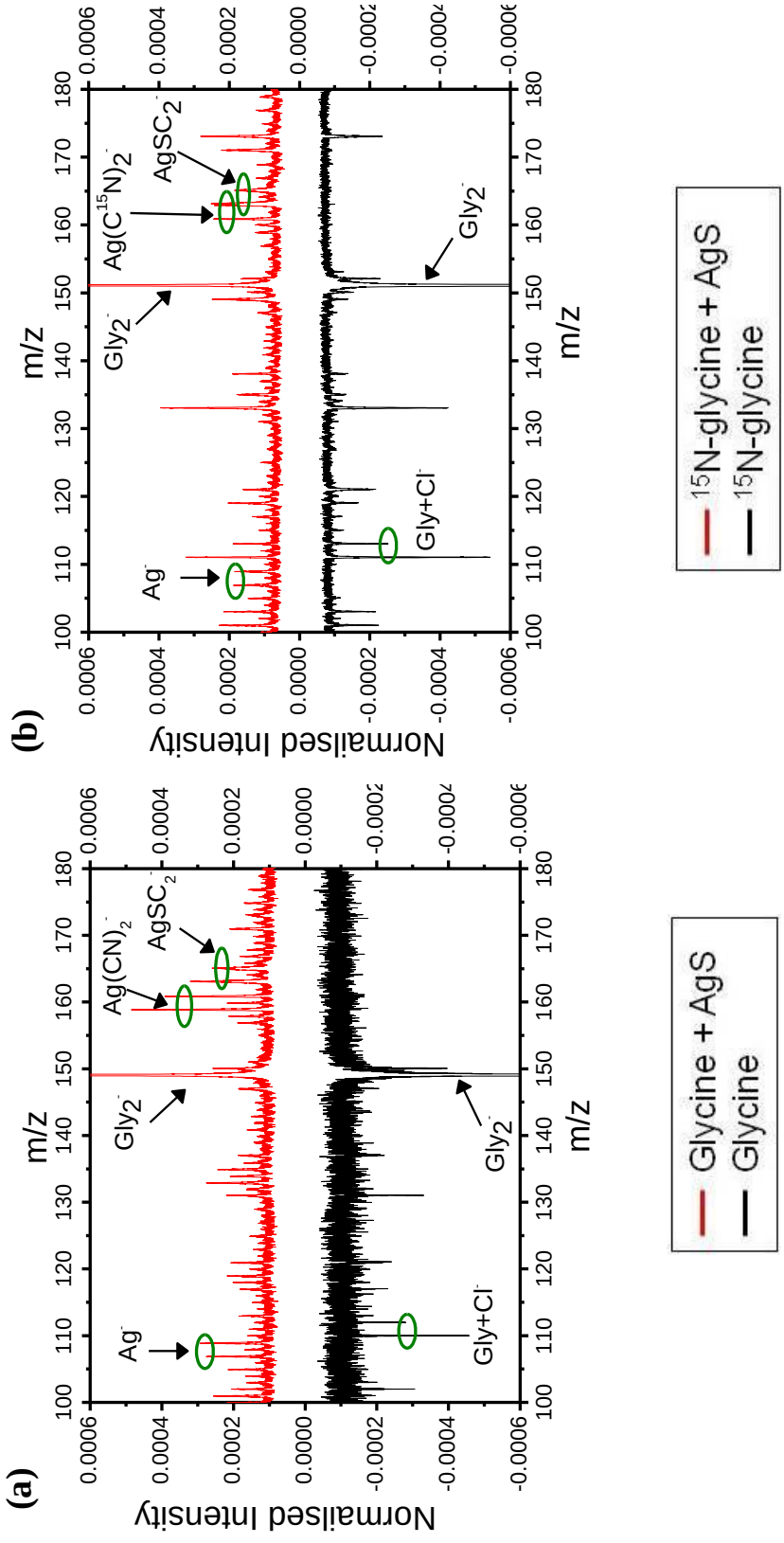

Figure 3.2. Negative ion mass spectra for (a) glycine with AgNPs on top (red) and glycine represented on the negative half (black) of the y-axis, (b) ^{15}N-glycine with Ag NPs on top and ^{15}N-glycine on the negative half.

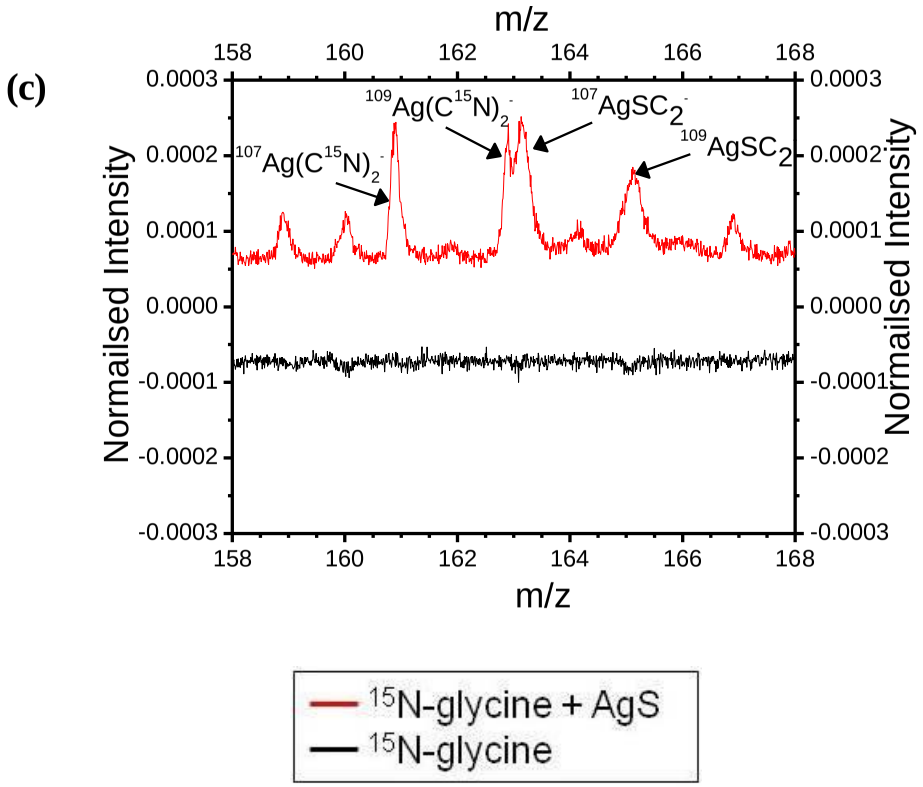

Figure 3.2. continued, (c) a magnified version from the mass range from 158 to 168 of the ^{15}N-glycine sample representing peak splitting at m/z 163. The spectra were obtained under Au_{400}^{4+} bombardment at 136 keV total

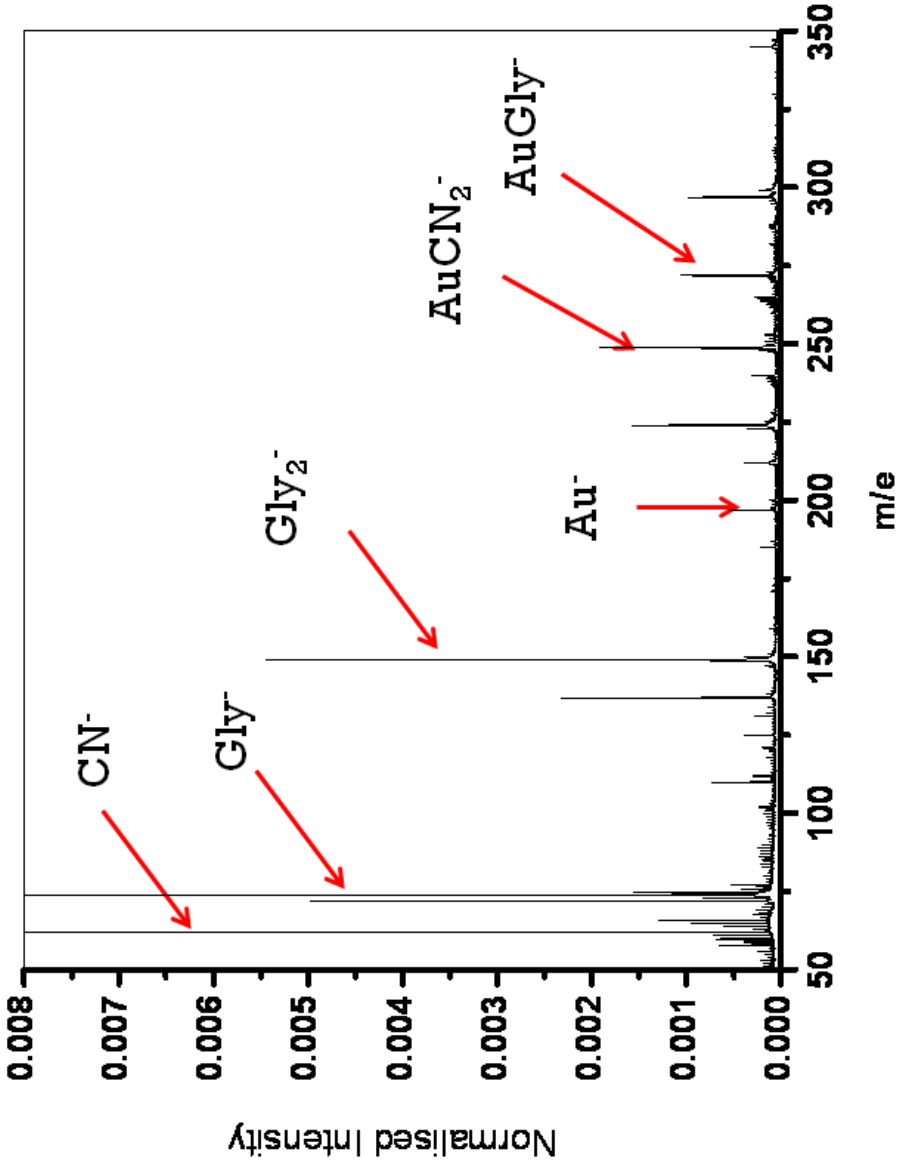

Figure 3.3. Negative ion mass spectrum of a vapor deposited sample of glycine bombarded by 136 keV of Au_{400}^{4+}.

are due to the surface sputtering of the Ag NPs. Silver/glycine adducts must originate from the atoms shattered from Ag NPs combining with CN^-, which is synthesized from glycine fragmentation. Indeed, a NP represents a finite system where the energy deposited from the impact cannot be dissipated in the same manner as in a bulk solid.[135] Accordingly, it can be expected that the NP completely disintegrates if the energy density deposited in the NP exceeds it total binding energy.[136] This condition is largely met with a Au_{400}^{4+} , C_{60}^{+} or Au_9^{+} (Figure 3.4) impact with the energies used here,. The "NP atomization cum substrate-molecule fragmentation-recombination" observed here has, to our knowledge, not been reported. A simpler process where Au atoms ablate from an impacting massive Au projectile and then recombine with fragments from target molecules, with particular amino acids, has been documented previously.[134] In a similar way, target-projectile adducts have also been detected when nm-size Ag grains were impacted with individual massive iron particles.[137]

Returning to Figure 3.2, the presence of $Ag(CN)_2^-$ indicates that the Ag NPs were dispersed as a single layer on glycine, confirming the morphology shown in Figure 3.1 Indeed, the depth of SI emission from 136 keV Au_{400}^{4+} impacts is ≤ 10 nm, thus $Ag(CN)_2^-$ could not be produced from multiple layers of Ag NPs on glycine.

The effectiveness of various projectiles for the characterization of the Ag NP assemblies on glycine can be assessed with the SI yield (expression 3.1).

$$Y_A(\%) = 100\sum_{x_A} \frac{x_A N(x_A)}{N_{\mathrm{Tot}}} = 100\sum_{x_A} x_A P(x_A) \qquad \text{Eq. 3.1}$$

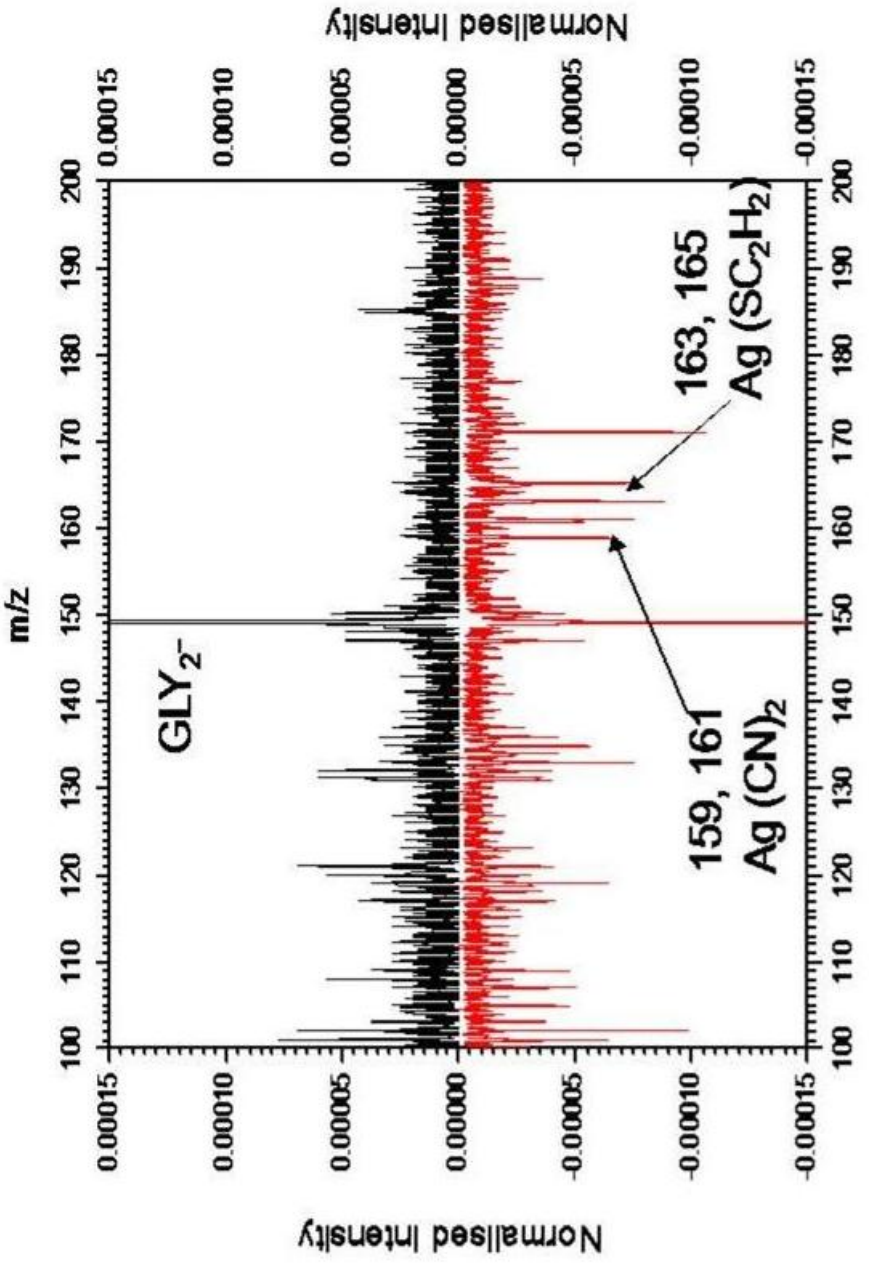

Figure 3. 4. Negative ion mass spectrum of glycine on top (black) and glycine with Ag NPs represented on the negative half (red) of the y-axis. The spectra were obtained under Au_9^+ bombardment at 34 keV total impact energy.

Where x_A is the number of SIs of type A detected in a single impact/emission event; $N(x_A)$ is total number of events where ion A is detected; $P(x_A)$ is the probability distribution of the number of ions detected per impact/emission event and N_{Tot} is the total number projectile impacts.

The data from Au_3^+, C_{60}^+ and Au_{400}^{4+} at impact energies representative of practical SIMS conditions are presented in Table 3.1. The SI yields follow trends generally observed for C_{60}^+ vs. Au_3^+ or Bi_3^+.[138, 139] The Au_{400}^{4+} projectile has the distinct feature of being efficient for the production of high SI yields and SI multiplicities. The latter is evidenced with Ag and Au-adducts from glycine. Further results presented below focus on data obtained with Au_{400}^{4+}.

A rough estimate of the coverage of the glycine surface by the Ag NPs can be obtained by calculating the decrease in SI yields from the neat glycine sample. Table 3.2 shows the yield percentage for these ions before and after the deposition of the Ag NPs obtained with impacts from the Au_{400}^{4+} projectile. The yield change ratio is calculated by dividing the yield before deposition, by that after deposition. The yields of CN^-, glycine molecular ion and the dimer decrease approximately three-fold after the deposition of the Ag NPs. The yield of gold adducts, $Au(CN)_2^-$ and $Au(Gly)^-$ decrease because of the physical coverage by the Ag NPs and the concurrent production of silver adducts. The projectile is the only source of gold atoms, hence, the more abundant silver is able to competitively scavenge the glycine ions to form adducts. In contrast to other SIs, the yield of re-emitted gold increases in the presence of the Ag NP. This observation is discussed further below.

Table 3.1. Percentage yields of negative secondary ions from the glycine sample after the deposition of Ag NPs for various projectiles. * Indicates the absence of the peak. The precision of the values are ±5%.

Ion	m/z	Au_{400}^{4+} Yield	Au_3^+ Yield	C_{60}^+ Yield
CN^-	26	13.45	1.46	4.22
Gly^-	74	17.82	9.1	4
Gly_2^-	149	3.55	9.79	5.36
Au^-	197	2.31	*	*
$AuCN_2^-$	249	3.36	*	*
$AuGly^-$	272	1.6	*	*
Ag^-	107	0.54	0.08	0.08
$AgCN_2^-$	159	0.91	0.03	0.06
$AgSC_2^-$	163	1.19	0.27	0.27

Table 3.2. Percentage yields of negative secondary ions from glycine before and after deposition of Ag NPs obtained with Au_{400}^{4+} projectiles accelerated to 136 keV total impact energy. The yield change ratio is obtained by dividing the yield before the deposition by the yield after. .The precision of the values are ±5%.

Ion	*m/z*	*Gly Yield*	*Gly + Ag-S Yield*	*Yield Change Ratio*
CN-	26	38.6	13.4	2.9
Gly^-	74	63.3	17.8	3.5
Gly_2^-	149	11.4	3.5	3.2
Au^-	197	1.3	2.3	0.5
$AuCN_2^-$	249	4.4	3.4	1.3
$AuGly^-$	272	2.4	1.6	1.5

As previously noted, the shot-by-shot bombardment/detection allows to identify ejecta from individual desorption nano-volumes of 10 nm in diameter. Accordingly, in the present case, the sequence of single impacts can impact either a site containing one Ag NP or a site appearing as a neat glycine surface. A likely species to uniquely originate from the latter is Gly_2^-. An advantage of the event-by-event mode is that the events where Gly_2^- was detected can be extracted from the compilation of individual impact data. The resulting mass spectrum, which is the "Gly_2^- coincidence ion mass spectrum" is presented in Figure 3.5. The spectrum shows abundant co-emission of Gly^- and CN- with Gly_2^- and negligible occurrence of Ag-containing SIs (≤ 1% relative to Gly_2^-). The assignment of Figure 3.5 pertaining to sites of neat glycine can be verified by computing the "effective yield" for Gly_2^- which corresponds to the number of the Gly_2^- detected divided by the number of impacts on neat glycine. As defined, the "effective yield" should be the same for the Gly_2^- emission from a large neat glycine surface as from the neat glycine sites on the surface examined here. The "effective yield" can be obtained from the experimentally detected co-emission events, provided the SIs are ejected independent of each other, i.e. the co-emission occurs at the frequencies expected from statistics. This is the case of Gly_2^- we can consider co-emission with Gly^- (based of Figure 3.5); the probability of their co-emission is expressed as follows

$$P_{(Gly_2,Gly)} = P_{Gly_2} \cdot P_{Gly} \qquad \text{Eq .3.2}$$

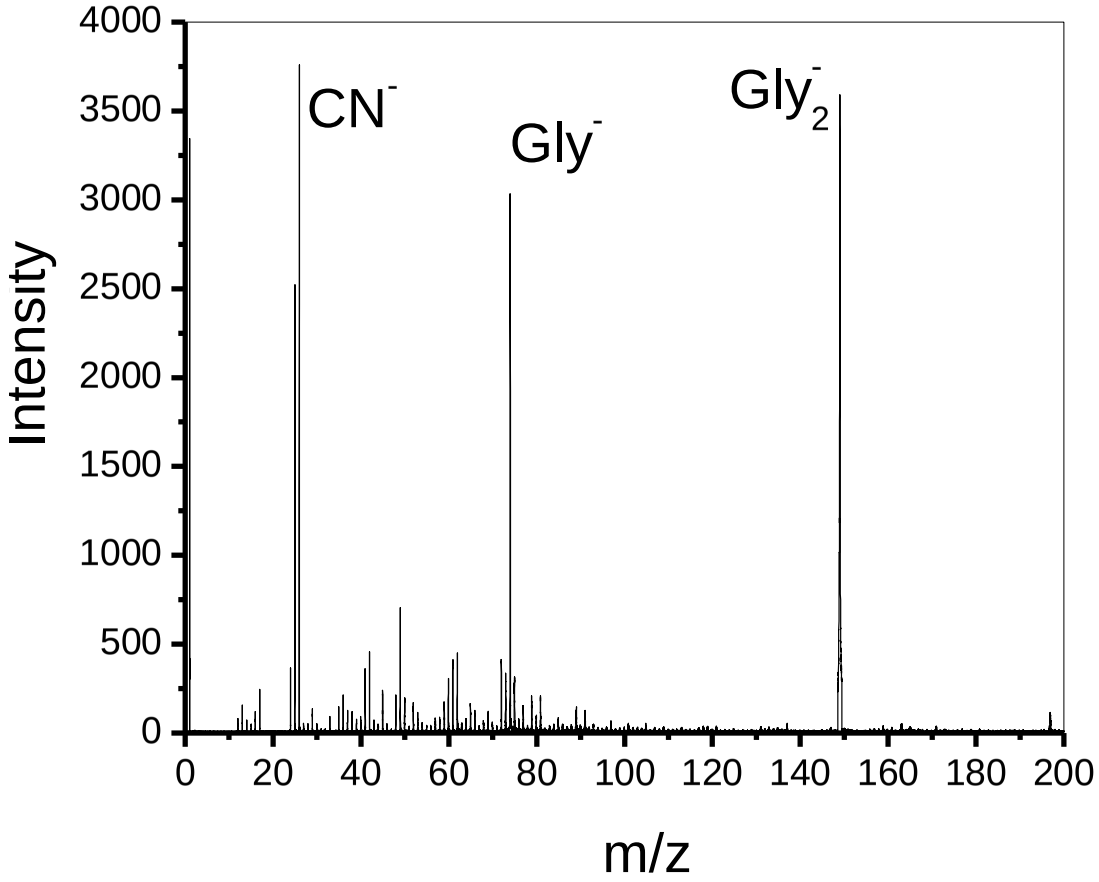

Figure 3.5. Negative ion mass spectrum of ions co-emitted with Gly_2^- ion. The mass spectrum was acquired with ~2 million impacts of 136 keV Au_{400}^{4+}.

The probability can be extended to the yield Y,[102] which is the number of SIs detected, I, divided by the number of impacts N.

$$Y_{(Gly_2,Gly)} = Y_{Gly_2} \cdot Y_{Gly} \qquad \text{Eq .3.3}$$

Hence,

$$Y_{Gly_2} = \frac{Y_{Gly_2,Gly}}{Y_{Gly}} \qquad \text{Eq. 3.4}$$

Under our experimental conditions, Y_{Gly_2} had values of 0.65 and 0.42, respectively for neat glycine and for the assumed neat glycine from the gly-Ag NP surface. The ~ 30% lower value for the complex covered surface is attributed to a preferential Gly_2^- emission at a forward angle with respect to the incident projectile.[140] Hence a neighboring Ag NP might block the forward trajectories of some Gly_2^- .

The rough agreement between the effective yields supports the idea that Gly_2^- and Gly^- are predominantly signals from neat glycine sites. Thus, the corresponding yield contains the effective number of impacts on neat glycine sites, which relates to the area not covered by Ag NPs. The assumption noted is related to Eq. 3.2 and can be re-stated as a correlation coefficient, Q, of unity:

$$Q_{Gly_2Gly} = \frac{\sum_{x_{Gly_2}} \sum_{x_{Gly}} x_{Gly_2} x_{Gly} P(x_{Gly_2} x_{Gly})}{\sum_{x_{Gly_2}} x_{Gly_2} P(x_{Gly}) \sum_{x_{Gly}} x_{Gly} P(x_{Gly})} = \frac{Y_{Gly_2Gly}}{Y_{Gly_2} Y_{Gly}} = 1 \qquad \text{Eq.3.5}$$

Thus,

$$N_{Gly} = \frac{I_{Gly_2} \cdot I_{Gly}}{I_{Gly_2,Gly}} \qquad \text{Eq. 3.6}$$

where N_{Gly} is the number of impacts on neat glycine sites, I_{Gly} and I_{Gly_2} are the number of Gly^- and Gly_2^- ions detected respectively while $I_{Gly_2\,Gly}$ is the number of Gly_2^- ions co-emitted with Gly^-. In this experiment

$$\frac{N_{Gly}}{N_{Tot}} = 0.5 \pm 0.04$$

(from an average of 2 runs). It can be deduced that we have an approximate 50% coverage of glycine by Ag NPs.

The data from sites containing Ag NPs can be analyzed in a similar fashion. The most abundant silver containing SIs $^{107}AgSC_2^-$ and $^{109}AgSC_2^-$. The mass spectrum of all ions detected as co-emited with $^{107}AgSC_2^-$ is given in Figure 3.6. Assuming again that the emissions are correlated, the yield data is processed as outlined in expressions (2)-(6), which results in

$$\frac{N_{AgSC_2^-}}{N_{Tot}} = 0.5 \pm 0.06$$

Hence the surface coverage by Ag NPs amount to ~50%, confirming the result obtained from the assay of the neat glycine sites.

We reported above the surprising presence of $Ag(CN)_2^-$ with evidence of a pathway involving fragmentation of the Ag NP. The number of impacts leading to fragmentation can be determined with the methodology already described, using in this case the data relevant to the emissions of $^{107}Ag(CN)_2^-$ and $^{109}Ag(CN)_2^-$. We determined that $470000 \pm 10\%$ impacts were of the kind that can lead to emission of $Ag(CN)_2^-$. They are less frequent than those that can lead to emission of $AgSC_2^-$. The difference in

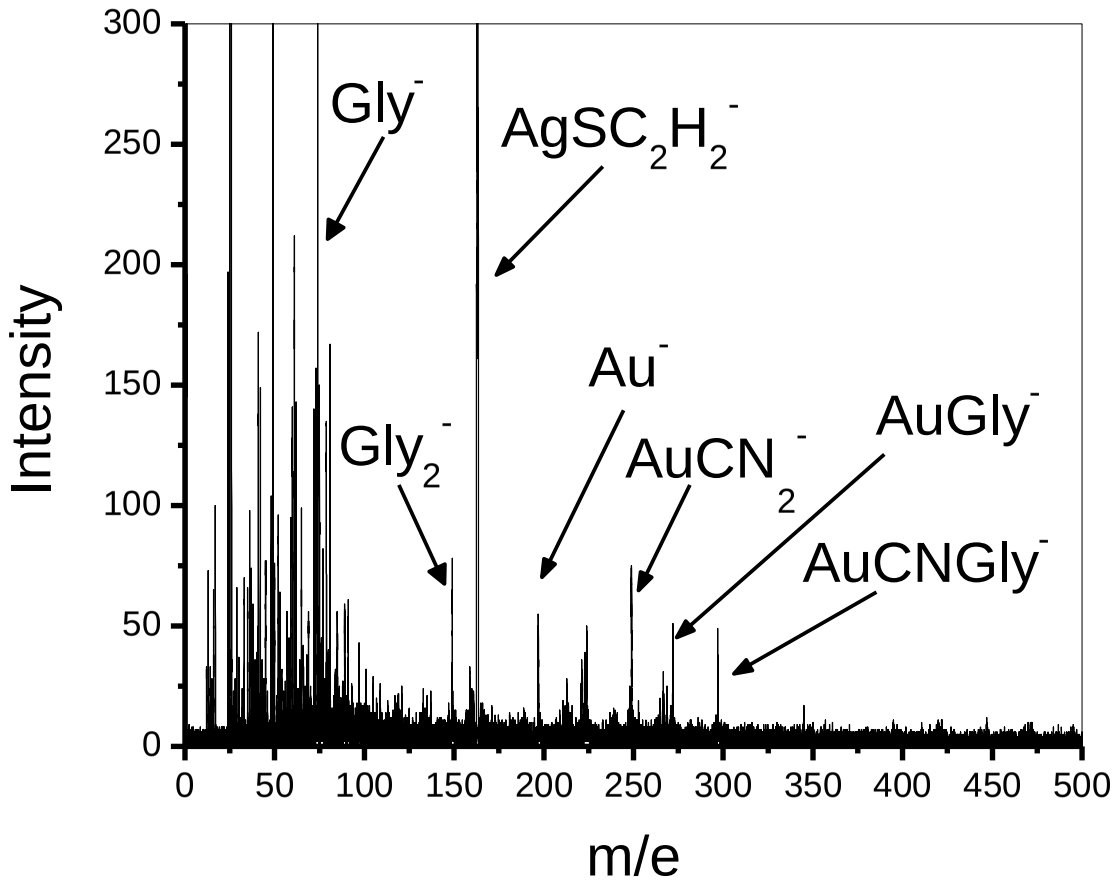

Figure 3.6. Negative ion mass spectrum of ions co-emitted with $AgSC_2^-$ ion. The mass spectrum was acquired with ~2 million impacts of 136 keV Au_{400}^{4+}.

the number of impacts suggests two types of collisions between a Au_{400}^{4+} and a Ag NP. The most likely event is a hit on the outer shell of the NP resulting in the emission of $AgSC_2^-$. Fragmentation as evidenced by $Ag(CN)_2^-$ requires a "bulls-eye" impact. The number of impacts of a given type is proportional to the particle volume from which a specific SI can be emitted. There should be more impacts on the outer layers of the Ag NP than direct hits where the ~ 2 nm projectile fully overlaps with the ~ 5 nm Ag NP. It is interesting to note that in the present case half of the impacts on an Ag NP were direct hits.

An increase in the yield of Au^- when glycine is covered with Ag NPs is reported in table 3.1. A similar trend has been observed when a glycine surface was coated with a 3 – 5 nm layer of Ag.[141] The increase was attributed to enhanced projectile recoil from a metallized surface as opposed to that from an organic surface. A comparison of the Au^- yield increase obtained on a solid layer of Ag vs. neat glycine shows that there is an additional enhancement in the emission of Au^- in the presence of Ag NPs. Given that the NPs amount to a silver coverage of ~50%, the observed yield increase of Au^- is ~ 75% above that expected from scaling the yield increase reported earlier from a full to a 50% coverage. The notably enhanced emission of Au^- in the presence of Ag NP remains to be explored(?).

Conclusion

SIMS in the shot-by-shot bombardment/detection mode allows to extract chemical and morphological information resolved at ~ 10 nm. In the present case, the Ag

NP can be viewed as physical and chemical segregations within the 10 nm sites probed. The method presented here can test single layer dispersion and determine surface coverage. Further since the NPs were examined one-by-one, variations in composition may be revealed, i.e. their classification based on individual tests appears feasible. The data show that grazing vs. direct impacts on NPs can be identified and quantified. It is important to note that massive energetic projectiles are required for generating useful analytical signal from single impacts. The methodology described here allows to examine the chemical environment around individual NPs. Among potential applications is the in-vitro characterization of functionalized NPs and biologically relevant co-located molecules.

CHAPTER IV

CHARACTERIZATION OF A BINARY MIXTURE OF NANOPARTICLES USING CLUSTER SIMS*

Introduction

The characterization of NPs of vanishingly small dimensions, presents new challenges for SIMS. We refer here to nano-objects with dimensions smaller than the secondary ion, SI, emission volume resulting from an individual projectile impact. This case is examined below with C_{60} – SIMS on 5 nm diameter NPs. The volume of the latter is over one order of magnitude smaller than the ~ 10^3 nm^3 from which SI emission occurs following the impact of one individual C_{60} with 20 – 30 keV of kinetic energy.[100] In a "nanoprojectile"-NP collision, the energy deposited from the impact is dissipated different than in a bulk solid. In particular, fragmentation and even complete disintegration may occur if the energy deposited exceeds the NP total binding energy.[135,136] We have reported fragmentation-atomization of 5nm silver NPs under impact of 26 keV C_{60}^+.[142] When the NPs are deposited in a single layer on an organic substrate and analyzed by cluster SIMS via single impacts, a surprising multi-process has been observed, which does not occur in thin (3-5 nm) silver layers covering the same organic substrate.[141]

---

*Parts of this chapter are reprinted with permission from *Surface Interface Analysis*, S. Rajagopalachary, S.V. Verkhoturov, and E. A. Schweikert, Characterization of Individual Nanoparticles with Cluster SIMS, *Submitted*. Copyright [2009] Wiley-Blackwell.

A C_{60}^{+} impact on a silver NP can produce a burst of silver atoms which form adducts with recombined fragments from the substrate molecules, e.g. $Ag(CN)_2^-$.[142] These observations were made with experiments run in the event-by-event bombardment-detection mode. In this approach, a sample with a single layer of NPs is probed with a sequence of individual C_{60}^{+}. The successive impacts occur in a stochastic distribution within a surface area selected for examination. The ionized ejecta from each impact, which originates from a ~ 10 nm diameter spot, are identified by ToF-MS and recorded individually.

In summary, nano-objects of "sub-critical assay dimension" have a SIMS signature which is specific to their physical and chemical characteristics and of their environment. A topic to be addressed is how the SIMS response will be affected in the case of a single layer of NPs of varied composition. We present here a study of a single layer of a mix of NPs of silver and gold.

Experimental Section

Glycine (MW 75.07), histidine (MW 155.16) and guanine (MW 151.13) were purchased from Sigma Aldrich. The Au NPs (5nm) functionalized with dodecanethiol in hexane were purchased from Nanoprobes Inc. Ag NPs (5 nm) functionalized with decanethiol in hexane were purchased from Sigma Aldrich. The integrity and size distribution of the NPs were verified by transmission electron microscopy TEM (Figure 4.1). Further verification of the NPs was also done using energy dispersive X-ray (EDX) analysis . The EDX spectrum for one of the sample (Au NPs) is shown in (Figure 4.2).

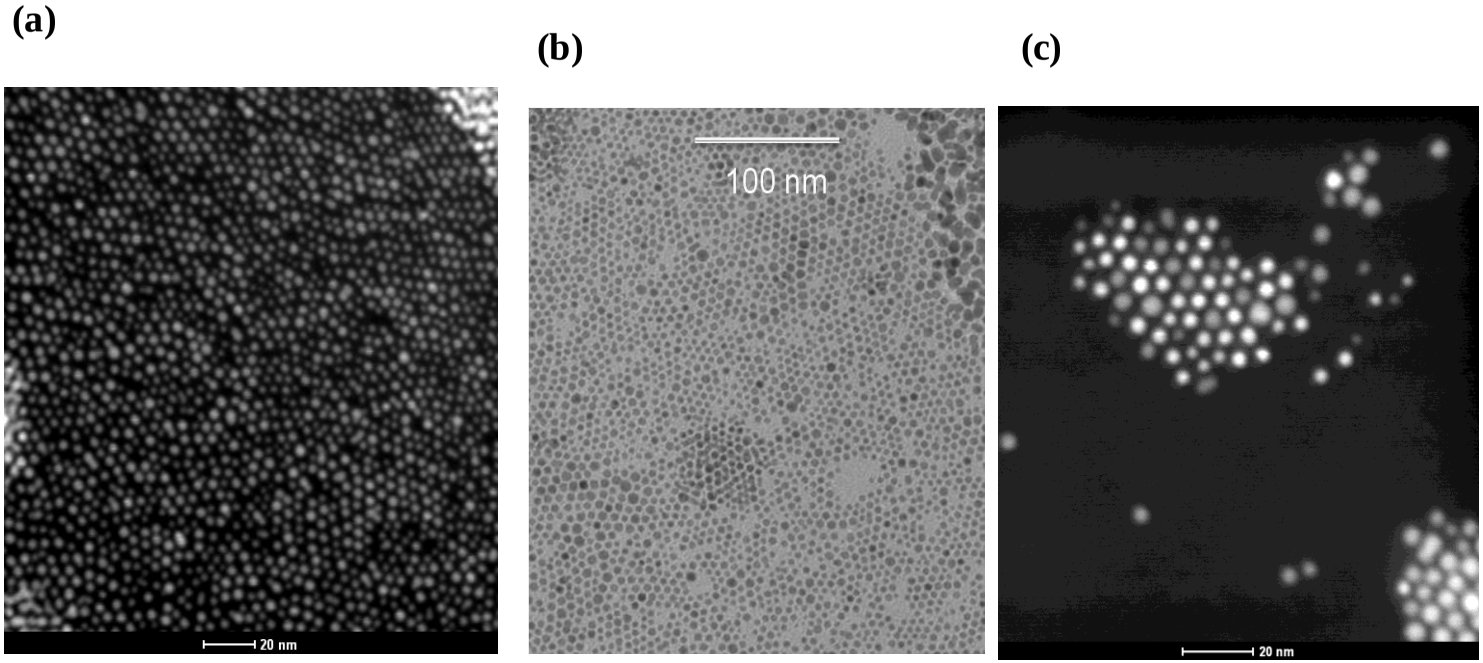

Figure 4.1. TEM images of (a). Au NPs (~5 nm) (b) Ag NPs and (c) a mixture of Au and Ag NPs in hexane deposited as a self organized single layer on a guanine substrate.

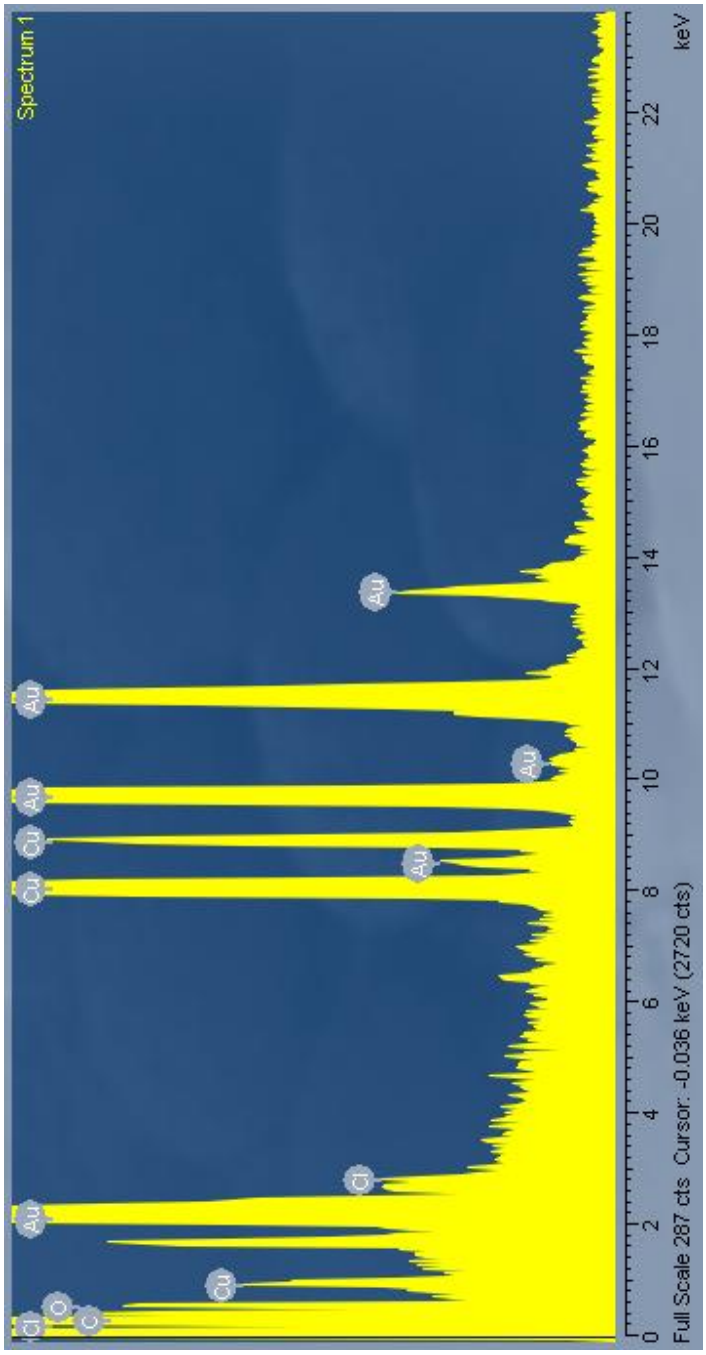

Figure 4.2. EDX spectrum of Au NP 5 nm 0.1 % w/v on a TEM grid with vapor deposited guanine layer.

The NPs were first analyzed by drop casting 15 μL on a stainless steel surface. Then they were drop casted on top of the organic surface similar to a procedure outlined earlier.[142] Briefly, the organic substrates were vapor deposited on a stainless steel surface. Then 15 μL of 0.1% (w/v) of the NPs were drop casted on top of the organic surface. This method of deposition on an organic substrate surprisingly causes these particles to self organize as a single layer. The deposition of the NPs does not affect the glycine, this was verified by SEM.[142] The samples were analyzed using a custom-built SIMS instrument explained in Chapter II.

Results and Discussion

Bombardment of an agglomeration of Ag NPs results in a low signal from the NPs. The weak response is attributed to the low electron affinity of Ag (data not shown). However, when the Ag NPs are examined in a single layer on top of an organic substrate (e.g. glycine, guanine, histidine), Ag adducts, in particular $Ag(CN)_2^-$ are readily apparent in the mass spectrum. Figure 4.3 presents an excerpt of a negative ion mass spectrum of one such sample, where guanine was used as the substrate. The identity of these adducts have been verified by isotope studies, previously.[142]

Figure 4.4 presents a mass spectrum for bulk Au NPs. The high electron affinity of Au allows the experimental observation of the several peaks characteristic of Au NP and the skin (dodecanethiol). Au_n^- ($1<n<9$) cluster ions are evident in the mass spectrum.

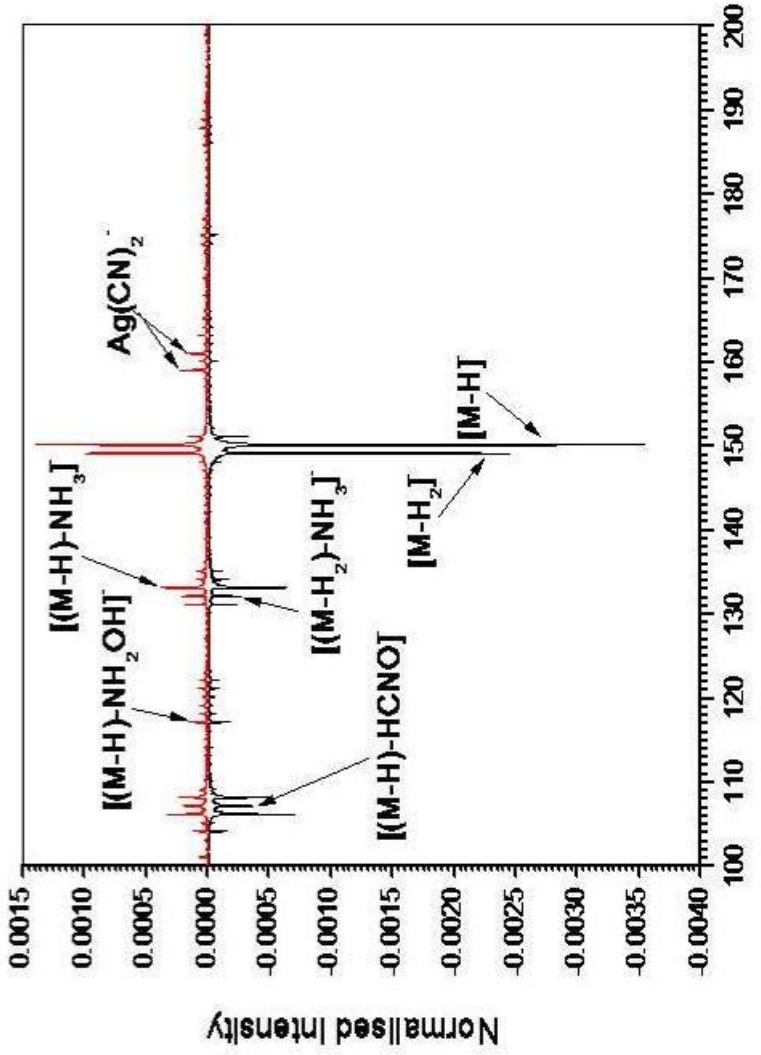

Figure 4.3. Negative ion mass spectrum of guanine before the deposition of Ag NPs (black) and after the deposition of Ag NPs (red). The y-axis for the bottom spectrum was shown in the negative scale for comparison. The bottom spectrum shows peaks characteristics of guanine and its fragments. After the deposition of Ag NPs, the guanine shows the presence of Ag adducts such as $Ag(CN)_2^-$. The peak intensities are normalized to the total number of projectiles on the y-axis. It should be noted that the height of the peak (normalized intensities) do not reflect the relative abundance of the isotopes of Ag, but the peak area does. The mass spectra were acquired with ~ 2 million projectile impacts.

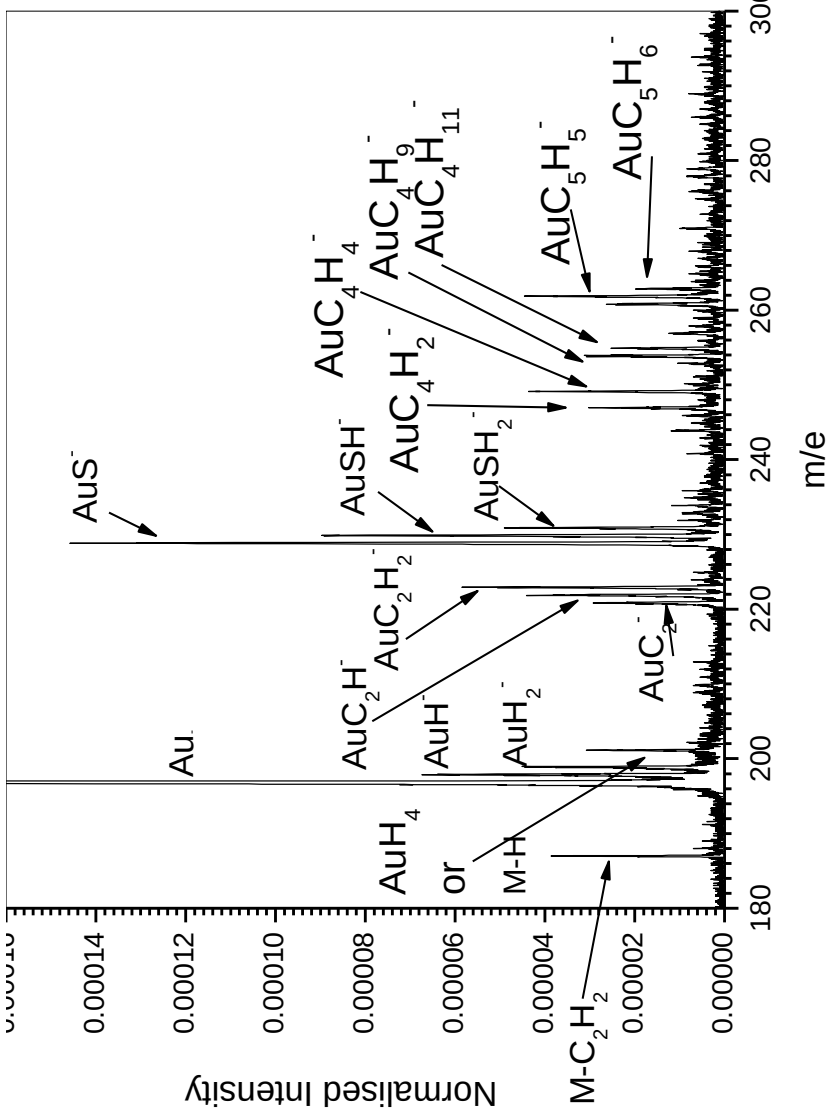

Figure 4.4. Negative ion mass spectrum of a bulk sample of Au NPs (5 nm) analysed by C_{60}^{+} accelerated to 26 kev.

The presence of these Au clusters is surprising. The abundance and number of these clusters are larger for these bulk NP when compared to a Si wafer nominally coated with a 200 nm Au layer. (Figure 4.5). Along with Au clusters the mass spectrum shows Au_nS clusters formed from the Au and coating of decanethiol. However, in the case of the nominally coated Au layer the Au_nS clusters are replaced with Au_nCl clusters. The source of the Cl is most likely from contamination during the manufacturing process.

The presence of Au_n and Au_nS clusters are also seen in the sample when the AuNPs are deposited as a monolayer on top of a guanine substrate (Figure 4.6). The Au clusters may be explained as follows. A "bulls-eye" hit by a C_{60}^+ on an Au NP will result in forward and lateral emission of Au fragments. The former implant into the substrate. The latter can undergo elastic collision(s) with surrounding Au NPs, likely resulting in further fragmentation (as they carry some internal energy) and may be emitted as a cluster carrying a negative charge. The products of the same process occurring on Ag NPs, i.e. $^{107}Ag^-$, $^{109}Ag^-$ (Figure 4.3) could not be detected given the low electron affinity of Ag.

Figure 4.3 and 4.6 also show respectively Ag and Au adducts. As noted at the outset, these adducts are the result of a multi-step process thought to involve "NP fragmentation cum substrate-molecule fragmentation-recombination". The nature and yield of adducts depend on the characteristics of the underlying organic substrate. The yields for the Ag and Au adducts with different substrates are given in Table 4.1.

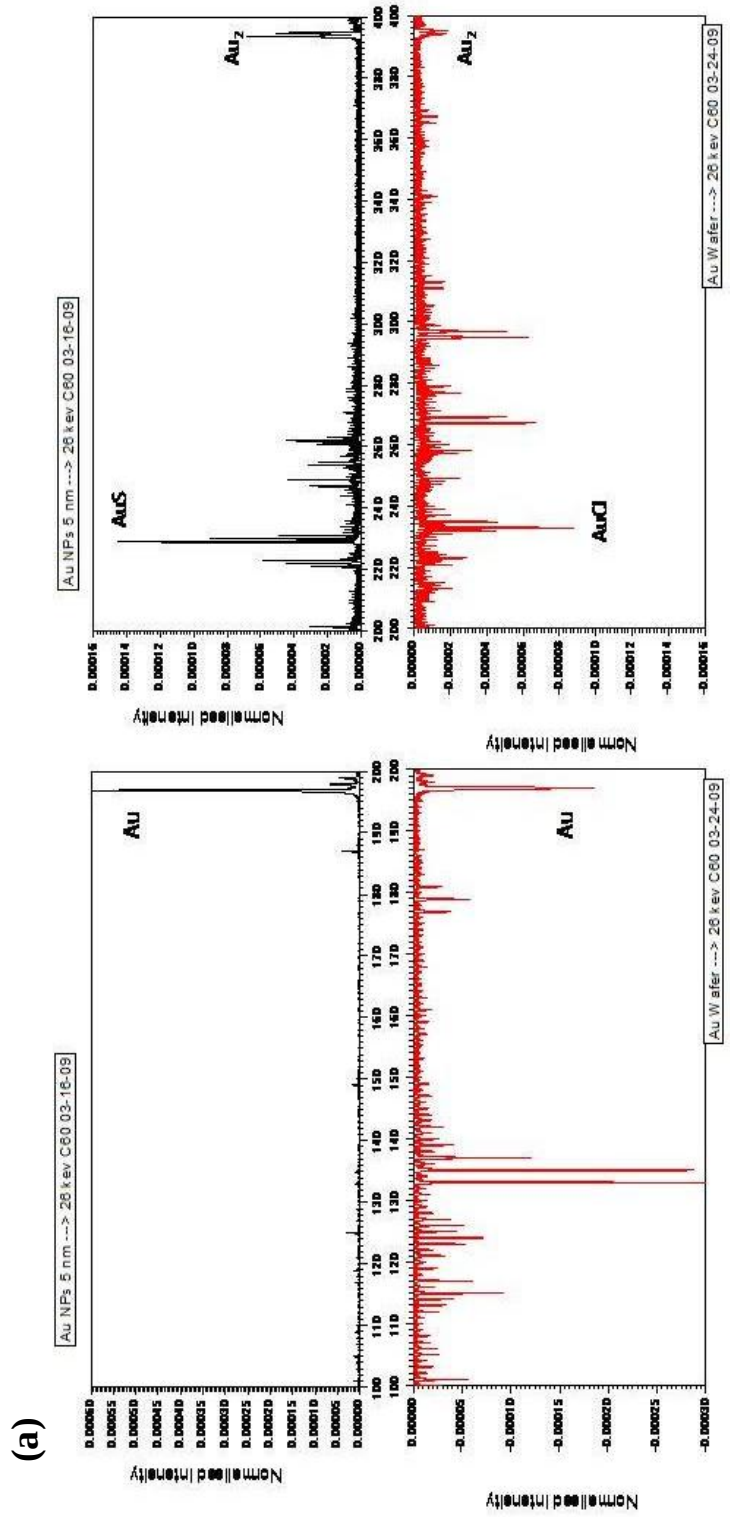

Figure 4.5. (a). Negative ion mass spectra of 5 nm Au NP bulk in black and Si wafer coated with a 200 nm Au layer in red, from mass range 100 to 400.

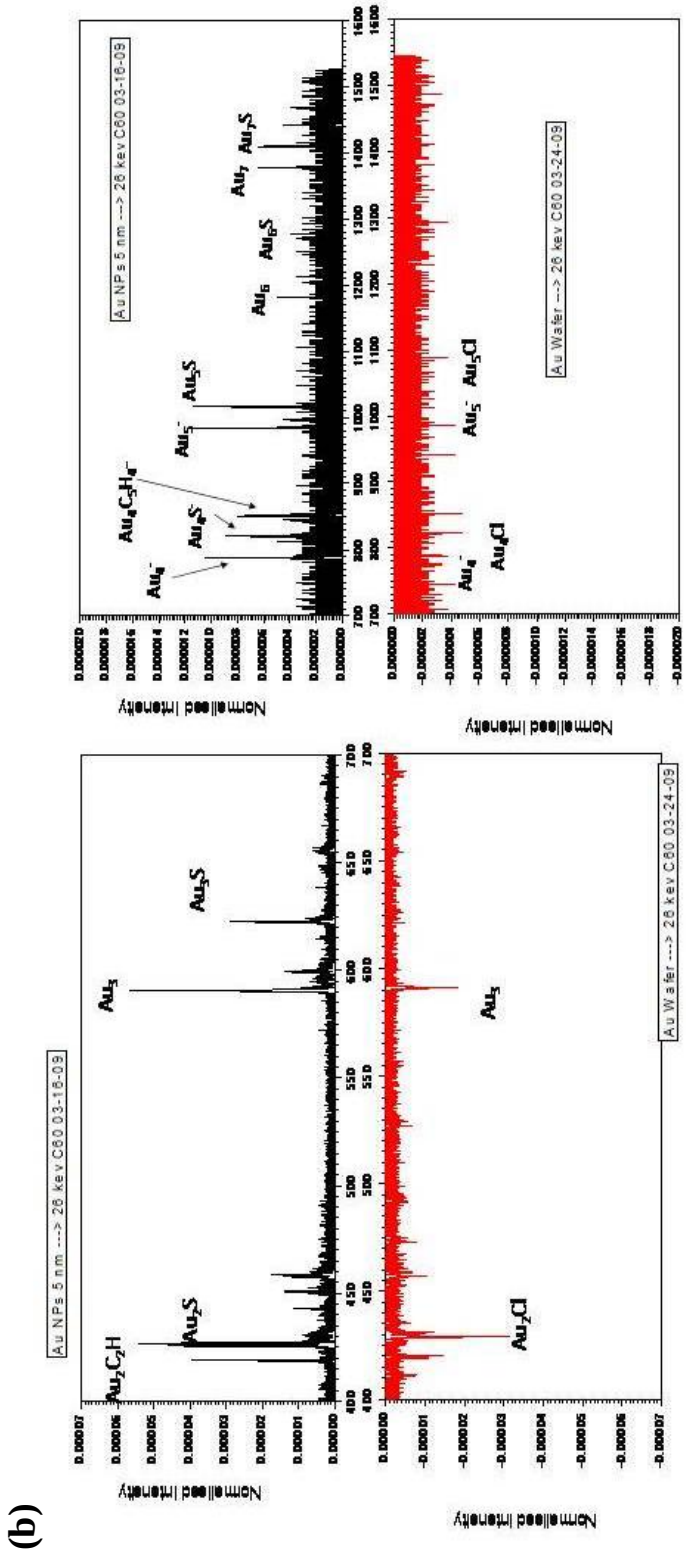

Figure 4.5. continued, (b). negative ion mass spectra of 5 nm Au NP bulk in black and Si wafer coated with a 200 nm Au layer in red, from mass range 400 to 1600. The mass spectra were obtained with ~ 2 million impacts of C_{60}^{+} accelerated to 26 keV. The peak intensities are normalized to the total number of projectiles on the y-axis.

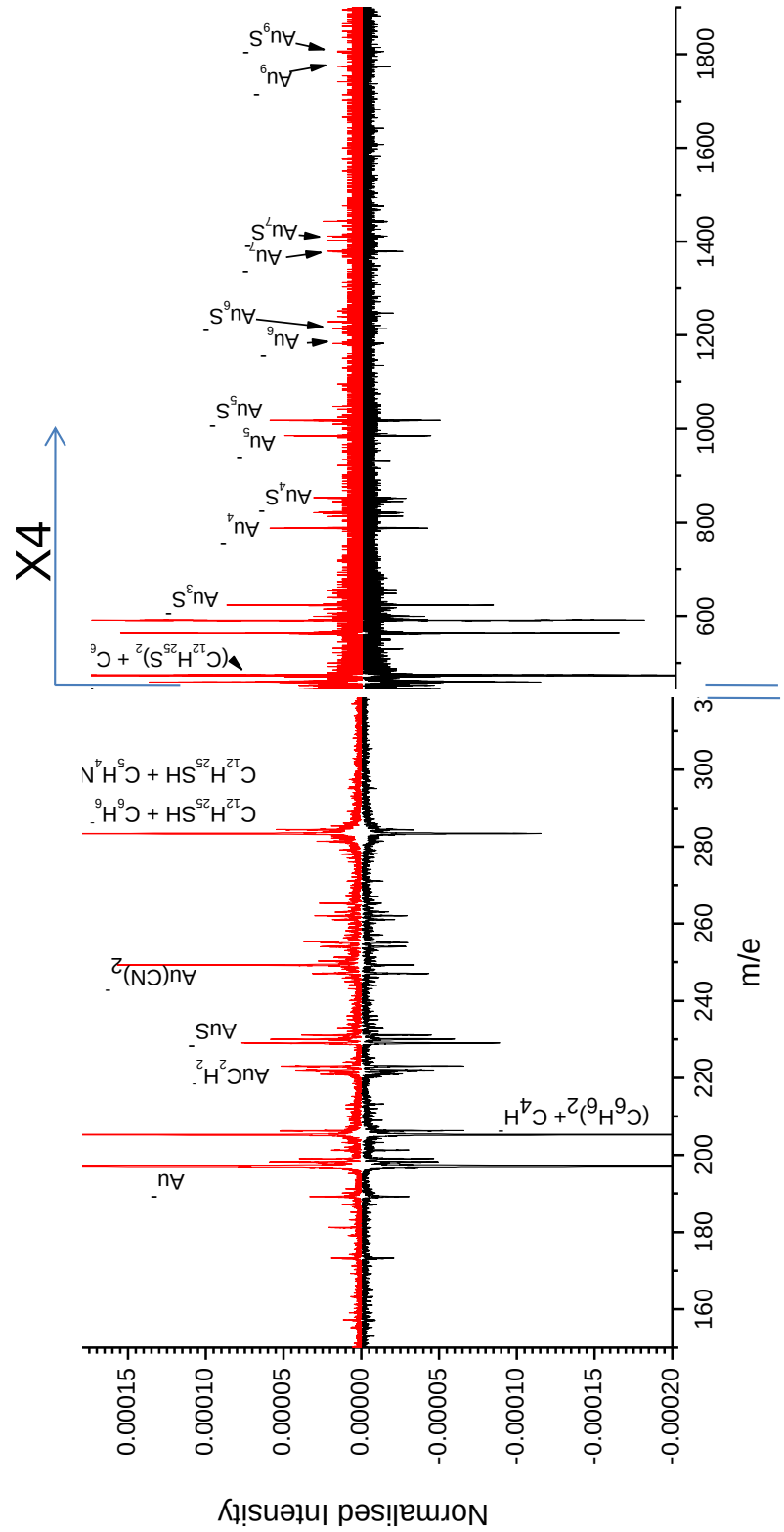

Figure 4.6. Negative ion mass spectrum of 5 nm Au NPs self organized as a single layer on guanine as the substrate (red) and on stainless steel plate (black). The mass spectra were acquired with ~ 2 million projectile impacts.

Table 4.1. Percentage yields of negative secondary ions from the different organic substrate samples after the deposition of the Ag NPs or Au NPs, for the respective samples. M-H represents the deprotonated molecule of the respective molecular ion.

Matrix	CN^- Y%	$[M-H]^-$ Y%	$[Ag(CN)_2]^-$ Y%	$[Au(CN)_2]^-$ Y%
Glycine	6.8	12.7	0.2	N/A
Histidine	4.6	0.5	0.4	N/A
Guanine	4.2	1.6	0.4	0.2

The Au adducts reported here are two orders of magnitude lower than those obtained when the Au_{400}^{4+} projectile impacts a glycine, histidine or guanine target directly.[134] The abundant adduct emission results from a simple process where "Au atoms ablate from the massive Au projectile and then recombine with fragments from the target molecule".[134] The data in Table 4.1 refers to a multi-step process where adducts result from the recombination of atoms due to the concurrently occurring fragmentation of a NP and of substrate molecules.

The methodology was extended to analyze a mixture of the two Au and Ag NPs (Figure 4.1c) Au having a high Z value is shown as bright spots whereas, Ag NPs of lower Z are seen as darker spots. An EDX spectrum was obtained to further verify the presence of both Au and Ag NPs (Figure 4.7). A portion of the TEM was imaged using the different level electrons from the respective consistent metals of the NP (Figure 4.7). However, as seen by the image, the technique is unable to resolve the individual NPs separately mainly because of the size of the NP. This represents an interesting case where a mixture of NPs of identical size and contain also approximately the same number of constituent atoms. The TEM presents a small portion of the grid. An examination of several areas of a single layer preparation of Au NPs and Ag NPs showed that they do not segregate in separate islands, but rather mix with each other as presented by the EDX images (Figure 4.7). A duplicate sample bombarded with a sequence of single C_{60}^{+} projectiles, produced the mass spectrum shown in Figure 4.8. The mass spectrum of the guanine surface prior to the deposition of the mixture of NPs is also presented for comp-

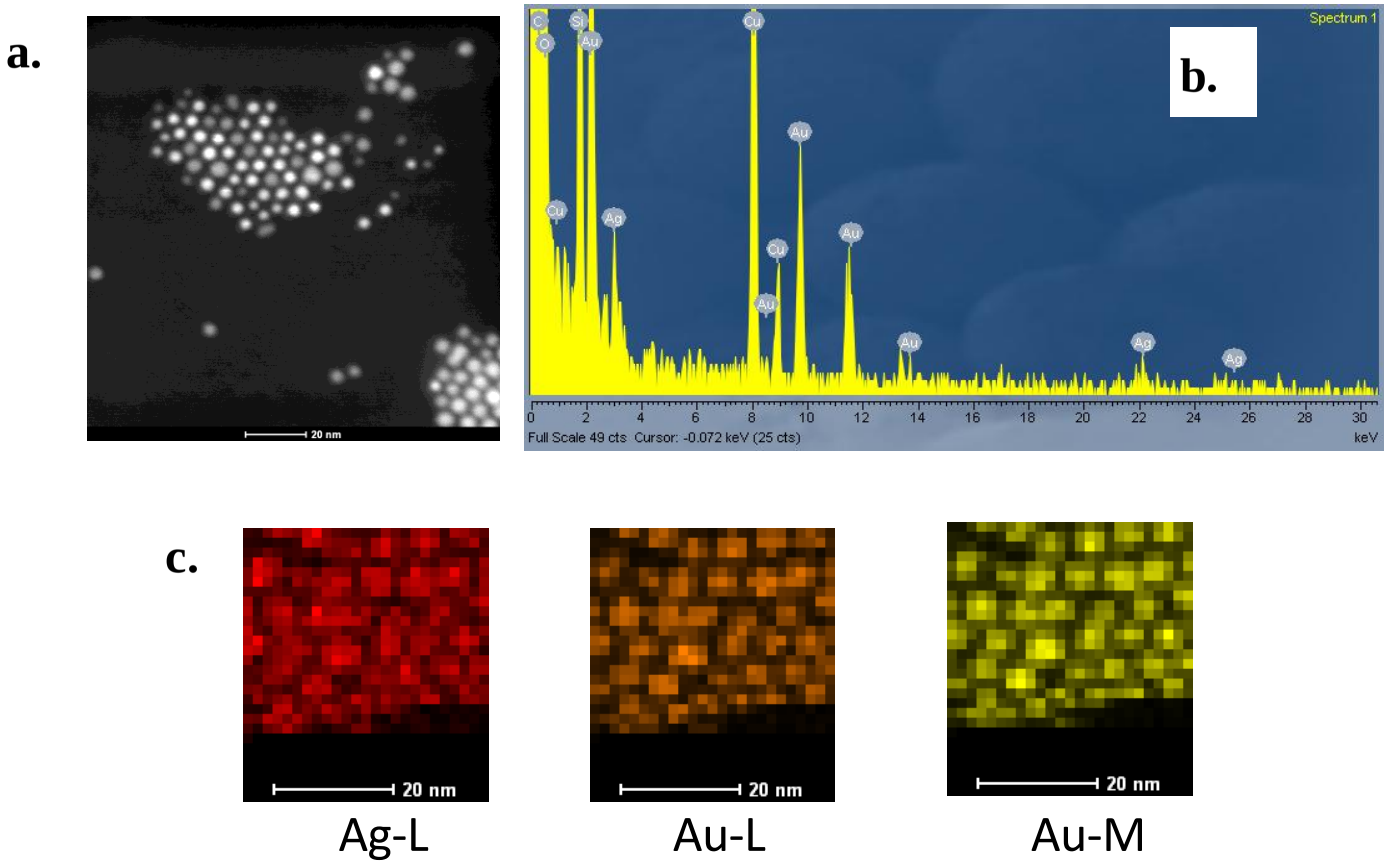

Figure 4.7. a). TEM image of Au and Ag NPs (50:50 mixture) deposited on top of a TEM grid that was vapor deposited with guanine. b). An EDX spectrum of the region shown in the TEM. The EDX shows both the presence of Au and Ag signal. c). EDX image of the area obtained by analyzing electrons from various energy levels.

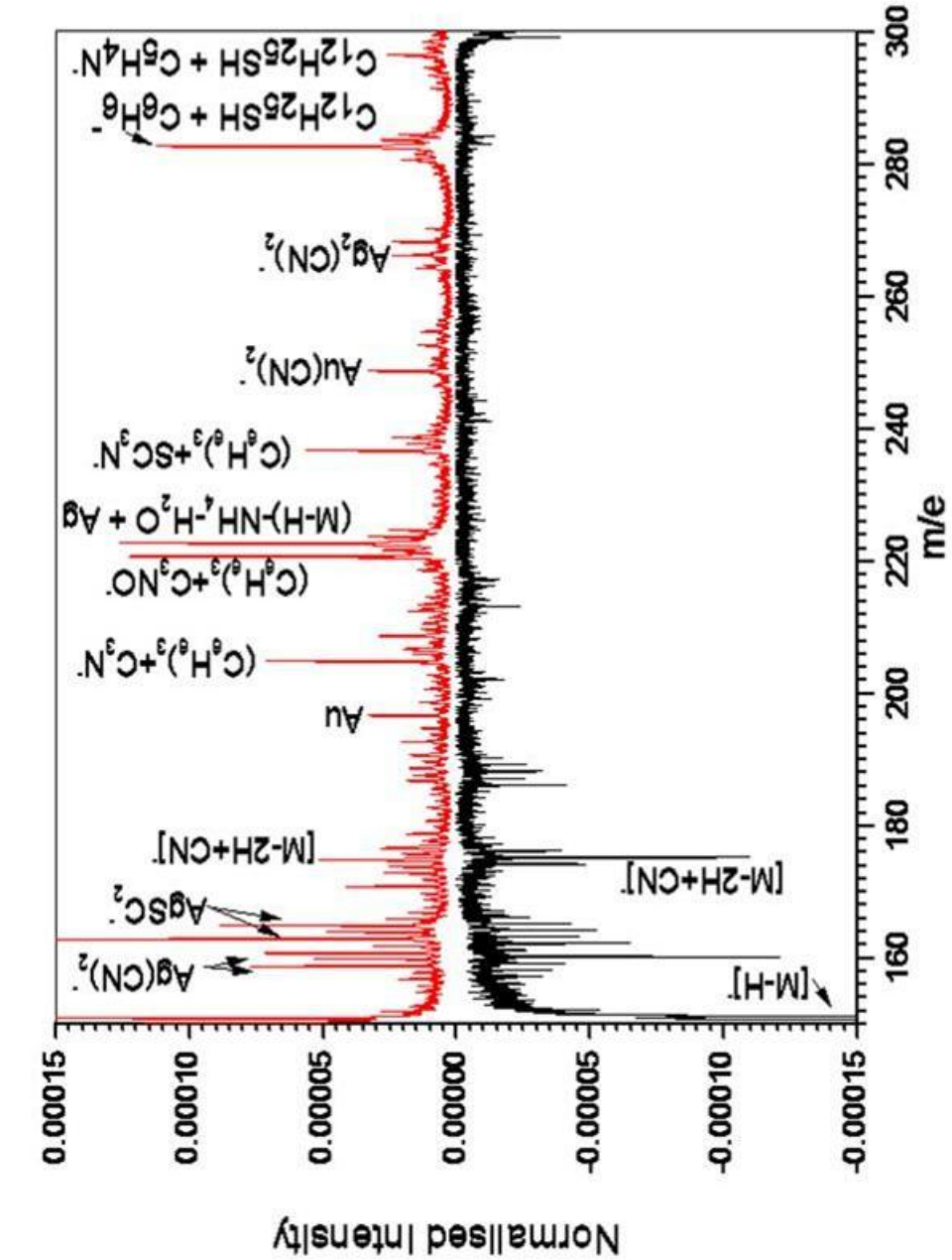

Figure 4.8. Negative ion mass spectrum of 5 nm Au NPs and Ag NPs (50:50 mixture) deposited as a self organized single layer on a guanine substrate (red). Guanine substrate itself without NPs is represented in black. The top spectrum was acquired with ~ 7 million projectile impacts and the bottom spectrum with ~2 million projectile impacts.

arison. The SIMS spectra show several Ag adducts: $Ag(CN)_2^-$, $Ag_2(CN)_2^-$.

The presence of Au NPs is only evidenced by the presence of Au and $Au(CN)_2^-$. The yields of adducts such $Au(CN)_2^-$ for the different sample is given in Table 4.2. The yield of the $Au(CN)_2^-$ and the $Ag(CN)_2^-$ are decreased in the mixture sample as compared to the pristine samples of the NP. The absence of Au_n^- cluster ions in the mass spectrum of the mixture of NPs confirms the explanation offered above, on why Au_n^- cluster ions are detected from a single layer of solely Au NPs on a guanine substrate. In the mixed layer, laterally ejected Au fragments from a bulls-eye hit on a Au NP, will either directly or after collision(s) with surrounding Au NPs, encounter a neighboring Ag NP and implant into the latter. This case is supported by the increase in yield of the deprotonated molecule of decanethiol as well as $AgSC_2^-$ in the mixture as compared to the pure Ag NP sample (Table 4.3 and 4.2 respectively). The increase in the yield of the SAM and the AgNP with the skin can be explained by the fact that Au atoms or clusters are better at sputtering secondary ions than Ag atoms. The absence of Au_n^- cluster ions in the mass spectrum is also an additional indication that Au and Ag NPs are in a homogenous mixture (Table 4.4). Laterally ejected Ag fragments from C_{60}^+ impacts on Ag NPs will collide elastically with surrounding Au or Ag NPs. They are, as noted already, unlikely to be negatively charged and hence remain undetected in our instrument.

Table 4.2. Percentage yields of adducts and the NP plus the coating for the different samples.

Percent yields Obtained with 26keV C_{60}^+				
Sample	$Au(CN)_2$	AuS, $AuSH, AuSH_2$	$Ag(CN)_2$	$AgSC_2$
Au NP Bulk	0.05	0.41	*	*
Au NP on Guanine	0.18	0.24	*	*
Ag NP Bulk	*	*	0.05	0.21
Ag NP on Guanine	0.01	*	0.35	0.09
Ag + Au NP on Guanine	0.04	*	0.13	0.30

Table 4.3. Percentage yields of the SAMs from the different samples.

Percent yields Obtained with 26keV C_{60}^+			DD - Dodecanethiol D - Decanethiol
Sample	[DD-H]	[DD-CH_3]	[D-H]
Au NP Bulk	0.04	0.04	*
Au NP on Guanine	0.03	0.04	*
Ag NP Bulk	*	*	0.03
Ag NP on Guanine	*	*	0.05
Ag + Au NP on Guanine	0.02	0.03	0.05

Table 4.4. Percentage yields of the Au clusters from the NP samples.

Percent yields Obtained with 26keV C_{60}^+				
Sample	Au	Au_2	Au_2H	Au_2S
Au NP Bulk	1.03	0.13	0.10	0.09
Au Wafer	0.43	0.05	0.03	*
Au NP on Guanine	0.71	0.1	0.09	0.05
Ag + Au NP on Guanine	0.04	*	*	*

Conclusion

C_{60}^{+} impacts on a single layer of a mixture of individually isolated Ag and Au NPs on an organic substrate causes a fascinating array of processes depending on the type of impact. Bulls-eye hits can result in "fragmentation-elastic-collision-cluster emission". The condition for this sequence of steps is that the NPs surrounding the fragmenting one be of equal or higher Z. Further, observation in practice requires that the fragmenting NP be of an element with high electron affinity. The purely physical sequence competes with a physico-chemical multi-step process resulting in the emission of adducts. A judicious choice of the organic substrate enhances the detection sensitivity for the metallic NP via the adduct formation. Grazing impacts cause emission of self assembled monolayer fragments, including fragments with attached metal atoms. Finally impacts in areas not covered by NPs show emission of substrate-specific ions. Clearly the characterization of complex nanometric structures via SIMS requires examination of signals from individual impacts. To generate detectable signal the individual projectile must be massive and energetic, the high energy density imparted in the collision volume is dissipated via multiple physical and chemical processes. They need to be understood for the accurate interpretation of the mass spectrometric data.

CHAPTER V

IMAGING MASS SPECTROMETRY WITH LASER DESORPTION/IONIZATION MEDIATED BY SOFT-LANDED NANOPARTICLES*

Introduction

Metal NPs have been used extensively in mass spectrometry to analyze biologically relevant molecules since 1988.[47-50] There exists a challenge to develop a preparation method which incorporates the NPs such that one observes uniform signal response from all regions of the surface. Conventional methods incorporate the NPs into the sample by mixing the NP's with the analytes.[51-53] To be viable for mass spectrometric imaging, NP incorporation must be achieved without disrupting the spatial arrangement of analyte molecules on the surface. Previously, Woods et al. have demonstrated an alternative technique for the incorporation of Au NPs into bioorganic solid material which is conducive to imaging applications.[143,144] Briefly, an Au LMIS is used to implant Au_{400} clusters (~2nm) into the top layers of biological samples. However, there are only a few such Au LMIS sources and they require the sample be introduced to high vacuum.

Here we demonstrate the use of an alternative delivery method for depositing a layer of Au NP onto the biological surface. The particle delivery system (PDS) utilized enables complete deposition at ambient or near-ambient conditions in less than five minutes. This PDS is typically used as a gene delivery technique in which heavy metal NPs coated with plasmid DNA are injected into multiple cells simultaneously. It was

*Parts of this chapter are reprinted with permission from *JASMS,* S. Rajagopalachary, J.D. DeBord, S.D.Sherrod, Z. Zhou, S. V. Verkhoturov, D.H.Russell and E. A. Schweikert, Imaging Mass Spectrometry with Laser Desorption/Ionization Mediated by Soft-Landed Nanoparticles. To be *Submitted*. Copyright [2009] Elsevier.

initially developed to introduce foreign nucleic acids into plant cells.[145,146] The PDS uses a pneumatic pressure differential to accelerate the NPs to supersonic velocities. Impact velocity is tunable but is typically on the order of 700 m/s.[147] The NPs used in this study reach the surface with less than 2 eV/atom kinetic energy. At this impact energy, the particles remain intact and do not penetrate the surface.[148] All NPs are transferred to the sample in one "shot". Additional information about the particle delivery system can be found elsewhere.[149]

In these initial experiments, Au NPs (5nm) were deposited using the PDS on prepared surfaces composed of the peptide fragments dynorphin 1-8 and substance P and the amino acid glycine along with isotopically labeled ^{15}N-glycine. The results show approximately an order of magnitude increase in signal when compared to the untreated sample. These results are concurrent with previously obtained results.[143,144]

Experimental Section

Sample Preparation and Au NP Deposition

Dynorphin 1-8 (YGGFLRRI, MW 981.2), substance P (RPKPQQFFGLM-NH_2, MW 1347.64), glycine, ^{15}N-glycine were purchased from Sigma Aldrich. The Au NPs (5nm) functionalized with dodecanethiol in toluene were purchased from Nanoprobes Inc. The integrity and size distribution were verified by TEM (Figure 5.1). For the drop-casted samples, the analytes were dissolved in deionized water at a concentration of 1nmol/µL . Two µL of each these solutions were deposited at three different spots on a stainless steel plate and dried in air. This plate was then introduced into a PDS-1000/He

Biolistic® Particle Delivery System for Au NP deposition. (Figure 5.2) A control plate was spotted in an identical manner but was not treated. For the imaging samples, the peptides were dissolved in methanol at a concentration of 5nmol/μL and electrosprayed one at a time, perpendicular to each other on the stainless steel plate using a mask. For the vapor deposited samples, glycine and ^{15}N-glycine were vapor deposited one at a time using a mask in the same way so that a cross was formed. These stainless steel plates were then treated with Au NPs. Control plates for each of the imaging samples were developed using the same procedure but were not treated. For all LDI samples, 100 μL of the 5 ppm Au NPs in toluene were deposited on a macrocarrier disk and dried leaving approximately 200 μg of NPs. NPs were deposited under 27 in Hg vacuum. The sample for STM analysis consisted of glycine vapor deposited onto highly oriented pyrolytic graphite (HOPG). Fifty μg of the Au NPs were then deposited on the surface. The sample was visualized by STM before (image not shown) and after (figure 4a) the deposition of Au NPs.

Laser Desorption/Ionization MS Analysis

LDI MS analysis of the treated and the untreated samples was performed using a Voyager DE-STR (Applied Biosystems, Foster City, CA) with a 337 nm N_2 laser and a

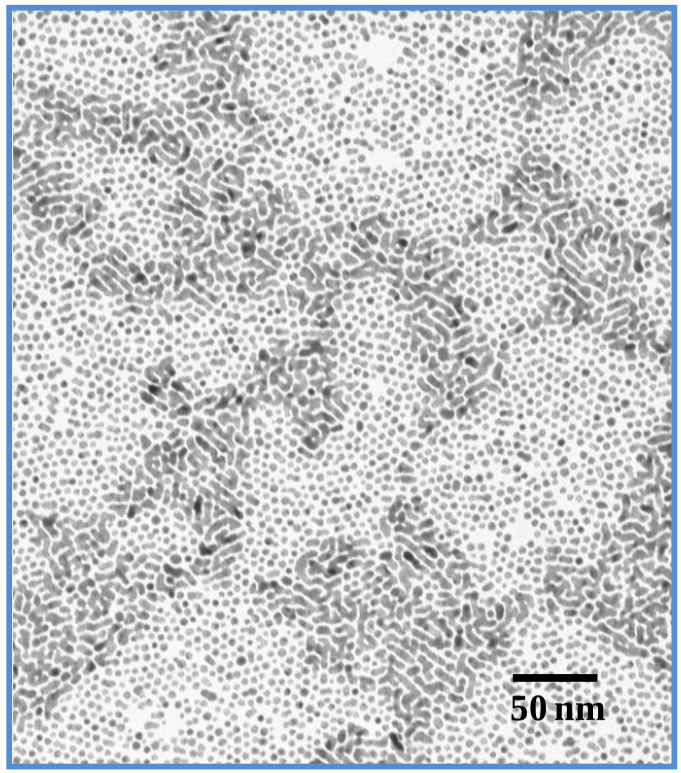

Figure 5.1. TEM image of the dodecanethiol functionalized Au NPs (~5 nm) in toluene deposited on a TEM grid. Scale bar represents 50 nm.

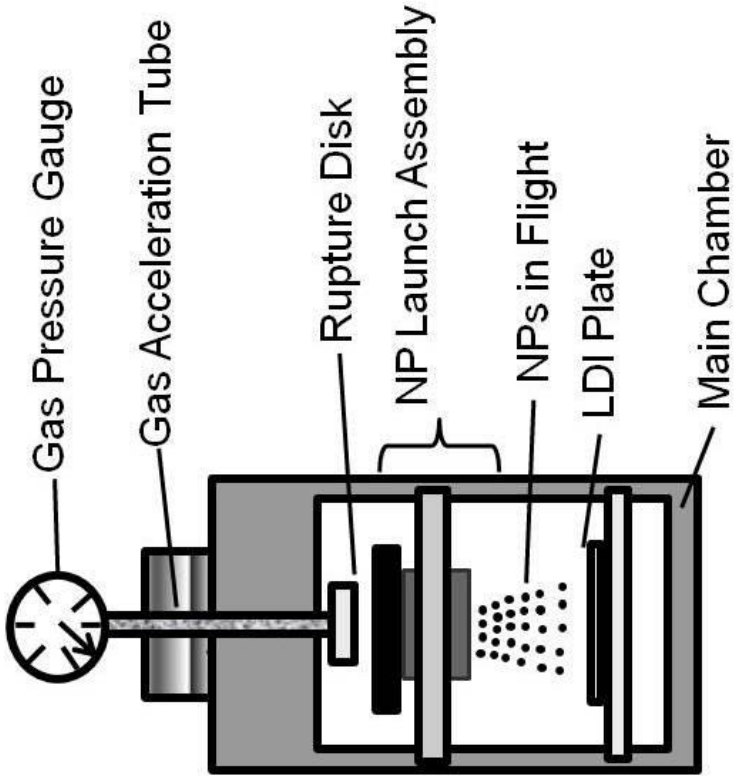

Figure 5.2. Schematic representation of the particle delivery system (PDS) used to soft land Au NPs.

20 kV acceleration voltage. The laser fluence (according to the attenuator gradient) was varied from 1500 to 2700. Positive ion mass spectra were obtained from 3 different sums of shots (6, 12, 50) on the treated sample and 2 shots (12,50) on the untreated sample as 6 shots did not yield any signal.

The samples were analyzed using both reflected and linear mode. Imaging MS analyses were performed using the same Voyager DE-STR instrument under optimized conditions. Imaging samples were translated in 70 μm increments due to the observation that the laser spot size was projected onto the sample surface as an ellipse, *ca.* 70 x 160 μm. Individual mass spectra represent the average of 50 laser shots.

STM Analysis

The scanning tunneling microscopy (STM) experiments were conducted at room temperature, using an Omicron STM1 in a vacuum chamber with a base pressure lower than 2.0 x 10^{-10} Torr. All images were scanned in constant-current mode with an electrochemically etched tungsten tip. All bias voltages are reported with reference to the sample. The highly oriented pyrolytic graphite or HOPG (ZYB quality, 1cm x 1cm x 1mm, MicroMasch®) was prepared by the scotch tape peeling method.

ToF SIMS Analysis

The samples were analyzed using a custom-built SIMS instrument equipped with an effusive C_{60} source. The details of the instrument are described in Chapter II. C_{60}^{+} was

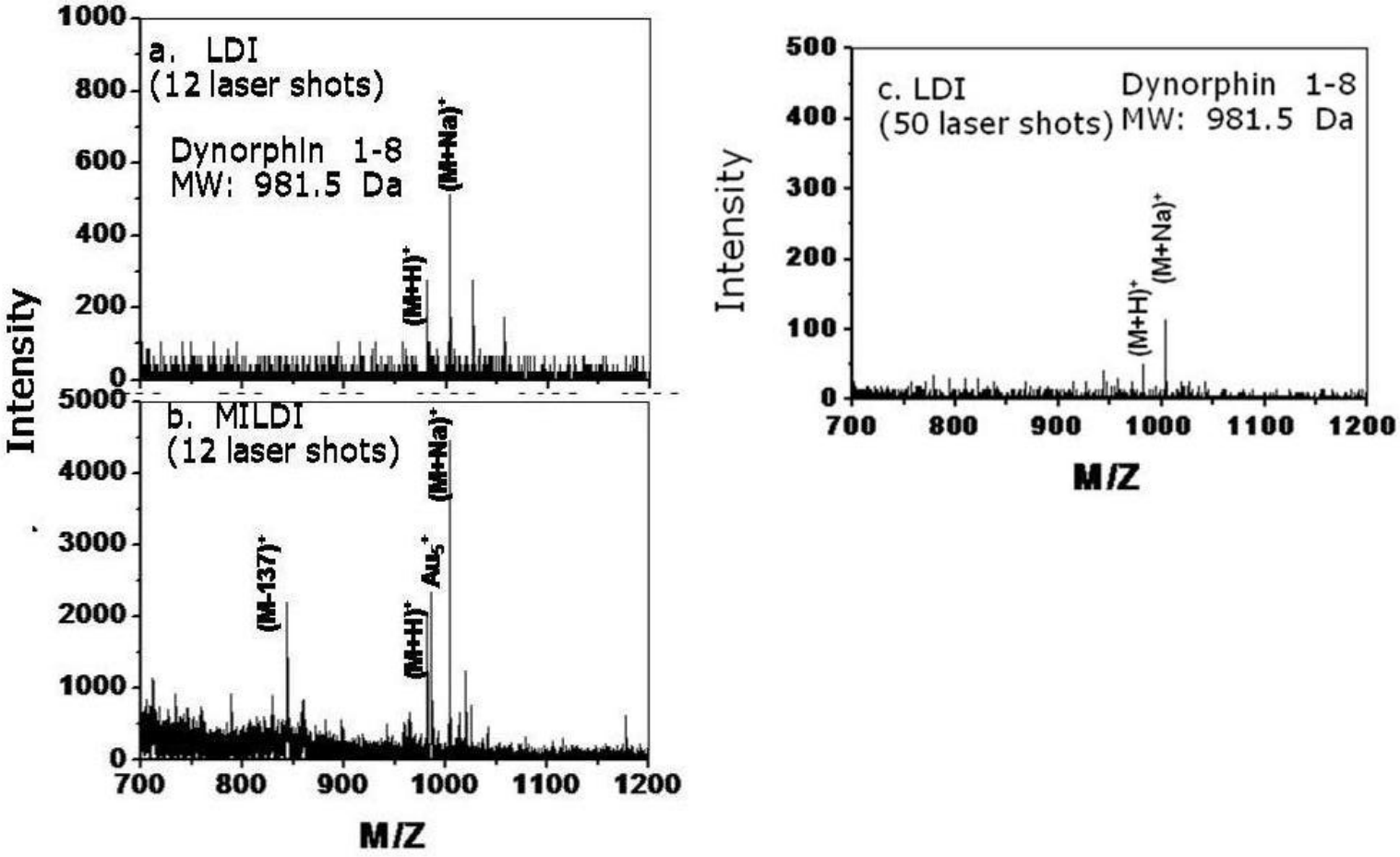

Figure 5.3. (a) Positive ion LDI-ToF mass spectrum for dynorphin 1-8 sample for an untreated control obtained with 12 laser shots. (b) LDI-ToF mass spectrum from a dynorphin 1-8 sample treated with 5 nm Au NPs obtained with 12 laser shots. Both mass spectra were obtained with the same laser fluence (2590, according to the attenuator graduation) (c). Positive ion LDI-ToF mass spectrum for dynorphin 1-8 sample for an untreated control obtained with 50 laser shots.

accelerated to 26 keV total impact energy. In all cases approximately two million events were recorded over a 3 mm^2 area with a diameter of ~2mm. Hence, the bombardments occurred in the "super-static" regime where repeated impacts on the same site are practically impossible.

Results and Discussion

Figure 5.3a. presents a positive ion mass spectrum of an untreated dynorphin 1-8 sample obtained with 12 laser shots. After 50 laser shots the intensity of the $[M+H]^+$ ion signal goes down compared to 12 laser shots (Figure 5.3 c). The laser fluence was 2590 according to the laser attenuator gradient. At this laser fluence the positive ion LDI spectrum from the untreated control sample (a) shows weak $[M+H]^+$ ion signal. There is an enhancement of the protonated molecule and the $[M+Na]^+$ ion in the sample treated with Au NPs (b). Figure 5.4 displays peaks observed in the mass spectrum corresponding to Au clusters (e.g., Au_3^+, Au_5^+) . This result is concurrent with previously observed results where 5 nm Au NPs were mixed with the analyte.[51]

We obtained similar results from the analysis of substance P (Figure 5.5). All mass spectra were obtained with a laser fluence of 2390; however, the untreated control sample shows higher relative abundance of both $[M+Na]^+$ and $[M+K]^+$ ions than the $[M+H]^+$ ion obtained with 50 laser shots. This trend is also observed for the Au NP treated sample as there is an enhancement of the $[M+Na]^+$ and the $[M+K]^+$ signal obtained from 2 laser shots. The enhancement is more apparent when the samples are compared at 12 laser shots. (Figure 5.5.a,b)

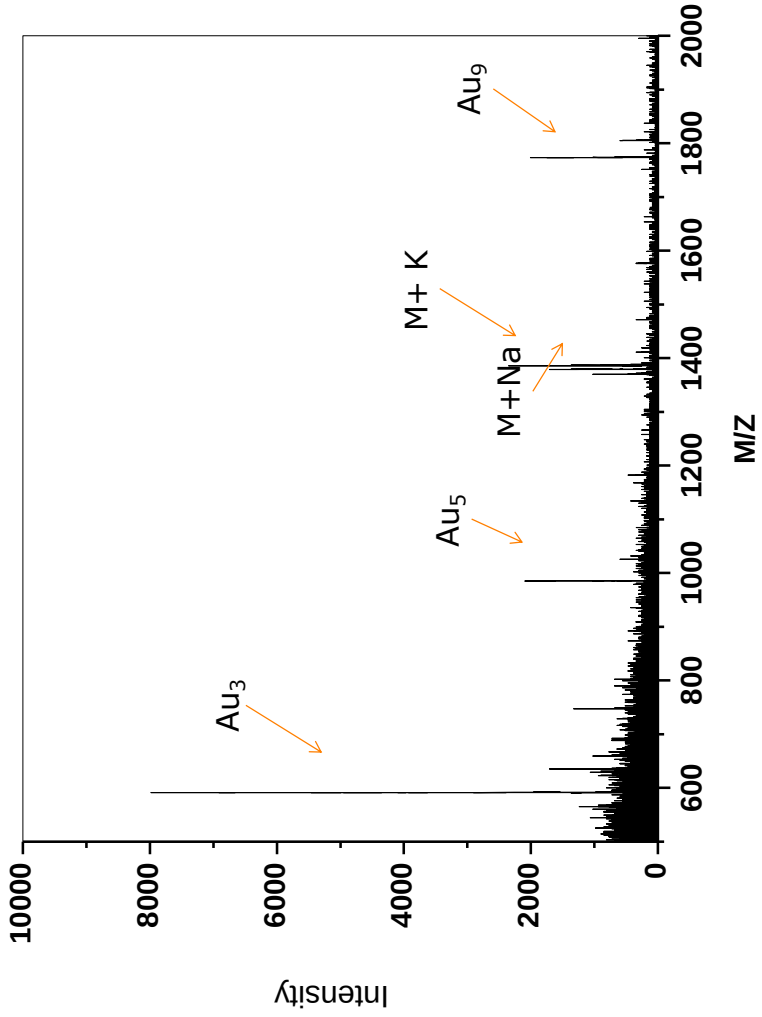

Figure 5.4. Positive ion LDI-ToF mass spectrum for Substance P showing the presence of several Au clusters.

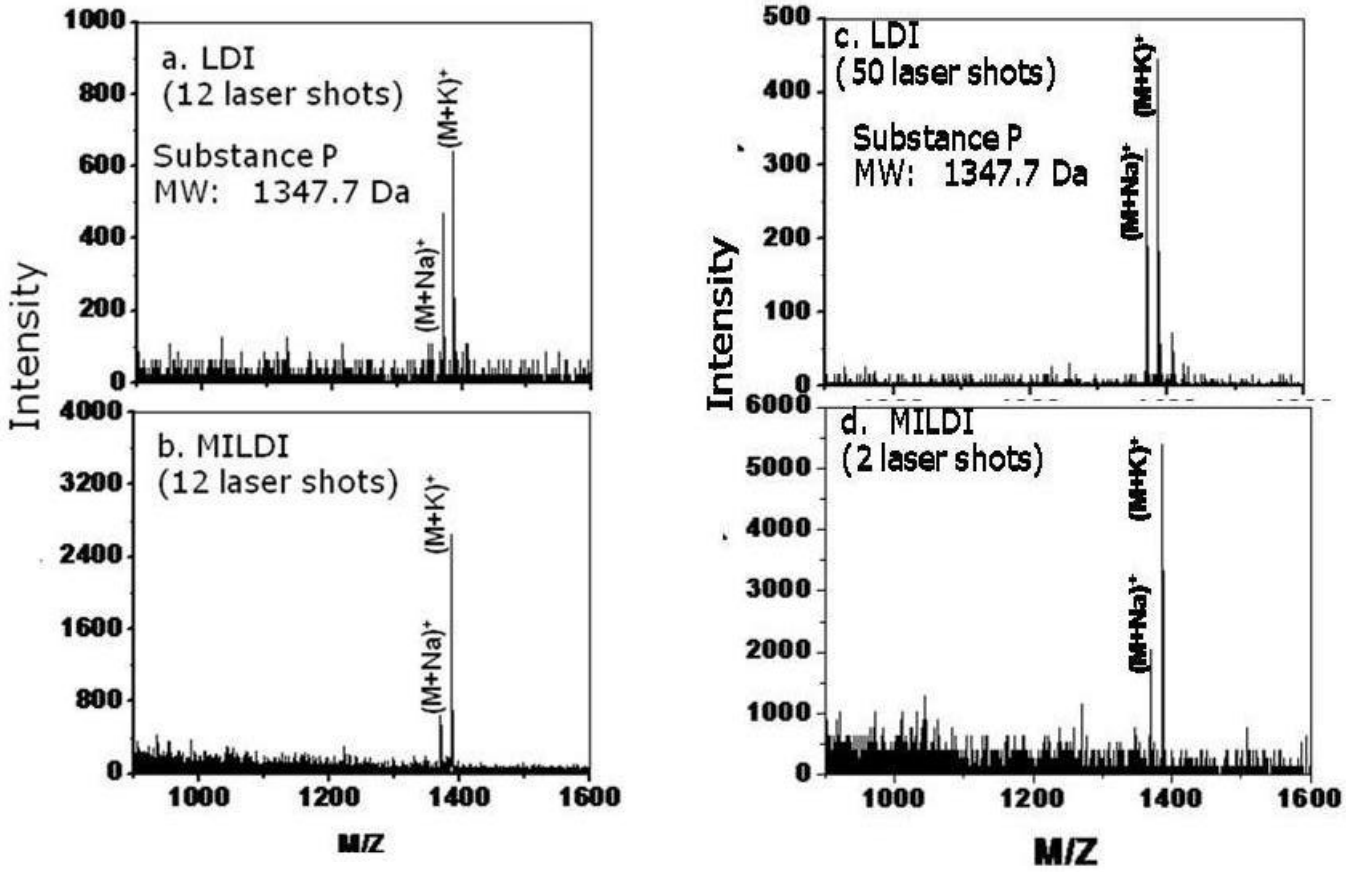

Figure 5.5. (a) Positive ion LDI-ToF mass spectrum of untreated substance P obtained from 12 laser shots. (b) LDI-ToF positive ion mass spectrum obtained from a sample treated with 5 nm Au NPs obtained from 12 laser shots. (c) Positive ion LDI-ToF mass spectrum of untreated substance P obtained from 50 laser shots. (d) LDI-ToF positive ion mass spectrum obtained from a sample treated with 5 nm Au NPs obtained from 2 laser shots. All mass spectra were obtained with the same laser fluence (2390, according to the attenuator graduation).

The STM and SIMS analyses were undertaken in order to determine the nature of the surface following deposition of the Au NPs. The STM image in Figure 5.6a shows that the Au NPs are capable of forming a SAM. This result is typical for much of the region where deposition occurred. The appearance of a SAM was unexpected due to the visually inhomogeneous deposition. The PDS deposits the NPs in such a way that the particle concentration is higher at the center and decreases as the distance from the center increases. The effective concentration range for this study was obtained when the center of the shot was focused away from the area of interest and the peripheral spray of particles covered the sample (Figure 5.6). Mass spectra obtained at the center of the shot only contained peaks corresponding to the Au NPs because the deposited layer of Au NPs was too thick. For this reason we believe the signal enhancement to be greatest in regions where a SAM of NPs is created or at a level just below this concentration. Static SIMS analysis was performed to verify the deposited Au NPs were in close proximity to the surface. Substance P was bombarded with individual C_{60}^{+} projectiles accelerated to 26 keV before (Figure 5.7b red) and after (Figure 5.6b black) soft-landing Au NPs. The sample shows the presence of strong Au and Au adducts, such as $Au(CN)_2^{-}$, after the Au NP treatment (Figure 5.7b black), whereas they were absent before the Au NPs were soft-landed (Figure 5.7b red). We have reported previously, for such adduct peaks to occur it requires the "NP atomization cum substrate-molecule fragmentation-recombination".[142] As the projectile probes a depth of less than 10 nm, this implies that the Au NPs were deposited/implanted at such depths.[100,143] The rapid decline in signal

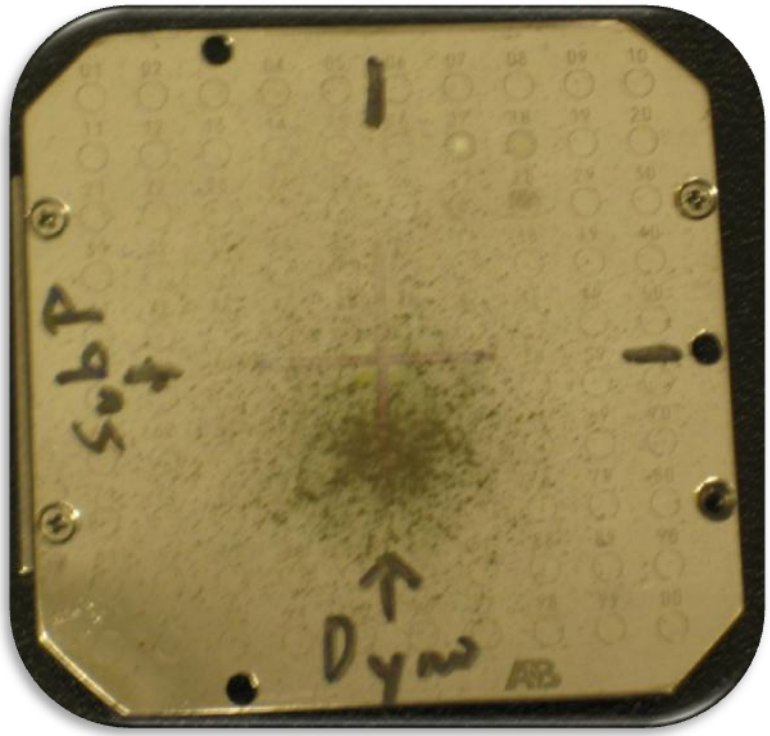

Figure 5.6. Picture of the stainless steel plate with electrosprayed Substance P and Dynorpin 1-8 fragment indicating the spread of Au NPs by the PDS.

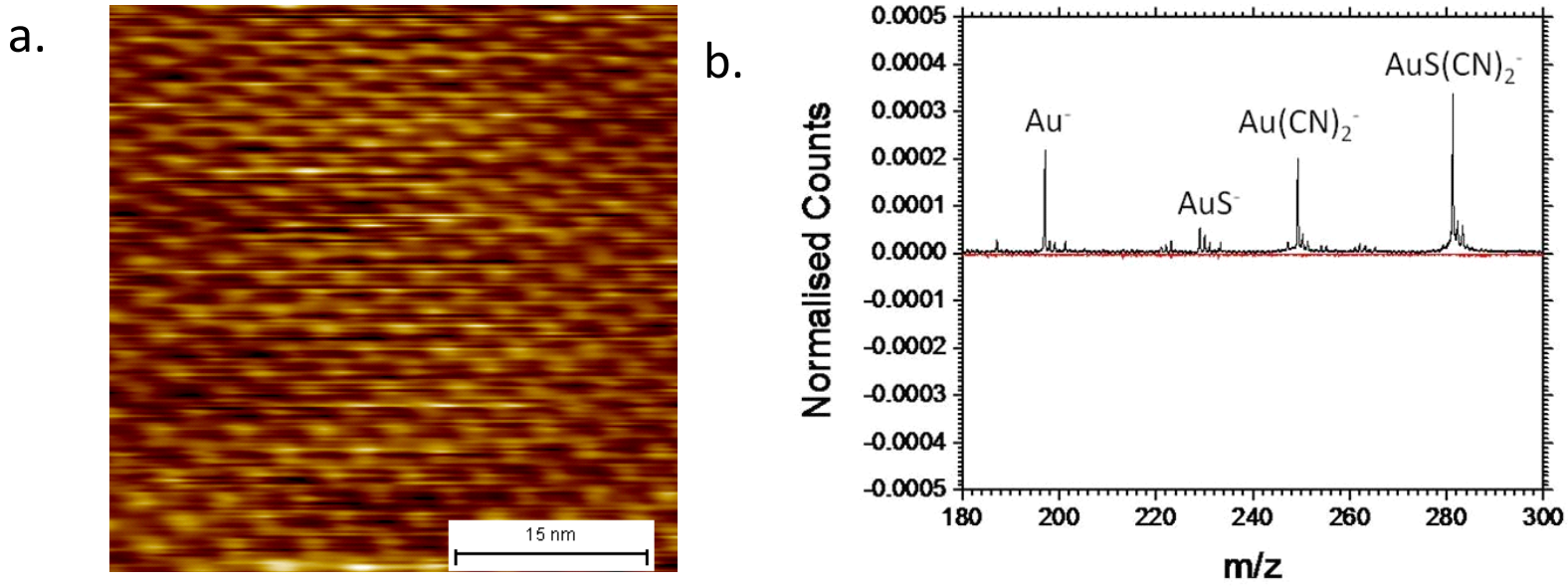

Figure 5.7. (a) STM image of 5 nm Au NPs self-assembled on glycine (35 nm x 35 nm, 1.0 V, 0.1 nA). (b) A selected mass range of a negative ion ToF-SIMS mass spectrum of Au NPs deposited on substance P on top (black) and substance P without deposition on the negative half (red) of the y-axis. Au and Au adduct peaks were observed when Au NPs were soft-landed on the sample, the control (without Au NPs) showed absence of these peaks. The spectra were obtained under C_{60}^{+} bombardment at 26 keV total impact energy. Negative values were a means to compare both the spectra on the same mass scale. The peak intensities are normalized to the total number of projectiles on the y-axis.

with increased laser shots also suggests that the NPs were located near the surface. Near the surface, they are quickly ablated away by the beam and once removed, ionization is severely reduced. This phenomenon was also observed by Woods et al.[143]

We further tested the efficiency of the particle delivery system deposition process for imaging applications. In this case dynorpin1-8 and substance P were electrosprayed normal to each other. Figure 5.8a. represents two MS ion images obtained from this sample. Green represents the emission of [substance P + Na]$^+$ at m/z 1369.7 which was sprayed horizontally and blue represents the emission of [dynorphin 1-8 + H]$^+$ at m/z 981.5 which was sprayed vertically. The MS ion image at m/z 590.9 shows there is emission of Au_3^+ over the entire imaged area. Representative mass spectra for each analyte is shown in Figure 5.8b. The mass spectra were obtained with a laser fluence of 2290. The control electrosprayed sample did not yield any signal of significance to image at that laser fluence (data not shown).

The capability of the method to image small molecules was shown using a sample of glycine and ^{15}N-glycine (Figure 5.9). Glycine was vapor deposited horizontally and the MS ion image for the protonated molecule, [glycine + H]$^+$ (m/z 76.0), is shown in green. Similarly, ^{15}N-glycine was vapor deposited vertically and the MS ion image for [^{15}N-glycine + H]$^+$ (m/z 77.0) is shown in blue. The ^{15}N-glycine was vapor deposited after glycine, therefore ^{15}N-glycine is the observed species at the region of overlap. It is worth mentioning that we observed a more uniform response from the vapor deposited samples than the electrosprayed samples due to the quality of sample

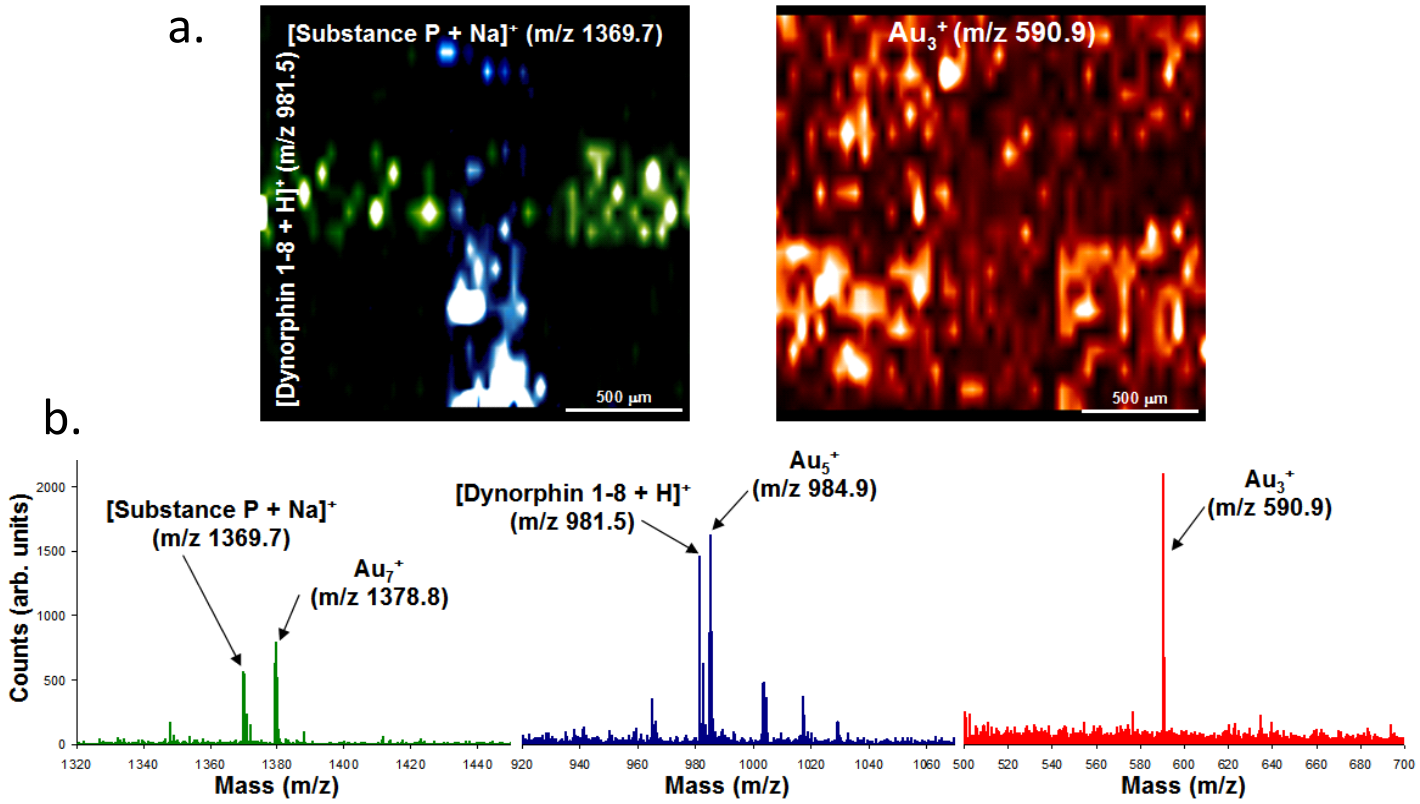

Figure 5.8. (a) MS specific ion images for $[Substance\ P + Na]^+$, $[Dynorphin\ 1\text{-}8 + H]^+$ and Au_3^+ following gold implantation of an electrosprayed sample (substance P – horizontal, dynorphin – vertical). (b) MALDI-ToF mass spectra obtained during analysis in specific regions of the sample. Both substance P (m/z 1369.7) and dynorphin (m/z 981.5) is observed in different regions of imaged sample, however Au_3^+ is observed throughout the entire imaged area.

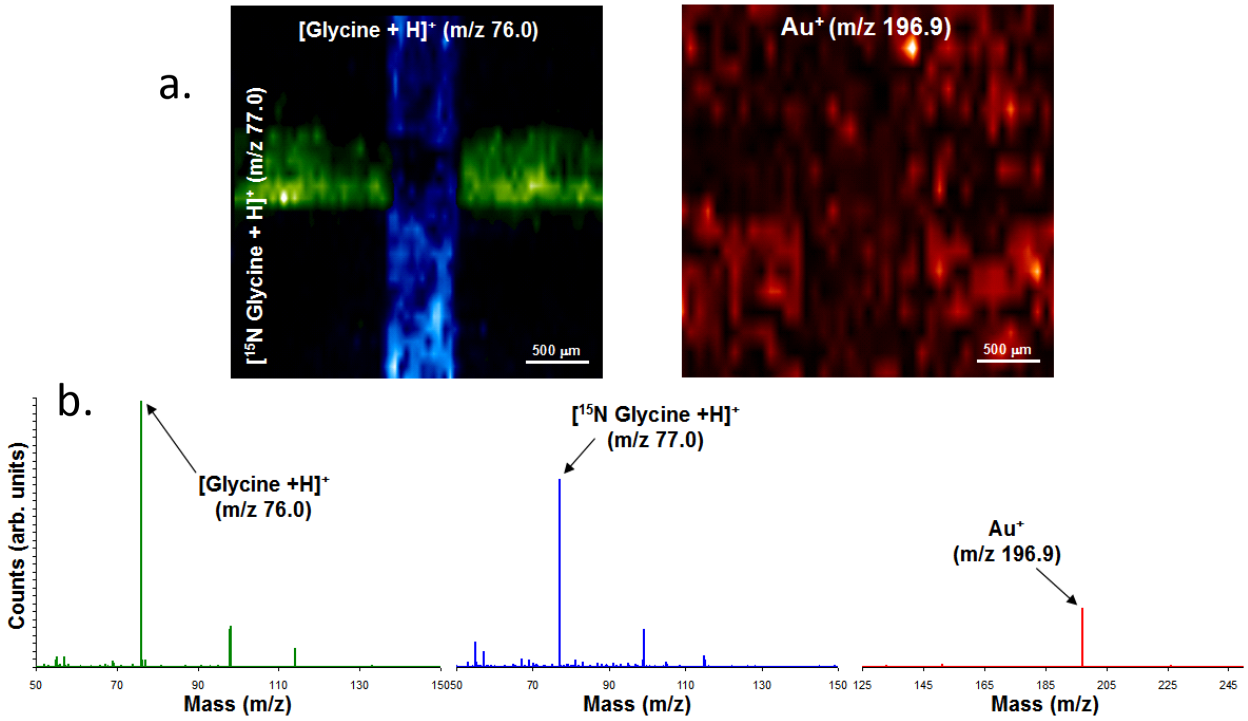

Figure 5.9. (a) MS ion images for $[Glycine + H]^+$, $[^{15}N\text{-}Glycine + H]^+$ and Au^+ following Au NP deposition on a vapor deposited sample (glycine – horizontal, ^{15}N-glycine – vertical). (b) LDI-ToF mass spectra obtained during analysis in specific regions of the sample. Both glycine (m/z 76.0) and ^{15}N-glycine (m/z 77.0) are observed in different regions of the imaged sample, however Au^+ is observed throughout the entire imaged area.

preparation. Vapor deposition resulted in a more uniform application of analyte than the electrospray procedure used.

The enhancement of desorption likely arises from a thermally driven mechanism, where there is an absorption of the photon energy by the Au NPs stimulating the heating of the surrounding analyte volume. Ions are likely to originate from analyte molecules adsorbed on or around the particle surface.[50] Au NPs have been reported to absorb photon energy at 337 nm, as used in our study.[150, 151] On the other hand, the absorption at the heated particle surface can produce the possible overheating which would result in the disintegration of the analyte. Perhaps, the self assembled monolayer of dodecanethiol on Au NPs reduces the direct thermal load on the analyte by acting as a buffer for the analyte molecules upon desorption.[50] The effect of the different lengths of this buffer region on the enhancement of the signal as well as the fragmentation of the analyte molecule remains to be a topic of further investigation.

Conclusion

Deposition of Au NPs via the particle delivery system represents an alternative method of sample preparation for enhancing ion emission using NPs while completely avoiding any solvent effects. Solvent-free deposition of NPs avoids analyte delocalization and thereby opens several exciting avenues for label-free biological imaging of tissues with microprobes. This technique is currently being applied to tissue imaging in our lab. The small particle size (5 nm) allows one to avoid the organic matrix crystals of MALDI which can limit the obtainable resolution.[53] For this NP matrix, the

resolution is theoretically limited to the laser spot size. The NPs can also be tailored for specific MS applications[152] to elicit analyte specificity[153] without altering the sample or making the NPs toxic for in vivo studies. This technique should find application in the imaging of biomolecules in tissues.

CHAPTER VI

CONCLUSIONS

In this study we address the issue of chemically characterizing individual NPs including their surfaces and the chemical environment surrounding them. Cluster SIMS in the event-by-event bombardment/detection mode was used to effectively characterize NPs . Single impacts of Au_{400}^{4+} and C_{60}^{+} perturb a volume of about 1000 nm^3. When the NPs are larger than the volume perturbed by the projectile the method allows examination of the near surfaces of the NPs. The event-by-event bombardment/detection allows to probe surface homogeneity. In our case, the NP and the immediate surroundings. When the dimensions of NPs are or at below the volume perturbed by a single projectile the fundamental chemical process of ionization and emission are notably different when compared to bulk emission. Specific accomplishments can be summarized as follows:

- We have demonstrated that SI emission from NPs of 50 nm or larger are comparable to bulk emission. These observations were made on Al NPs. It remains to be seen how chemical composition may affect SI emission as a function of size. The lowest volumetric limit for bulk emission is yet to be determined.

- A methodology has been developed by determining surface coverage by the concept of effective impacts. The usefulness of NPs often depend on the nature and quality of the surface coverage.

- The ability to quantitatively determine surface coverage of individual NPs in the 50-100 nm size range, to our knowledge, a unique feature of event-by-event bombardment/detection SIMS.

- We report on the first observation on the multi-step fragmentation-recombination process when nanoprojectile impact a single layer of NPs on an organic substrate. The multi-step process requires a head on collision between the projectile and the NP. The nature and the abundance of the ionized ejecta from the process depend on the projectile target interaction.

- We could further distinguish ejecta from grazing projectile NP interaction, from those generated by head on collision. These observations illustrate the feasibility of determining the chemical composition on physically and chemically segregated surfaces, with a spatial resolution of a few nm.

- A mixture of Au and Ag NPs in a single layer has revealed additional surprising fragmentation-elastic-collision-cluster-emission process, when NP projectiles collide head on NPs. This physical process competes with the multi step process that results in adduct emission.

- In a final set of experiments we have demonstrated the ability of soft landed NPs for LDI MS. The novel mode of soft landing NPs using the "gene-gun" holds promise for imaging mass spectrometry. Here NPs enable enhanced SI emission in a solvent free application, i.e. in a manner that retains the integrity of the spatial distribution of molecular species.

Proposed Work

The characterization of NPs using SIMS in the event-by-event bombardment/detection may be extended in several ways:

- To characterize NPs used in other applications, such as nanotoxicology. NPs diffuse, settle, and agglomerate in cell culture media as a function of particle properties: media density, viscosity, particle size, shape, charge and density. These NPs have adverse effects on the body.[154] Here, it is critical to have a chemical understanding of single NPs and their location in cells. Current methodology of analyzing the coating on NPs can be used as a quality control to measure the effectiveness of the functionalization of these NPs. Principles and procedures can be developed for analysis of thin sections of tissues after the dosage of these NPs. The ability to chemically analyze the NP dosed tissue, specifically to identify the chemical interaction of the surfaces with neighboring biomolecules in the cell, would prove useful.

- Investigation of the NPs in the positive mode. The study presented here deals with characterization of NPs in the negative mode. However, several of the NPs such as Ag ionize in the positive mode. Preliminary experiments from our lab have shown that the methodology of SIMS in the event-by-event bombardment/detection can be performed in the positive mode as well. Results have shown that the instrument can be run in positive mode in two ways. The signal from the pulser can be re-routed to act as the start for the secondary ToF. Alternatively, photons emitted from the impacts could be used as the start signal. Preliminary studies from our lab indicate that photons could be

used as start signals for the analysis of various molecules.[155] By using the photon signals as a start for the secondary ToF, NPs could be studied without the use of a substrate.

- The collision-fragmentation-recombination studies can be pursued with different combinations of NPs and substrates. It would be interesting to investigate the effect of substrate make-up on the yield of adducts of fragmentation recombination. Hence, an ideal substrate could be judicially determined that produces the maximum yield for the adducts. Initial experiments have been performed with NaF, other substrates with negative ions of high electron affinity (such as F^{-}, Cl^{-} and I^{-}) could be investigated. The SAM plays an important role in the distribution of the NPs on the surface of the substrate. As there are different surface interactions of the SAM molecule with the molecules of the substrate. The effect of different surfactant/SAM molecules on the SI emission can be investigated by varying the chemical composition and or length of the chain. From a fundamental perspective, an investigation of NPs with diameters below 5nm can be extended to further illustrate the mechanism of secondary recoils. A question that needs to addressed is how does the mass spectrum change when the NPs are in a size that is much below the volume of emission. Other types of NPs in the same size range but of different composition, such as nonmetallic and semiconductor materials could be used. The different NP materials would provide test cases for samples with different electron emission.

- The electron emission from the samples can be used to isolate impacts with localization. Initial studies have been performed on a mass spectrometer that is capable

of combing mass spectrometry with localization. Experiments performed in the instrument has shown that the electron emission from different substrates such as metallic vs. non metallic are different.[156] A sample where NPs are deposited on an organic substrate offers an interesting case of heterogeneity below the 1000 nm^3 for analysis with the this instrument.

REFERENCES

(1) ISI web of science http://portal.isiknowledge.com. **2009**.

(2) Cowburn, R. P.; Welland, M. E. *Science* **2000**, *287*, 1466.

(3) Csaba, G.; Porod, W.; Csurgay, A. I. *Int. J. Circuit Theory Appl.* **2003**, *31*, 67.

(4) Csurgay, A. I.; Porod, W.; Goodnick, S. M. *Int. J. Circuit Theory Appl.* **2001**, *29*, 1.

(5) Bell, A. T. *Science* **2003**, *14*, 1688.

(6) Haensel, V. *U.S. Patent* **1949**, 2479110.

(7) Haensel, V.; Bloch, H. S. *Platinum Met. Rev.* **1964**, *8*, 2.

(8) Kluksdahl, H. E. *U.S. Paten.* **1968**, 3415737.

(9) Van den Berg, J. P.; Lucien, J. P.; Germaine, G.; Thielemans, G. L. B. *Fuel Process. Technol.* **1993**, *35*, 119.

(10) Cooper, B. H.; Donnis, B. H. *Appl. Catal.* **1996**, *137*, 203.

(11) Corma, A.; Martínez, A.; Martínez-Soria, V. *J. Catal.* **2001**, *200*, 259.

(12) Tollefson, J. *Nature* **2007**, *450*, 334.

(13) (a) Faraday, M. *Philos. Trans. R. Soc. London* **1857**, *147*, 145.
(b) Edwards, P. P.; Thomas, J. M. *Angew. Chem. Int. Ed.* **2007**, *46*, 5480.

(14) De, M.; Ghosh, P. S.; Rotello, V. M. *Adv. Mater.* **2008**, *20*, 4225.

(15) Nativo, P.; Prior, I. A.; Brust, M. *ACS Nano* **2008**, *2*, 1639.

(16) Li, J. L.; Wang, L.; Liu, X-Y.; Zhang, Z-P.; Guo, H-C.; Liu, W-M.; Tang, S-H. *Cancer Lett.* **2009**, *274*, 319.

(17) Yamada, T.; Iwasaki, Y.; Tada, H.; Iwabuki, H.; Chuah, M. K.; VandenDriessche, T.; Fukuda, H.; Kondo, A.; Ueda, M.; Seno, M.; Tanizawa, K.; Kuroda, S. *Nat Biotechnol*. **2003**, *21*, 885.

(18) Derfus, A. M.; Maltzahn, G.; Harris, T. J.; Duza, T.; Vecchio, K. S.; Ruoslaht, E.; Bhatia, S. N. *Adv. Mater.* **2007**, *19*, 3932.

(19) Ferrari, M. *Nat. Rev. Cancer* **2005**, *3*, 161.

(20) Mirkin, C. A.; Letsinger, R. L.; Mucic, R. C.; Storhoff, J. J. *Nature* **1996**, *382*, 607.

(21) Xu, X. Y.; Han, M. S.; Mirkin, C. A. *Angew. Chem. Int. Ed.* **2007**, *46*, 3468.

(22) Batista, P.; Pereira, E.; Eaton, P.; Doria, G.; Miranda, A.; Gomes, I.; Quaresma, P.; Franco, R. *Anal. Bioanal. Chem.* **2008**, *391*, 943.

(23) Liu, J. W.; Lu, Y. *Org. Biomol. Chem.* **2006**, *4*, 3435.

(24) Hirsch, L. R.; Jackson, J. B.; Lee, A; Halas, N. J.; West, J. *Anal. Chem.* **2003**, *75*, 2377.

(25) Bruchez, M.; Moronne, M.; Gin, P.; Weiss, S.; Alivisatos, A. P. *Science* **1998**, *281*, 2013.

(26) Zhou, M.; Ghosh, I. *Biopolymers* **2007**, *88*, 325.

(27) Rosi, N. L.; Mirkin, C. A. *Chem. Rev*. **2005**, *105*, 1547.

(28) Jin, Y. H.; Kannan, S.; Wu, M.; Zhao, J. X. J. *Chem. Res. Toxicol.* **2007**, *20*, 1126.

(29) He, H.; Xie, C.; Ren, J. *Anal. Chem.* **2008**, *80*, 5951.

(30) Boisselier, E.; Astruc, D. *Chem.Soc.Rev*. **2009**, *38*, 1759.

(31) Ostrowski, A, D.; Martin, T.; Conti, J.; Hurt, I.; Harthorn, B. H. *J. Nanopart Res*. **2009**, *11*, 251.

(32) Borm, P. J. A.; Robbins, D.; Haubold. S.; Kuhlbusch, T.; Fissan, H.; Donaldson, K.; Schins, R. P. F.; Stone, V.; Kreyling, W.; Lademann, J.; Krutmann, J.; Warheit, D.; Oberdorster, E. *Part. Fibre Toxicol*. **2006**, *3*, 11.

(33) Oberdörster, G.; Oberdörster, E.; Oberdörster, J. *Environ. Health. Perspect*. **2005**, *113*, 823.

(34) Hoet, P. H. M.; Bruske-Hohlfeld, I.; Salata, O. V. *Nanobiotechnol.* **2004**, *2*, 12.

(35) Nel, A.; Xia, T.; Madler, L.; Li, N. *Science* **2006**, *311*, 622.

(36) Kunzli, N.; Tager, I. B. *Swiss Med. Wkly.* **2005**, *135*, 697.

(37) Kaiser, J. *Science* **2005**, *307*, 1858.

(38) Kulmala, M.; Vehkamaki, H.; Petaja, T.; Dal Maso, M.; Lauri, A.; Kerminen, V.-M.; Birmili, W.; McMurry, P. H. *J. Aerosol Sci.* **2004**, *35*, 143.

(39) Oberdorster, G.; Oberdorster, E.; Oberdorster, J. *Environ. Health Perspect*. **2005**, *113*, 823.

(40) Englert, N. *Toxicol. Lett*. **2004,** *149*, 235.

(41) Moghimi, S. M.; Hunter, A. C.; Murray, J. C. *FASEB J.* **2005**, *19*, 311.

(42) Sonavane, G.; Tomoda, K.; Sano, A.; Ohshima, H.; Terada, H.; Makino, K. *Colloids Surf. B*. **2008**, *65*, 1.

(43) Churg, A. *Free Radical Biol. & Med.* **2003**, *34*, 1230.

(44) Ferin, J. *Toxicol. Lett*. **2004**, *72*, 121.

(45) Gustavsson, P.; Gustavsonn, A.; Hogstedt, C. *Br. J. Ind. Med.* **1988**, *45*, 777.

(46) Ferin, J.; Oberdorster, G. *Acta Astronaut.* **1992**, *27*, 257.

(47) Tanaka, K.; Waki, H.; Ido, Y.; Akita, S.; Yoshida, Y.; Yoshida, T. *Rapid Commun. Mass Spectrom.* **1988**, *2*, 151.

(48) Sunner, J.; Dratz, E.; Yu-Chie, C. *Anal. Chem.* **1995**, *67*, 4335.

(49) Dale, M.; Knochemuss, R.; Zenobi, R. *Anal. Chem.* **1996**, *68*, 3321.

(50) Schurenberg, M.; Dreisewerd, K.; Hillenkamp, F. *Anal. Chem.* **1999**, *71*, 221.

(51) McLean, J. A.; Stumpo, K. A.; Russell, D. H. *J. Am. Chem. Soc.* **2005**, *127*, 5304.

(52) Sherrod, S. D.; Diaz, A. J.; Russell, W. K.; Cremer, P. S.; Russell, D. H. *Anal. Chem.* **2008**, *80*, 6796.

(53) Taira, S.; Sugiura, Y.; Moritake, S.; Shimma, S.; Ichiyanagi, Y.; Setou, M. *Anal. Chem.* **2008**, *80*, 4761.

(54) Zhu, Z. L.; Ghosh, P. S.; Miranda, O. R.; Vachet, R. W.; Rotello, V. M. *J. Am. Chem. Soc.* **2008**, *130*, 14139.

(55) Skala, M. C.; Crow, M. J.; Wax, A.; Izatt, J. A. *Nano Lett*. **2008**, *8*, 3461.

(56) Lal, S. L.; Clare, S. E.; Halas, N. J. *Acc. Chem. Res.* **2008**, *41*, 1842.

(57) Sperling, R. A.; Rivera Gi, P. I.; Zhang, F.; Zanella, M.; Parak, W. J. *Chem. Soc. Rev*. **2008**, *37*, 1896.

(58) Stöckle R. M.; Suh Y. D.; Deckert. V.; Zenobi R. *Chem. Phys. Lett*. **2000**, *318*, 131.

(59) Whetten, R. L.; Khoury, J. T.; Alvarez, M. M.; Murthy, S.; Vezmar, I.; Wang, Z. L.; Stephens, P. W.; Cleveland, C. L.; Luedtke, W. D.; Landman, U. *Adv. Mater.* **1996**, *8*, 428.

(60) Jimenez, V. L.; Georganopoulou, D. G.; White, R. J.; Harper, A. S.; Mills, A. J.; Lee, D; Murray, R. W. *Langmuir*. **2004**, *20*, 6864.

(61) McNeal, C. J.; Hughes, J. M.; Pignolet, L. H.; Nelson, L. T. J.; Gardner, T. G.; Fackler Jr, J. P.; Winpenny, R. E. P.; Irgens, L. H.; Vigh, G.; Macfarlane, R. D. *Inorg. Chem.* **1993**, *32*, 5582.

(62) Negishi, Y.; Chaki, N. K.; Shichibu, Y.; Whetten, R. L.; Tsukuda, T. *J. Am. Chem. Soc.* **2007**, *129*, 11322.

(63) Chaki, N. K.; Negishi, Y.; Tsunoyama, H.; Shichibu, Y.; Tsukuda, T. *J. Am. Chem. Soc.* **2008**, *130*, 8608.

(64) Bertino, M. F.; Sun, Z.-M.; Zhang, R.; Wang, L.-S. *J. Phys. Chem. B.* **2006**, *110*, 21416.

(65) Tracy, J. B.; Kalyuzhny, G.; Crowe, M. C.; Balasubramanian, R.; Choi, J-P.; Murray, R. W. *J. Am. Chem. Soc.* **2007**, *129*, 6706.

(66) Tracy, J. B.; Crowe, M. C.; Parker, J. F.; Hampe, O.; Fields-Zinna, C. A.; Dass, A.; Murray, R. W. *J. Am. Chem. Soc.* **2007**, *129*, 16209.

(67) Dass, A.; Stevenson, A.; Dubay, G. R.; Tracy, J. B.; Murray, R. W. *J. Am. Chem. Soc.* **2008**, *130*, 5940.

(68) Schaaff, T. G.; Whetten, R. L. *J. Phys. Chem. B.* **2000**, *104*, 2630.

(69) Gaumet, J. J.; Strouse, G. F. *J. Am. Soc. Mass Spectrom.* **2000**, *11*, 338.

(70) Gaumet, J. J.; Khitrov, G. A.; Strouse, G. F. *Nano Lett*. **2002**, *2*, 375.

(71) Dass, A.; Holt, K.; Parker, J. F.; Feldberg, S. W.; Murray, R. W. *J. Phys. Chem. C*. **2008**, *112*, 20276.

(72) Cliffel, D. E.; Zamborini, F. P.; Gross, S. M.; Murray, R. W. *Langmuir*. **2000**, *16*, 9699.

(73) Dass, A.; Dubay, G. R.; Fields-Zinna, C. A.; Murray, R. W. *Anal. Chem*. **2008**, *80*, 6845.

(74) Lover, T.; Henderson, W.; Bowmaker, G. A.; Seakins, J. M.; Cooney, R. P. *Inorg. Chem*. **1997**, *36*, 3711.

(75) Lover, T.; Henderson, W.; Bowmaker, G. A.; Seakins, J. M.; Cooney, R. P. *Chem. Mater*. **1997**, *9*, 1878.

(76) Wang, S.; Zordan, C. A.; Johnston, M. V. *Anal. Chem.* **2006**, *78*, 1750.

(77) Zordan, C. A.; Wang, S.; Johnston, M. V. *Environ. Sci.Technol.* **2008**, *42*, 6631.

(78) Zelenyuk, A.; Imre, D.; Han, J. H.; Oatis, S. *Anal. Chem*. **2008**, *80*, 1401.

(79) Castner, D. G. *Nature* **2003**, *422*, 129.

(80) Pellin, M. J. *Pure & Appl. Chem*. **1992**, *4*, 591.

(81) Blain, M. G.; Della-Negra, S.; Joret, H.; Le Beyec, Y.; Schweikert, E. A. *Phys. Rev. Lett*. **1989**, *63*, 1625.

(82) Boussofiane-Baudin, K.; Bolbach, G.; Brunelle, A.; Della-Negra, S.; Hakansson, P.; Le Beyec, Y. *Nucl. Instrum. Methods Phys. Res. B*. **1994**, *88*, 160.

(83) Appelhans, A. D.; Delmore, J. E. *Anal. Chem*. **1989**, *61*, 1087.

(84) Tempez, A.; Schultz, J. A.; Della-Negra, S.; Depauw, J.; Jacquet, D.; Novikov, A.; Lebeyec, Y.; Pautrat, M.; Caroff, M.; Ugarov, M.; Bensaoula, H.; Gonin, M.; Fuhrer, K.; Woods, A. *Rapid Comm. Mass Spec.* **2004**, *18*, 371.

(85) Thbmpson, D. A. *Radiat. €ff.* **1981,** *56,* 105.

(86) Van Stipdonk, M. J.; Harris, R. D.; Schweikert, E. A. *Rapid Comm. Mass. Spec.* **1996**, *10*, 1987.

(87) Wong, S. C. C.; Hill, R.; Blenkinsopp, P.; Lockyer, N. P; Weibel, D.E; Vickerman, J.C. *Appl. Surf. Sci.* **2003**, *203*, 219.

(88) Rickman, R. D. *Ph.D. Dissertation, Texas A&M University, College Station, TX*. **2004.**

(89) Andersen, H. H.; Bay, H. L.; *J.Appl.Phys.* **1974**, *45*, 953.

(90) Bitensky, I.S.; Parilis, E. S. *Nucl. Instrum. Methods Phys. Res. B.* **1987**, *21*, 26.

(91) Guillermier, C.; Della-Negra, S.; Schweikert, E. A.; Dunlop, A.; Rizza, G. *Int. J. Mass Spec.* **2008**, *275*, 86.

(92) Chen, B-J.; Yin, Y-S.; Ling, Y-C. *Appl.Surf.Sci.* **2008**. *255*, 977.

(93) Min, H.; Kim, Y.; Yu, H.; Moon, D.W.; Lim, S.J.; Yoon, H-Y.; Lee, T.G.; Shin, S.K. *Chem. Eur.J.* **2008**, *14*, 8461.

(94) Sun, Y.; Frenkel, A. I.; White, H.; Zhang, L.; Zhu, Y.; Xu, H.; Yang, J. C.; Koga, T.; Zaitsev, V.; Rafailovich, M. H.; Sokolov, J. C., *J. Phys. Chem.B.* **2006**, *110*, 23022.

(95) Novikov, A.V.; Kirillov, S. N.; Baranov, I. A; Obnorskii, V.V.; Yarmiychuk, S. V. *Appl. Surf. Sci.* **2006**, *252*, 7034.

(96) Baranov, I.; Della-Negra, S.; Fallavier, M.; Kirillov, S.; Beyec, Y. L.; Novikov, A.; Obnorskii, V.; Wien, K.; Yarmiychuk, S. *Nucl. Instrum. Methods Phys. Res. B.* **2006,** *245*, 184.

(97) Shi, D.; He, P.; Wang, S. X.; Ooij, W. J.; Wang, L. M.; Zhao, J.; Zhou, Y. *J. Mater. Res.* **2002**, *17*, 982.

(98) Pinnick, V.; Verkhoturov, S. V.; Kaledin, L.; Bisrat, Y.; Schweikert, E.A. *Anal. Chem.* **2009**, *81*, 7527.

(99) Li, Z.; Verkhoturov, S. V.; Schweikert, E. A. *Anal. Chem*. **2006**, *78*, 7410.

(100) Li, Z.; Verkhoturov, S. V.; Locklear, J. E.; Schweikert, E. A. *Int. J. Mass Spec.* **2008**, *269*, 112.

(101) Knoll, G. F. *Radiation Detection and Measurement*, 2nd ed.; Wiley: New York, **1989**.

(102) Park, M. A.; Gibson, K. A.; Quinones, K.; Schweikert, E. A. *Science* **1990**, *248*, 988.

(103) Della Negra, S.; Jacquet, D.; Lorthiois, Y.; Le Beyec, Y. *Int. J. Mass Spec. Ion Phys.* **1983**, *53*, 215.

(104) Van Stipdonk, M. J.; Schweikert, E. A.; Park, M. A. *Journal of Mass Spectrometry* **1997**, *32*, 1151.

(105) Verkhoturov, S. V.; Schweikert, E. A.; Rizkalla, N. M. *Langmuir.* **2002**, *18*, 8836.

(106) Diehnelt, C. W.; English, R. D.; Van Stipdonk, M. J.; Schweikert, E. A. *Nucl. Instrum. Methods Phys. Res. B.* **2002**, *193*, 883.

(107) Locklear, J. E.; Verkhoturov, S. V.; Schweikert, E. A. *Int. J. Mass Spec.* **2004,** *238*, 59.

(108) Rickman, R. D.; Verkhoturov, S. V.; Parilis, E. S.; Schweikert, E. A. *Phys. Rev. Lett.* **2004**, *92*, 047601.

(109) Fried, L. E.; Manaa, M. R.; Pagoria, P. F.; Simpson, R. L. A*nn. Rev. Mater. Res.* **2001**, *31*, 291.

(110) Kaledin, L.; Tepper, F. *Dekker Encyclopedia of Nanoscience and Nanotechnology.* Taylor and Francis Group Publishing: London, **2004**, 1936-1945.

(111) http://www.argonide.com. **2007**.

(112) Cliff, M. D.; Tepper, F.; Lisetsky, V. *Ageing Characteristics of Alex ® nanosize Aluminum.* AIAA. **2001**, 3287.

(113) Toshima, N. *Dekker Encyclopedia of Nanoscience and Nanotechnology*. Taylor and Francis Group Publishing: London, **2004**, 1869-1880.

(114) Verkhoturov, S. V.; Rickman, R. D.; Guillermier, C.; Hager, G. J.; Locklear, J. E.; Schweikert, E. A. *Appl. Surf. Sci.* **2006**, *252*, 6490.

(115) Delcorte, A.; Garrison, B. J**.** *J. Phys. Chem. C*. **2007**, *111*, 15312.

(116) Verkhoturov, S. V.; Rickman, R. D.; Balderas, S.; Schweikert, E. A. *Appl. Surf. Sci.* **2004**, *113*, 231.

(117) Rickman, R. D.; Verkhoturov, S. V.; Hager, G. J.; Schweikert, E. A. *Int. J. Mass Spec. Ion Phys.* **2005**, *245*, 48.

(118) Bouneau, S. ; Della-Negra, S. ; Depauw, J. ; Jacquet, D.; Le Beyec, Y. ; Mouffron, J. P. ; Novikov, A. ; Pautrat, M. *Nucl. Instrum. Methods Phys. Res. B*. **2004**, *225*, 579.

(119) Rickman, R. D.; Verkhoturov, S. V.; Hager, G. J.; Schweikert, E. A.; Bennet, J. A. *Int. J. Mass Spec. Ion Phys.* **2005**, *241*, 57.

(120) Locklear, J. E. *Ph.D. Dissertation, Texas A&M University, College Station, TX*. **2006**.

(121) Verdier, S.; Metson, J. B.; Dunlop, H. M. *J. Mass Spectrometry* **2007**, *42*, 11.

(122) Verkhoturov, S. V.; Rickman, R. D.; Guillermier, C.; Hager, G. J.; Locklear, J. E.; Schweikert, E. A. *Appl. Surf. Sci.* **2006,** *252*, 6490.

(123) Witmaack, K. Quantitative analysis of solids by SIMS and SNMS. In *Quantitative Microbeam Analysis*; Fitzgerald, A. G.; Storey, B. E.; Fabian, D., Eds.; IOP Publishing Ltd: London, **1993**; Chapter 1. 352-358.

(124) Schaaff, T. G.; Whetten, R. L. *J. Phys. Chem. B*. **2000**, *104*, 2630.

(125) Garcia, M. A.; Merino, J. M.; Fernández Pinel, E.; Quesada, A.; De la Venta, J.; Ruiz González, M. L.; Castro, G. R.; Crespo, P.; Llopis, J.; González-Calbet, J. M.; Hernando, A. *Nano Lett.* **2007**, *7*, 1489.

(126) Xiao, Y.; Patolsky, F.; Katz, E.; Hainfeld, J. F.; Willner, I. *Science* **2003**, *299*, 1877.

(127) Garitaonandia, J. S.; Insausti, M.; Goikolea, E.; Suzuki, M.; Cashion, J. D.; Kawamura, N.; Ohsawa, H.; GildeMuro, I.; Suzuki, K.; Plazaola, F.; Rojo, T. *Nano Lett*. **2008**, *8*, 661.

(128) Kruse, J.; Dolgner, K.; Greve, H.; Zaporojtchenko, V.; Faupel, F. *J. Phys. D: Appl. Phys.* **2006**, *39*, 5086.

(129) Greve, H.; Biswas, A.; Schürmann, U.; Zaporojtchenko, V.; Faupel, F. *App. Phys. Lett*. **2006**, *88*, 123103.

(130) Rajagopalachary, S.; Verkhoturov, S.V.; Schweikert, E.A. *Nano Lett*. **2008**, *8*, 1076.

(131) Winograd, N. *Anal. Chem*. **2005**, *77*, 142A.

(132) Nagy, G.; Walker, A.V. *Int. J. Mass Spec.* **2007**, *262*, 144.

(133) Smetana, A. B.; Klabunde, K. J.; Sorensen, C. M. *J. of Colloid Interface Sci.* **2005**, *284*, 521.

(134) Guillermier, C.; Della Negra, S.; Rickman, R. D.; Hager, G. J.; Schweikert, E. A. *Int. J. Mass Spec.* **2007**, *263*, 298.

(135) Pinnick, V.; Rajagopalachary, S.; Verkhoturov, S. V.; Kaledin, L.; Schweikert, E.A. *Anal. Chem*. **2008**, *80*, 9052.

(136) Kissel, R.; Urbassek, H. M. *Nucl. Instrum. Methods Phys. Res. B*. **2001**, *180*, 293.

(137) Mellado, E. M.; Hornung, K.; Kissel, J. *Int. J. Impact Engineering* **2006**, *33*, 419.

(138) Brunelle, A.; Della-Negra, S.; Depauw, J.; Jacquet, D.; Le Beyec, Y.; Pautrat, M.; Baudin, K.; Andersen, H. H. *Phys. Rev. Lett.* **2001**, *63*, 022902.

(139) Harris, R. D. *Ph.D. Dissertation, Texas A&M University, College Station, TX.* **1998**.

(140) Della-Negra, S.; Depauw, J.; Pautrat, M.; Dunlop, A.; Rizza, G.; Guillermier, C.; Schweikert, E. A. Abstracts of the Desorption 2008, Innovations in Mass Spectrometry of Biomolecules, Ontario, Canada.

(141) Guillermier, C.; Pinnick, V.; Verkhoturov, S. V.; Schweikert, E.A. *Appl. Surf. Sci.* **2006**, *252*, 6644.

(142) Rajagopalachary, S.; Verkhoturov, S.V.; Schweikert, E.A. *Anal. Chem.* **2009**, *81*, 1089.

(143) Novikov, A.; Caroff, M.; Della-Negra, S.; Le Beyec, Y.; Pautrat, M.; Schultz, J. A.; Tempez, A.; Wang, H. Y. J.; Jackson, S. N.; Woods, A. S. *Anal. Chem.* **2004**, *76*, 7288.

(144) Tempez, A.; Ugarov, M.; Egan, T.; Schultz, J. A.; Novikov, A.; Della-Negra, S.; Lebeyec, Y.; Pautrat, M.; Caroff, M.; Smentkowski, V. S.; Wang, H. Y. J.; Jackson, S. N.; Woods, A. S. *J. Proteome Res.* **2004**, *4*, 540.

(145) Klein, T. M.; Wolf, E. D.; Wu, R.; Sanford, J. C. *Nature* **1987**, *327*, 70.

(146) Kikkert, J.; Humiston, G.; Roy, M.; Sanford, J. *In Vitro Cellular & Developmental Biology – Plant* **1999**, *35*, 43.

(147) Yi, L. *IEEE Transactions on Biomedical Engineering* **2007**, *54*, 1507.

(148) Haberland, H.; Insepov, Z.; Kurrais, M.; Mall, M.; Moseler, M.; Thurner, Y. *Nucl. Instrum. Methods Phys. Res. B*. **1993**, *80-81*, 1320.

(149) Kikkert, J. *Plant Cell, Tissue and Organ Culture*. **1993**, *33*, 221.

(150) Jain, P. K.; Lee, K. S.; El-Sayed, I. H.; El-Sayed, M. A. *J. Phys. Chem. B.* **2006**, *110*, 7238.

(151) Chen, H. L.; Cheng, H. C.; Ko, T. S.; Chuang, S. Y.; Chu, T. C. *Japenese Journal Appl Phys*. **2006**, *45*, 6984.

(152) Teng, C.-H.; Ho, K.-C.; Lin, Y.-S.; Chen, Y.-C. *Anal. Chem*. **2004**, *76*, 4337.

(153) Prodan, E.; Radloff, C.; Halas, N. J.; Nordlander, P. *Science* **2003**, *302*, 419.

(154) Teeguarden, J, G.; Hinderliter, P. M.; Orr, G.; Thrall, B. D.; Pounds, J. G. *Toxicology Sci*. **2007**, *95*, 300.

(155) Fernandez-Lima, F. A.; Pinnick, V.; Verkhoturov, S. V.; Schweikert, E.A. *Surface Interface Analysis. Submitted.*

(156) Verkhoturov, S.V.; Eller, M.; Rickman, R. D.; Della-Negra, S.; Schweikert, E. A. *J. Phys. Chem. C. In Press.*

VITA

Name:	Sidhartha Raja Rajagopal Achary
Address:	Center for Chemical Characterization and Analysis (CCCA) Teague Building—Room G21 Texas A&M University College Station, Texas 77843-3144
Email Address:	sidhat@gmail.com
Education:	B.S., Chemistry, Wichita State University, 2002 Ph.D., Chemistry, Texas A&M University, 2010